Terahertz-induced ultrafast symmetry control in condensed matter

Haoyu Huang

Fachbereich Physik
Universität Hamburg

zur Erlangung des akademischen Grades
Doctor rerum naturalium

Fakultät für Mathematik, Informatik
und Naturwissenschaften

August 2020

Gutachter der Dissertation:	Prof. Dr. Franz X. Kärtner Prof. Dr. Christian Bressler
Datum der Disputation:	05.08.2020

Declaration

I hereby declare that except where specific reference is made to the work of others, the contents of this dissertation are original and have not been submitted in whole or in part for consideration for any other degree or qualification in this, or any other university. This dissertation is my own work and contains nothing which is the outcome of work done in collaboration with others, except as specified in the text and Acknowledgements.

Haoyu Huang
August 2020

Acknowledgements

First and foremost, I would like to thank my Ph.D. advisor, Prof. Dr. Franz X. Kärtner, who offered me the great opportunity to stay in his group for my doctoral study. As a supervisor, he gave me the flexibility to freely explore the topics I like in his group and inspire me a lot in the field of ultrafast optics through his guidance and feedback in our weekly group seminar. I am very grateful for his generosity to fund me to report my results in international conferences in US and Japan, which not only teaches me how to present my works to a large professional audience but also help me to build up connections in the optical society and broaden my horizon of the world.

I would like to also thank Dr. Oliver D. Mücke, who is my team leader and second supervisor, and supports me daily through his detailed suggestions and feedback in my experiments. I also benefited a lot from his kind help to improve my academic writing and presentation skills.

I would like to thank Prof. Dr. Guoqing Chang, my previous second supervisor, who gave me a lot of enlightenment in my research and life through sharing his methodology and life experience. In addition to that, I did cherish the experience to spend four pleasant days in his new house with his family in the US two years ago, which has significantly enriched my personal life.

I would like to especially thank Dr. Liwei Song, with whom I worked together intimately over most of my Ph.D. period. I learned a lot from him. His initiation towards the study of THz induced birefringence in water led me to join this project and his previous experience in OPA design and ultrafast THz sources make the implementation of the project of "ultrafast symmetry control of solids by an intense terahertz field" possible. Besides, his humor and kindness in his personality make our lab a pleasant workplace. I do treasure our friendship built in our work and daily life.

I also would like to express my gratitude to many colleagues with whom I spend much research life in CFEL. Firstly, I would like to thank Dr. Yudong Yang and Nicolai Klemke, I benefited a lot from their suggestions and help in the lab. Meanwhile, I enjoy the moment we sit down and talk together during our daily coffee break time.

Furthermore, I would like to thank our group secretary Christine Berber who helped me a lot with administrative tasks in DESY with a kind heart.

And I give special thanks to my Chinese colleagues in Franz's group, Qiao Cao, Yizhou Liu, Yi Hua. We spent a lot of joyful moments together at DESY and support each other in our daily life.

Last and foremost, I would like to thank my parents and my girlfriend, their support is my strength to overcome all the difficulties in my Ph.D. research period.

Abstract

The study of broken symmetry has a profound meaning in every aspect of science. The presence of an external field can break the symmetry in condensed matter, i.e., the spherical symmetry in the liquids and the inversion symmetry in centrosymmetric crystals. In this thesis, by employing an intense terahertz (THz) pulse as the external field, we conduct two separate studies: the THz induced birefringence in liquids and the ultrafast control of even-order harmonic generation from solids.

In chapter 1, we introduce the general motivation and introduction of the study of symmetry control in the condense matter by an intense THz pulse.

In chapter 2, we explain the principle of optical parametric amplification and discuss the design and properties of our home-build OPA.

In chapter 3, we discuss the principles of generating ultrafast THz pulses with strong electric fields via optical rectification (OR) and the characterization of THz pulse via electro-optic sampling (EO-sampling). In particular, we highlight the tilted-pulse-fronts (TPF) technique[1] as well as OR in organic crystal DSTMS, as these two techniques are exploited in chapter 4 and chapter 5.

In chapter 4, we study the THz-field induced birefringence in molecular liquids utilizing the Kerr effect. We find experimental evidence for a THz-induced optical birefringence, which provides evidence for molecular orientation. Moreover, by studying liquid water, using a combination of THz pump and optical probe experiments, we demonstrate a transient orientation of their dipole moments, not possible by optical excitation. The resulting birefringence reveals that the polarizability of water is lower along its dipole moment than the average value perpendicular to it. This anisotropy, also observed in heavy water and alcohols, increases with the concentration of sodium iodide. Our results enable a more accurate parametrization and a benchmarking of existing and future water models.

In chapter 5, we will give a brief overview of high-harmonic generation in solids, followed by a very general symmetry theory of solids which implies the symmetry control of harmonic generation in solids, then comes to our experimental proofs of achieving ultrafast control of even-order harmonic generation from solids by an intense terahertz field. Uniquely, we demonstrate that the crystal symmetry is not only broken but also controlled by an intense

THz beam. The transient generation of even-order harmonics along the THz electric field is measured. For crystals without even-order polarization, such as Si and diamond, the intensity of the generated harmonics is affected by the THz polarization which determines the even-order nonlinear polarity. While for crystals with initial even order polarization, such as GaAs, the even-order harmonic generation could be either enhanced or inhibited regarding the direction of the THz electric field. This study paves a way to ultrafast all-optical crystal symmetry control, which can be used in the high harmonic generation, optical frequency conversion, THz electric field measurements, and so on.

In chapter 6, I will introduce the results of setting up a compact XUV beamline and some first results of XUV signals from MgO and NiO. The XUV emission from MgO shows HHG features, while the XUV emission from NiO does not behave as expected. So more experiments and theoretical calculations are needed to understand this XUV emission mechanism.

Zusammenfassung

Die Untersuchung gebrochener Symmetrien hat eine tiefgreifende Bedeutung in vielen Feldern der Naturwissenschaften. Die Symmetrien von kondensierter Materie - beispielsweise die sphärische Symmetrie von Flüssigkeiten und die Inversionssymmetrie von zentrosymmetrischen Kristallen - können gebrochen werden durch die Präsenz eines externen Feldes. In dieser Doktorarbeit werden starke THz-Impulse als solche externe Felder benutzt und damit zwei verschiedene Phänomene untersucht: Die THz-induzierte Doppelbrechung in Flüssigkeiten sowie die ultraschnelle Kontrolle von Hohen Harmonischen gerader Ordnung die in Festkörpern erzeugt werden.

Kapitel 1 beinhaltet die grundsätzliche Motivation sowie die Einleitung für die Untersuchung der Symmetriekontrolle in kondensierter Materie durch einen starken THz-Impuls.

In Kapitel 2 werden die Prinzipien von optischer parametrischer Verstärkung erklärt und das Design und die Eigenschaften des eigens für diese Arbeit angefertigten, optischen parametrischen Verstärkers diskutiert.

Kapitel 3 befasst sich mit der Erzeugung von ultraschnellen THz-Impulsen mithilfe der optischen Gleichrichtung. Dabei wird das Hauptaugenmerk auf die Technik der verdrehten Wellenfront sowie auf die THz-Erzeugung im organischen Kristall DSTMS gelegt, da diese beiden Methoden in den Kapiteln 4 und 5 angewendet werden. Auch wird die Charakterisierung der THz-Impulse mittels elektrooptischen Samplings thematisiert.

In Kapitel 4 wird die THz-induzierte Doppelbrechung in molekularen Flüssigkeiten mithilfe des Kerr-Effekts untersucht. Experimentell wird hierbei ein solcher induzierter Doppelbrechungseffekt gefunden, welcher die Schlussfolgerung zulässt, dass sich die Moleküle im THz-Feld orientieren. Weiterhin wird in Pump-Probe Experimenten mit Wassermolekülen eine ultraschnelle Ausrichtung der Dipolmomente gemessen die nicht passiert mit optischer Anregung. Die induzierte Doppelbrechung zeigt, dass die Polarisierbarkeit von Wasser niedriger entlang der Achse des Dipolmoments ist, als entlang der dazu orthogonalen Achse. Die Anisotropie – die auch in schwerem Wasser und Alkoholen beobachtet wird – wächst mit der Konzentration von Natriumiodid. Diese Ergebnisse erlauben eine präzisere Parametrisierung sowie eine Referenzierung von existierenden und zukünftigen Modellen zur Beschreibung von Wasser.

Kapitel 5 enthält einen kurzen Überblick über die Hohe Harmonische Erzeugung in Festkörpern, gefolgt von einer grundsätzlichen Theorie welche beschreibt wie die Hohen Harmonischen mittels der Symmetrie kontrolliert werden können. Anschließend wird dies experimentell mit THz-gestützter Erzeugung von geraden Ordnungen Hoher Harmonischer, welche auf ultraschnellen Zeitskalen kontrolliert werden können, nachgewiesen. Es wird gezeigt, dass das THz-Feld die Symmetrie nicht nur brechen sondern auch kontrolliert manipulieren kann. Bei Kristallen mit Inversionssymmetrie wie Si und Diamant beeinflusst die Polarisation des THz-Feldes die Intensität der geraden harmonischen Ordnungen. Bei Kristallen ohne Inversionssymmetrie, beispielsweise GaAs, werden die geraden harmonischen Ordnungen je nach Orientierung des THz-Feldes verstärkt oder abgeschwächt. Diese Untersuchungen weisen den Weg zu ultraschneller rein optischen Symmetriekontrolle in Kristallen mit einer Vielzahl an Anwendungsmöglichkeiten, beispielsweise in den Bereichen der Hohen Harmonischen Erzeugung, der optischer Frequenzkonversion und der THz-Feld Messungen.

In Kapitel 6 werden erste Ergebnisse präsentiert, in denen mithilfe einer kompakten Vakuumbeamline extrem ultraviolette (EUV) Strahlung von NiO und MgO erzeugt wurden. Die EUV-Emissionen von MgO werden eindeutig als Hohe Harmonische Erzeugung identifiziert während die EUV-Emissionen von NiO anderen Ursprungs ist. Um diesen Ursprung näher zu verstehen wären weitere Experimente sowie Simulationen notwendig.

Table of contents

Nomenclature

Acronyms / Abbreviations

CEP Carrier-envelope phase

CPA Chirped pulse amplification

DFG Difference frequency generation

FROG Frequency resolved optical gating

HHG High harmonic generation

OPA Optical parametric amplifier

DSTMS 4-N,N-dimethylamino-4'-N'-thyl-stilbazolium 2,4,6-trimethylbenzenesulfonate

OR optical rectification

TDDFT time-dependent density-functional theory

SFG Sum frequency generation

SHG Second harmonic generation

XUV extreme ultraviolet

Chapter 1

Introduction

1.1 Overview

1.1.1 the motivation for the study of symmetry control in condense matter by an intense THz pulse

The primordial concept of symmetry comes into the cognitive history of mankind through the recognition of the beauty of geometrical forms [2]. When talking about the role of symmetry in physics, the Nobel laureate PW Anderson states in his article *More is Different* [3], "it is only slightly overstating the case to say that physics is the study of symmetry." Meanwhile, he also revealed that the broken symmetry could lead to the complexity which contains plenty of levels of the organization and each level can require a whole new conceptual structure [3]. The DNA structure, the "information-bearing crystallinity" which contains the vital genetic information to life, is a good example of this kind of complexity [3]. Therefore, the study of broken symmetry has a profound meanings in every aspect of science. In this thesis, we would focus on the study of symmetry control in the condense matter by an intense THz pulse.

In our daily life, The most familiar examples of condensed phases are solids and liquids, which arise from the electromagnetic forces between atoms.The presence of the external field would break the symmetry in condensed matter, i.e., the spherical symmetry in the liquid and the inversion symmetry in centrosymmetric crystals. This concept lies in the center of this thesis and would be implemented by employing an intense terahertz (THz) pulse as the external field to conducting two separate studies:

- THz induced birefringence in liquids,
- ultrafast control of even-order harmonic generation from solids.

1.1.2 Outline of thesis

In chapter 1, we introduce the general motivation and introduction of the study of symmetry control in condensed matter by an intense THz pulse.

In chapter 2, we explain the principle of optical parametric amplification and exhibit the design and properties of our home-build OPA.

In chapter 3, we discuss the principles of generating ultrafast THz pulses with strong electric fields via optical rectification (OR) process and the characterization of THz pulse via electro-optic sampling (EO-sampling) technique. In particular, we highlight the tilted-pulse-fronts (TPF) technique[1] as well as OR in organic crystal DSTMS, as these two techniques are exploited in chapter 4 and chapter 5.

In chapter 4, we study the THz-field induced birefringence in molecular liquids by utilizing the Kerr effect. We find experimental evidence for a THz-induced optical birefringence, which provides evidence for molecular orientation. Moreover, by studying liquid water, using a combination of THz pump and optical probe experiments, we demonstrate a transient orientation of their dipole moments, not possible by optical excitation. The resulting birefringence reveals that the polarizability of water is lower along its dipole moment than the average value perpendicular to it. This anisotropy, also observed in heavy water and alcohol, increases with the concentration of sodium iodide. Our results enable a more accurate parametrization and a benchmarking of existing and future water models.

In chapter 5, we will give a brief overview of high-harmonic generation in solids, followed by a very general symmetry theory of solids which implies the symmetry control of harmonic generation in Solids, then comes to our experimental proofs of achieving ultrafast control of even-order harmonic generation from solids by an intense terahertz field. Uniquely, we demonstrate that the crystal symmetry is not only broken but also manipulated by an intense THz beam. The transient generation of even-order harmonics along the THz electric field is measured. For crystals without even order polarization, such as Si and diamond, the intensity of the generated harmonics is affected by the THz polarization which determined the even-order nonlinear polarity. While for crystals with initial even order polarization, such as GaAs, the even-order harmonic generation could be either enhanced or inhibited regarding the direction of the THz electric field. This study paves a way to ultrafast all-optical crystal symmetry control, which can be used in the high harmonic generation, optical frequency conversion, THz electric field measurement, and so on.

In chapter 6, I will firstly introduce the motivation of setting up a compact XUV beamline for our experiment. Then I will go into engineering details of how to set up this compact XUV beamline. A gated detection of XUV spectra method is introduced to improve the signal to noise ratio and some first results of XUV signals from MgO and NiO are shown. The XUV

emission from MgO shows HHG features, while the XUV emission from NiO does not behave as expected from harmonics. So more experiments and theoretical calculations are needed to understand this XUV emission mechanism. These results are based on joint work with Nicolai Klemke.

Chapter 2

Optical parametric amplification

2.1 Nonlinear optics background

In nonlinear optics, the optical response can often be described by expressing the optical polarization P as a Taylor expansion in terms of the laser electric field E as:

$$P(t) = \varepsilon_0 \left(\chi^{(1)} E(t) + \chi^{(2)} E^2(t) + \chi^{(3)} E^3(t) + \dots \right) \tag{2.1}$$

Here the coefficients $\chi^{(N\neq 1)}$ are the nonlinear optical susceptibilities of order N and $\chi^{(1)} = \chi$ is the linear optical susceptibility. For the example of the second order response to an electric field with two frequency components, we have

$$\begin{aligned} E(t) &= \frac{1}{2}\left(E_1 e^{i\omega_1 t} + E_2 e^{i\omega_2 t} + cc.\right) \\ P_{(2)}(t) &= \varepsilon_0 \chi^{(2)} E \cdot E \\ &= \frac{1}{4}\varepsilon_0 \chi^{(2)} \left(E_1^2 e^{i2\omega_1 t} + E_2^2 e^{i2\omega_2 t} + \right. \\ &+ 2E_1 E_2 e^{i(\omega_1+\omega_2)t} + 2E_1 E_2^* e^{i(\omega_1-\omega_2)t} + \\ &\left. + E_1 E_1^* + E_2 E_2^* + cc.\right) \end{aligned} \tag{2.2}$$

There are several terms of second order frequency mixing in $P_{(2)}(t)$:

- second harmonic generation (SHG) with the double frequencies,
- sum frequency generation(SFG),
- difference frequency generation (DFG),
- frequency zero optical rectification (OR).

To understand how the various frequency components of the field generate and become coupled by the nonlinear interaction, we need to start with Maxwell equation:

$$\begin{aligned} \vec{\nabla}\cdot\vec{D} &= \rho, \\ \vec{\nabla}\cdot\vec{B} &= 0, \\ \vec{\nabla}\times\vec{E} &= -\frac{\partial}{\partial t}\vec{B}, \\ \vec{\nabla}\times\vec{H} &= \vec{j}+\frac{\partial}{\partial t}\vec{D}. \end{aligned} \tag{2.3}$$

We assume the solution of these equations in regions of space that contain no free charges and no free currents, so that

$$\begin{aligned} \rho &= 0, \\ \vec{j} &= 0. \end{aligned} \tag{2.4}$$

For the non-magnetic, neutral media, we have

$$\begin{aligned} \vec{B} &= \mu_0\vec{H}, \\ \vec{D} &= \varepsilon_0\vec{E}+\vec{P}. \end{aligned} \tag{2.5}$$

So the curl equations could be written as:

$$\begin{aligned} \vec{\nabla}\times\vec{E} &= -\tfrac{\partial}{\partial t}\vec{B}, \\ \vec{\nabla}\times\vec{B} &= \mu_0\tfrac{\partial}{\partial t}\vec{D}. \end{aligned} \tag{2.6}$$

Here, if we take the curl of the first curl equation, switching the order of the derivatives and inserting the second curl equation, we have

$$\begin{aligned} \vec{\nabla}\times\vec{\nabla}\times\vec{E} &= -\mu_0\frac{\partial^2}{\partial t^2}\vec{D} \\ &= -\frac{1}{c^2}\frac{\partial^2}{\partial t^2}\vec{E}-\mu_0\frac{\partial^2}{\partial t^2}\vec{P} \\ &= -\frac{1}{c^2}\frac{\partial^2}{\partial t^2}\vec{E}-\mu_0\frac{\partial^2}{\partial t^2}\left(\vec{P}_1+\vec{P}_{NL}\right) \end{aligned} \tag{2.7}$$

By using an identity from vector calculus:

$$\begin{aligned} \vec{\nabla}\times\vec{\nabla}\times\vec{E} &= \vec{\nabla}\cdot(\vec{\nabla}\cdot\vec{E})-\vec{\nabla}^2E \\ \vec{P}_1 &= \varepsilon_0\chi^{(1)}\vec{E} \\ n^2 &= 1+\chi^{(1)} \end{aligned} \tag{2.8}$$

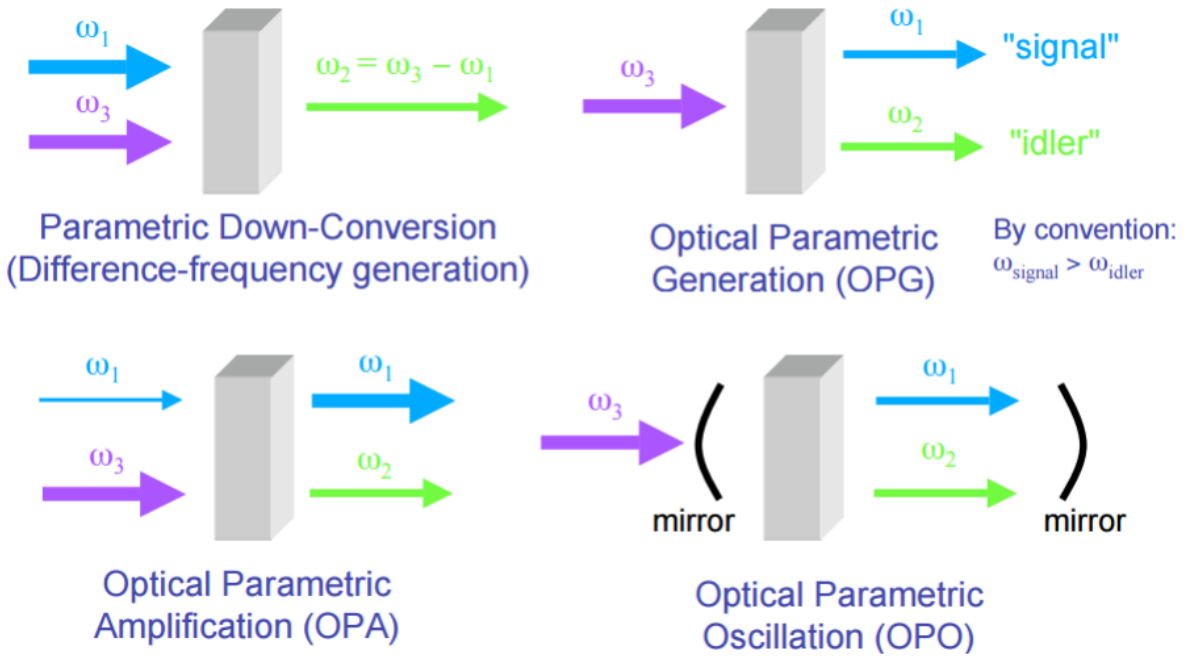

Fig. 2.1 second order nonlinear optical parametric processes. Adapted from ref [6]

Then, we can derive the nonlinear wave equation in the usual form:

$$-\vec{\nabla}^2\vec{E}+\frac{n^2}{c^2}\frac{\partial^2}{\partial t^2}\vec{E}=-\mu_0\frac{\partial^2}{\partial t^2}\vec{P}_{NL}. \tag{2.9}$$

2.2 Parametric process

A parametric process is an optical process in which the quantum state of the nonlinear material is not changed in the light-matter interactions. Therefore, the energy and momentum are conserved in this optical field [4]. In nonlinear optics, parametric processes include three-wave-mixing, four-wave-mixing, or higher order harmonic generation and self-phase modulation [5]. Fig. 2.1 shows a sampling of second order nonlinear optical parametric processes. As ω_1, ω_2 and ω_3 are sets of wavelengths to generate other sets. The energy conservation requires the relation $\omega_3 = \omega_2 + \omega_1$ should always hold.

2.3 Optical parametric amplification

An optical parametric amplification process is essentially DFG process, in which generated frequency ω_3 equals to the difference of the pump frequencies $\omega_1 - \omega_2$. The microscopic

mechanism of this process can be explained in Fig 2.1. A pump photon excites a virtual energy level and decays by a two-photon emission process which is stimulated by the presence of a signal photon. This leads to the emission of an identical second signal photon and an idler photon under conversion of energy and momentum. Therefore, the energy from the pump beam is transferred to the existing seed beam and the simultaneously borned idler beam. The optical parametric amplifier (OPA), which emits light of variable wavelengths by an optical parametric amplification process, is today one of the most widely used laser light source. To understand the amplification characteristics of an OPA, we assume the pump beam and seed beam propagating along the z direction, the corresponding waves can be expressed as the product of an envelope and a carrier:

$$\begin{aligned} E_p &= A_p(z) \cdot e^{i\left(\omega_p t - k_p z\right)} \\ E_s &= A_s(z) \cdot e^{i(\omega_s t - k_s z)} \end{aligned} \tag{2.10}$$

using the DFG term from equation (2.2):

$$P_i = \varepsilon_0 \chi^{(2)} A_p A_s^* e^{i(\omega_i - k_i z)} \tag{2.11}$$

Using the nonlinear wave equation (2.9), we obtain

$$\begin{aligned} \frac{dA_i}{dz} &= -\frac{i\chi^{(2)}\omega_i}{2n_i c} A_p A_s^* e^{-i\Delta k z} \\ \frac{dA_s}{dz} &= -\frac{i\chi^{(2)}\omega_s}{2n_s c} A_p A_i^* e^{-i\Delta k z} \\ \frac{dA_p}{dz} &= -\frac{i\chi^{(2)}\omega_p}{2n_p c} A_s A_i e^{i\Delta k z} \end{aligned} \tag{2.12}$$

Here $\Delta k = (k_p - k_s) - k_i$ is the phase mismatch. These coupled amplitude equations can already demonstrate some basic behavior of the OPA process. The evolution of the amplitude along the interaction length in the crystal is shown in Fig. 2.4. Initially, the buildup of both the signal and the idler is an exponential growth respectively with the nearly unchanged pump intensity. Then, comes the inflection point of the growth of both the signal and the idler as the pump's depletion sets in. As the decreasing growth rates of the signal and the idler approach zero, the maximum of both the signal and the idler and the minimum of the pump appear. After this phase, comes a back conversion from signal and idler to the pump frequency via sum frequency generation.

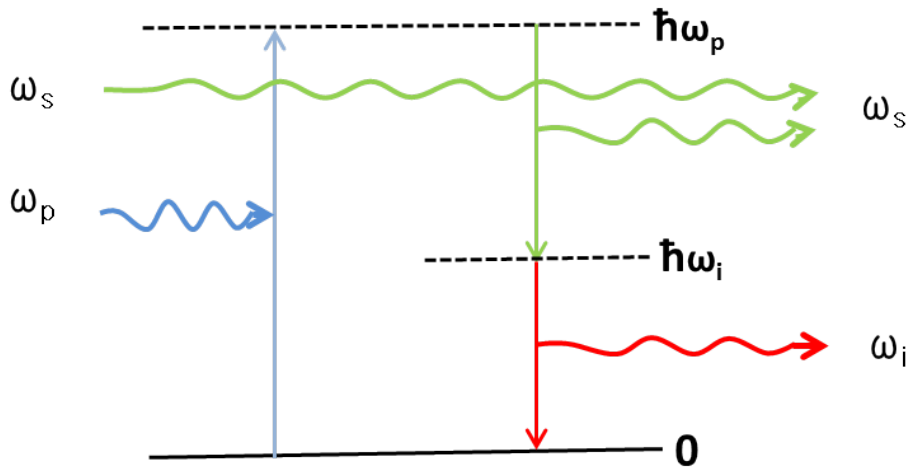

Fig. 2.2 The scheme of the OPA process. A pump photon excites a virtual energy level and decays by a two-photon emission process which is stimulated by the presence of the signal photon leading to the emission of an identical second signal photon and an idler photon under conversion of energy and momentum.

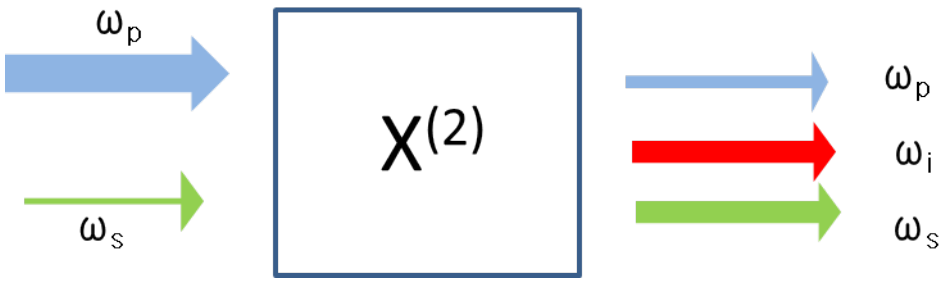

Fig. 2.3 In a $\chi^{(2)}$ process, the signal beam is amplified by the energy transfer from the pump beam. Simultaneously, the idler beam is generated via the DFG process and amplified the same way as the signal beam.

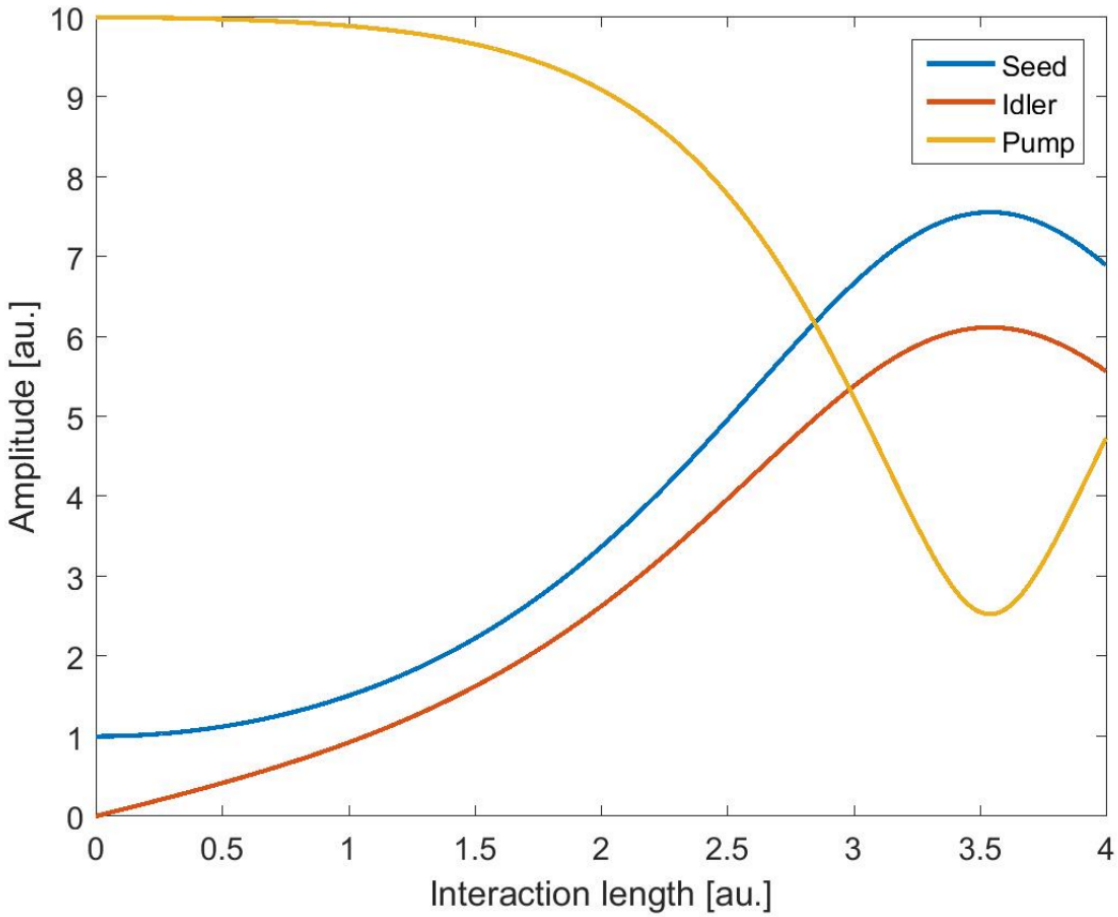

Fig. 2.4 Amplitude development in an OPA with propagation distance within the nonlinear crystal. Adapted from ref [7]

2.4 Home-built three-stage infrared OPA

In this section, I will introduce our home build three-stage OPA. The design of it is adapted from Liwei Song's previous work [8].

2.4.1 OPA design and setup

The design of our three-stage OPA is shown in Fig.2.6. The Ti:sapphire chirped-pulse amplifier (30 fs, 4.5 mJ, 3 kHz) is used as pump laser. The input diameter of it is $\sim$1 cm. The pump pulses are divided into four parts using three beam spliters. The smallest portion of the laser pulses ($< 30\mu J$), which transmits through BS3, focused into a 2-mm-thick sapphire plate and generate a single-filament white light continuum (WLC).

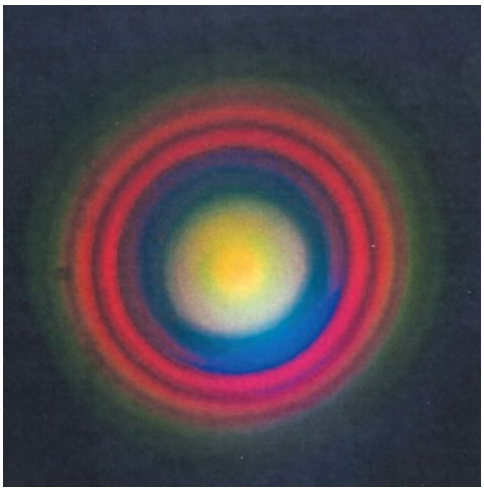

Fig. 2.5 The single-filament white light continuum (WLC).

This WLC works as the seed pulses for the following OPA stages and a variable neutral density filter (VND) is used for smooth adjustment of the pump beam energy inside the WLC. A fraction of the pump laser pulses with $\sim 120\mu$J pulse energy, reflected by BS3, is used to pump the first near-collinear OPA stage (OPA1) consisting of a 2.5-mm-thick BBO crystal cut for type II phase matching ($\theta = 27.2^\circ, \phi = 30^\circ$). The intersection angle between the pump and seed beams is $\sim 1^\circ$. After the OPA1, the WLC is amplified to $\sim 4\mu$J with the center wavelength at 1.44 μm and transit through the center of an aperture, while the rest of the pump beam is blocked by the edge of this aperture.

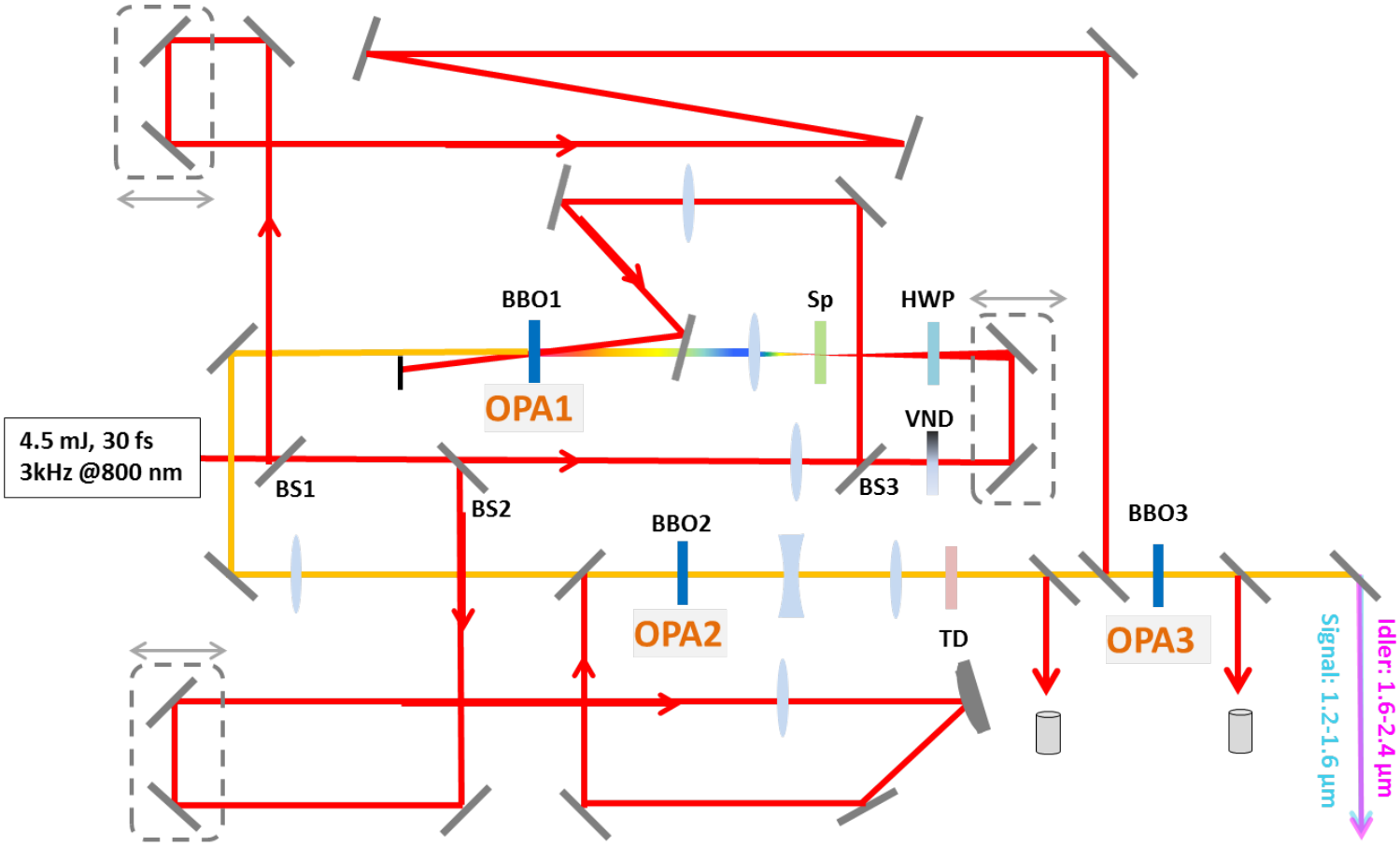

Fig. 2.6 OPA layout. VND, variable neutral density filter; HWP, half-wavelength waveplate; Sp, sapphire plate; TD, time delay crystal.

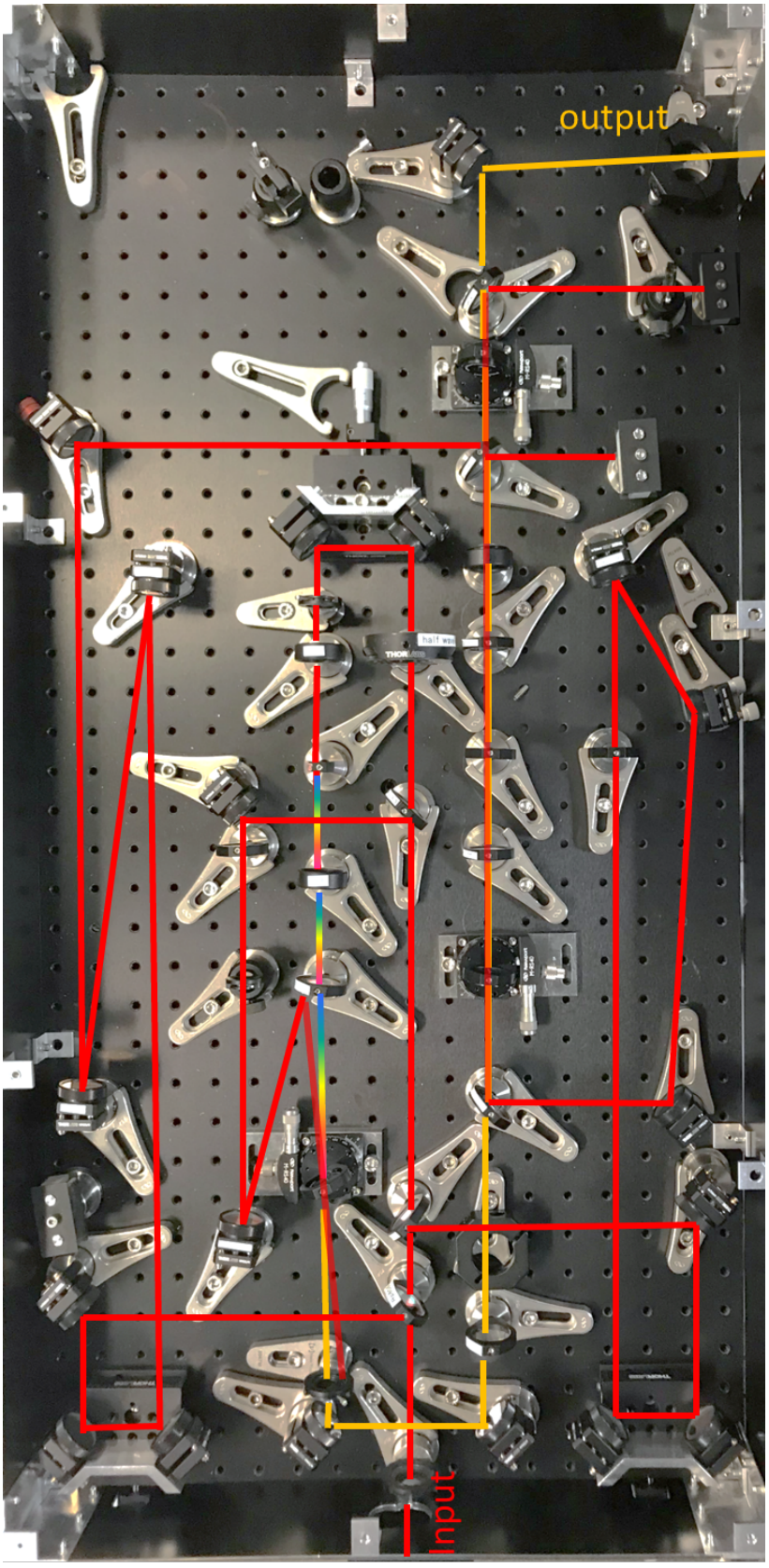

Fig. 2.7 OPA setup in the lab.

The amplified pulses at 1.44 μm from OPA1 are collimated and transit through the second collinear OPA stage (OPA2) consisting of a 2-mm-thick BBO crystal cut for type II phase matching ($\theta = 27.2^\circ, \phi = 30^\circ$). $\sim 720\mu$J laser pulse with a diameter of ~ 3.2 mm is used to pump OPA2, corresponding to a pump intensity near 250 GW/cm^2(the damage threshold of BBO). Both the signal and the pump beams are well collimated before injecting into the BBO crystal. The seed pulses are amplified to $\sim$90 μJ in this stage.

The amplified signal pulses from OPA2 are enlarged and collimated to $\sim$9 mm in diameter with a Galilean telescope. A 1.5-mm-thick a-cut YVO_4 crystal is employed as a time delay crystal to separate the signal and the idler pulses in time. Then the laser beam transmits through the third collinear OPA stage (OPA3) consisting of a 2-mm-thick BBO crystal cut for the same type II phase matching ($\theta = 27.2^\circ, \phi = 30^\circ$). The remaining $\sim$3.6 mJ pump laser with a diameter of $\sim$9 mm is used to pump OPA3. Similar to OPA2, the pump and the signal beams are collimated and collinearly hit the BBO crystal. Here, the collinear setup is quite necessary to avoid angular dispersion in the generated idler beam. The signal pulses are further amplified to $\sim$0.5 mJ at 1.44 μm, corresponding to the idler pulses with the energy of $\sim$0.4 mJ at 1.8 μm. Normally, it is necessary to optimize the grating-based compressor (both the angle of incidence and the separation distance) in the Ti: sapphire laser system to optimize the chirp of the pump laser to optimize the conversion efficiency.

2.5 Characterization of the OPA pulses

2.5.1 The principle of FROG

To characterize the full temporal shape of an ultrafast pulse with phase information, the FROG (Frequency Resolve Optical Gating), which was invented in 1991 by Rick Trebino and Daniel J. Kane [9], is the most widely-used method. The principle of FROG utilizes the pulse itself to gate the pulse with a variably delayed replica of the pulse in a nonlinear-optical medium. Then, by analyzing the resulting spectrally resolved trace, the retrieval of the pulse can be accomplished by using a FROG retrieval algorithm.

The schematic of a SHG-FROG measurement setup is shown in Fig. 2.8. The measured FROG spectrogram (also called FROG trace) is a graph of intensity as a function of frequency ω and delay τ:

$$I_{\mathrm{FROG}}(\omega,\tau) = \left|E_{\mathrm{sig}}(\omega,\tau)\right|^2 = \left|FT\left[E_{\mathrm{sig}}(t,\tau)\right]\right|^2 = \left|\int_{-\infty}^{\infty} E_{sig}(t,\tau)e^{-i\omega t}dt\right|^2. \tag{2.13}$$

Here, $E_{\mathrm{sig}}(t,\tau)$ is the nonlinear signal field which can be expressed as $E_{\mathrm{sig}}(t,\tau) = E(t)E(t-\tau)$. Therefore, we have

$$I_{\mathrm{SHGFROG}}(\omega,\tau) = \left| \int_{-\infty}^{\infty} E(t)E(t-\tau)e^{-i\omega t}dt \right|^2 . \tag{2.14}$$

By applying FROG retrieval algorithm [10], the signal E(t) can be retrieved from the FROG trace.

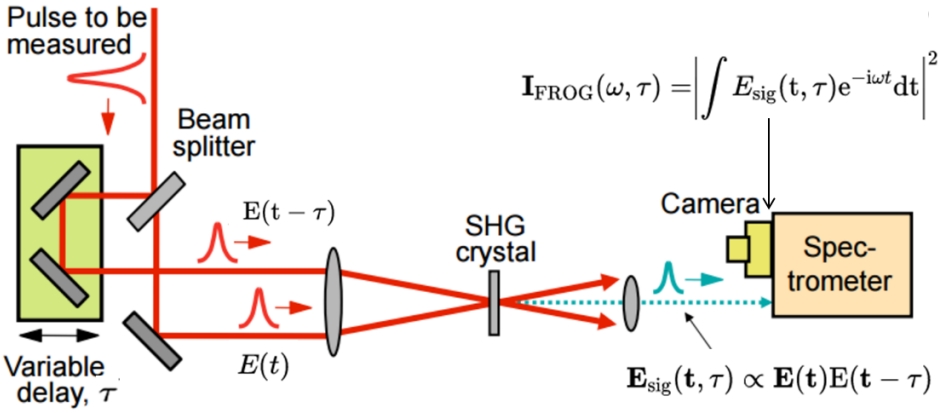

Fig. 2.8 Schematic of SHG-FROG measurement setup. Adapted from [11]

2.5.2 FROG measurement of the OPA pulses

The pulse duration of the output signal pulses of the OPA is measured by a home-built FROG setup when the highest conversion efficiency is obtained.

The signal pulse duration is ∼34 fs at 1.35 μm without any further pulse compression.

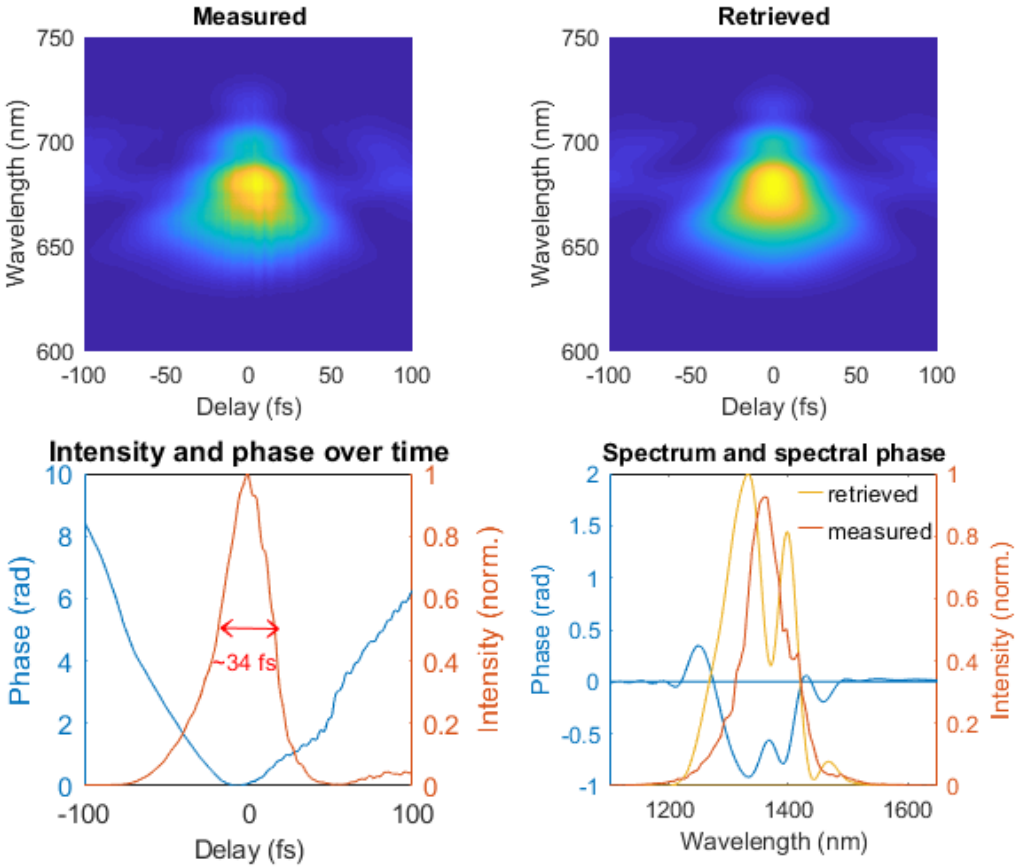

Fig. 2.9 FROG measurement and retrieval of the OPA signal pulses centered at 1.35 μm.

Chapter 3

Intense THz pulse generation and characterization

In this chapter, we explain the principles of generating ultrafast THz pulses with strong electric fields via optical rectification (OR) and the characterization of THz pulse via electro-optic sampling (EO-sampling). In particular, we highlight the tilted-pulse-fronts (TPF) technique[1] as well as OR in organic crystal DSTMS, since these two techniques will be exploited in the main experiments of this thesis:

- In the experiments of THz induced birefringence study in molecular liquids in chapter four, single-cycle THz pulse is generated in $LiNbO_3$ by optical rectification using the tilted-pulse-fronts technique at lower frequency THz (below 1 THz).

- In the experiemnts in chapter 5, organic crystal DSTMS with an extremely high nonlinear constant $\chi^{(2)}$ will be exploited for the ultrafast symmetry control of solids.

3.1 The THz range of the electromagnetic spectrum

The electromagnetic spectrum covers a rich range of wavelengths: from thousands of kilometers down to less than the size of an atomic nucleus. While we have explored many regions of this spectrum and make it for good use in the last century, there is still one mystery region between microwaves and infrared light waves called “terahertz gap”(shown in Fig.3.1), where technology for its generation and manipulation is in its infancy[13] compared to the relatively well-developed science and technology in the microwave and optical frequencies. This THz region (shown in Fig. 3.1), corresponding to the wavelength range of 3-0.03 mm (photons with a frequency between 300 GHz and 10 THz) and lies in the gap between the regimes of

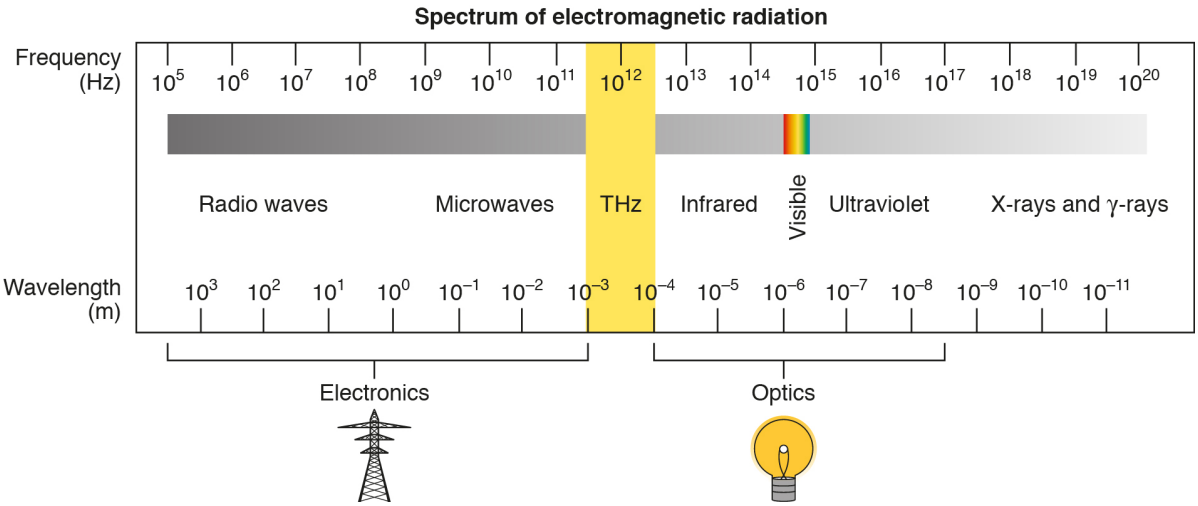

Fig. 3.1 Spectrum of electromagnetic radiation. The THz band lies between microwaves and infrared band.[12]

photonics and electronics, is the next frontier in science and technology [14]. In the last 30 years, the significant progress in THz technology [15, 16] and the development of laser-based THz time-domain spectroscopy triggered the field of THz science and technology expanded rapidly. As more intense THz sources and higher sensitivity detectors become available, it leads to a wide variety of interesting applications from fundamental science like the fundamental carrier dynamics phenomena and phonon/vibrational modes of various materials systems to 'real world' applications such as THz imaging and spectroscopy, security, medical applications, food, construction, and the pharmaceutical industry[17].

3.2 Ultrafast THz pulse generation techniques

Table 3.1 shows a summary of the comparison between the THz generation techniques and the overview of intense laser-based THz sources are shown in Fig. 3.2 [17]. The photoconductive (PC) antenna generates and detects THz pulses by transient photocarriers induced with ultrafast laser pulses [14]. It is widely employed in THz time-domain spectroscopy to analyze material linear properties, while its THz peak electric field is not high enough to induce nonlinear material effects. Plasma in air generates frequencies across the entire THz spectrum, but the efficiency tends to be very low and suffers from shot-to-shot instability. Optical rectification (OR) is a simple approach to generate high conversion efficiency, high stability, and high peak field. To study nonlinear effects in condensed matter with strong electric fields, we would discuss the principle of optical rectification (OR) in detail in the next section.

Table 3.1 Summarized comparison between the THz generation techniques and the advantages and disadvantages of each technique. Adapted from ref [18]

	Optical rectification	Photoconductive antenna	Air-plasma
THz radiation properties	• Single to multi-cycle THz pulses with peak fields from several 100 kV cm^{-1} up to several MV cm^{-1} • Broad bandwidth, from 0.1 THz to 6 THz, depending on the nonlinear crystal	• Asymmetric quasi half-cycle THz pulses with peak field of few hundreds kV cm^{-1} • Low THz frequencies (0.1-1 THz) • Picosecond pulse duration • Large spot size ($\geqslant$2.5 mm)	• Single-cycle THz up to MV cm^{-1} with conical emission profile • Broad bandwidth from 0.1 to 10 THz and over
Advantages	• High conversion efficiency – in organic crystals 3% – in lithium niobate 1% • Simple experimental configuration • High stability	• Large ponderomotive potential • High stability • Extraction of THz energy from the bias voltage	• No concerns for damage with air • Whole THz region covered without gap • High electric field
Disdvantages	• Laser damage threshold of the nonlinear medium • Complicated phase-matching conditions for some crystals • Thermal and multi-photon effects in the crystal when pumping with high laser intensities	• Relatively low THz peak electric field • Laser damage threshold of the antenna • High electromagnetic noise • THz radiation saturation at low optical fluence • Short life-time of the emitter	• Shot-to-shot instability • Low energy level and low conversion efficiency ($< 0.1\%$) • Conical shape

.

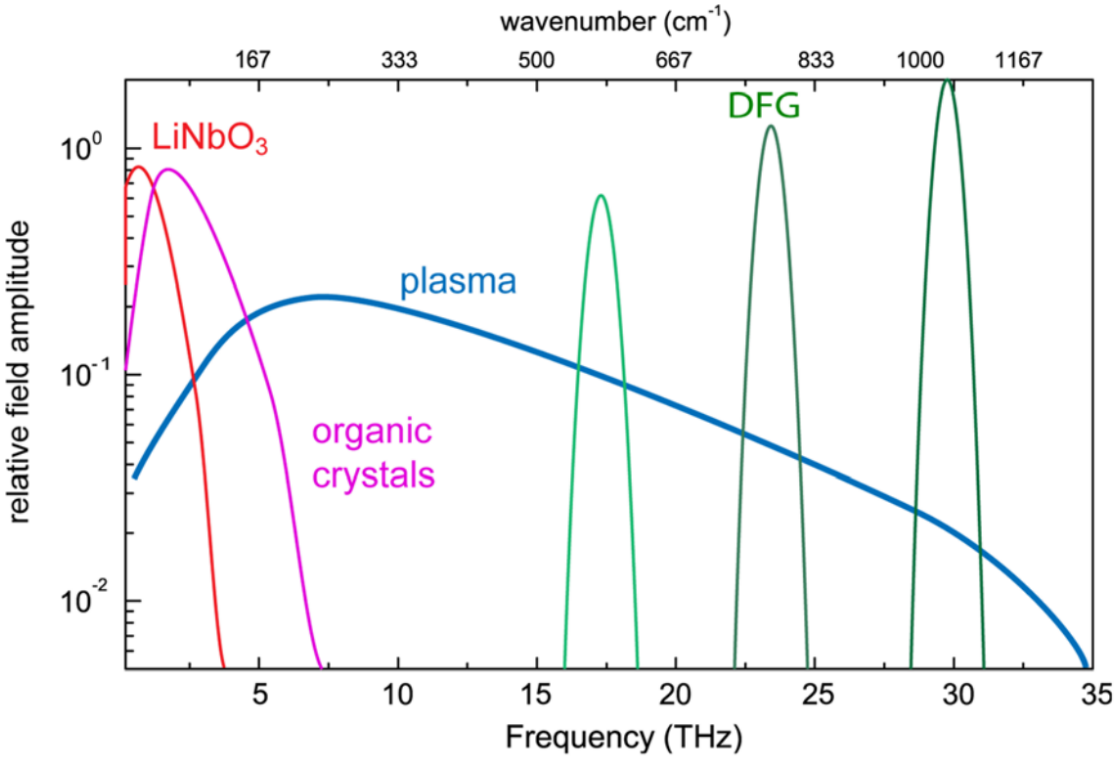

Fig. 3.2 Overview of intense laser-based THz sources: optical rectification in $LiNbO_3$ or nonlinear organic crystals results in broadband, single-cycle pulses. Ionization of plasmas produces ultra-broadband pulses with a wide frequency spectrum. Difference frequency mixing (DFG) of optical parametric amplifiers delivers narrowband tunable mid-infrared pulses. Adapted from [17]

3.3 Optical rectification

Optical rectification (OR) is a second-order nonlinear process that generates the quasi-DC polarization when an intense optical pulse passes in noncentrosymmetric materials. It is a difference-frequency generation process with the frequency difference close to zero. Different frequency components in a pulse can mix with each other in the NLO material, producing a broadband THz pulse.

In nonlinear optics, the second order susceptibility $\chi^{(2)}$ of the material is related to the THz generation via the following formulas[18]:

$$P_{OR}^{(2)}(\Omega) = \varepsilon_0 \chi^{(2)}(\Omega = \omega_2 - \omega_1; \omega_1, -\omega_2) E(\omega_1) E^*(\omega_2) \tag{3.1}$$

Here,in Equation(3.1), Ω is the frequency difference between two frequency components of the optical pump ω_1 and ω_2 . This process is schematically shown in Fig. 3.3.

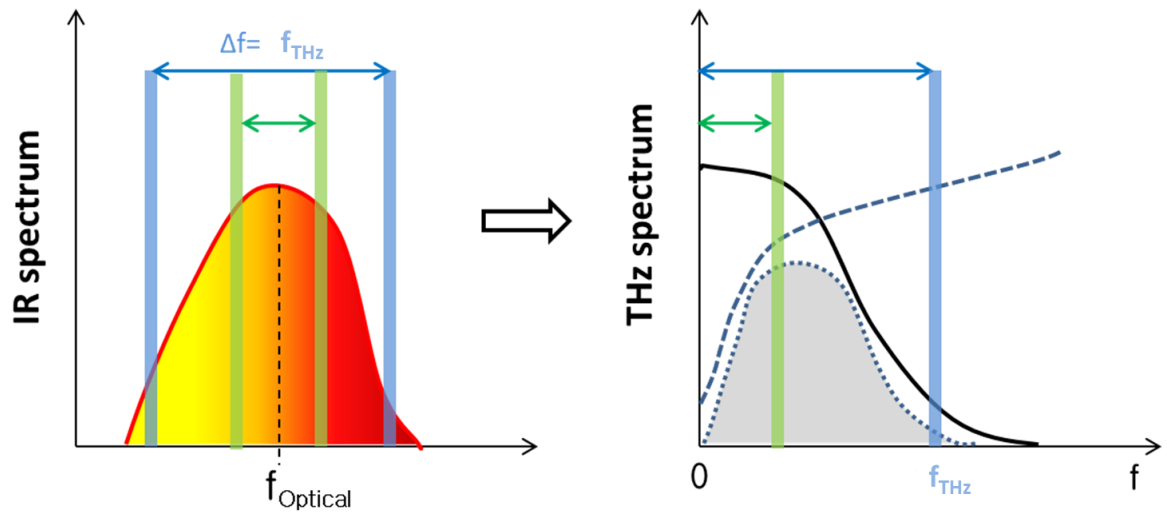

Fig. 3.3 Spectral diagram of intrapulse difference frequency generation of IR pulse (optical rectification) yielding a THz pulse.

The temporal THz field $E^{\mathrm{rad}}_{\mathrm{THz}}(t)$ can be derived from the second derivative of the change of the polarization (Fourier transformed in the time domain) with respect to time t :

$$E^{\mathrm{rad}}_{\mathrm{THz}}(t) \propto \frac{\partial^2 P^{(2)}_{OR}(t)}{\partial t^2}. \tag{3.2}$$

In a first approach [19] which considering:

1. non-depleted pump approximation,
2. negligible optical and THz absorption,
3. plane-wave approximation,
4. perfect phase-matching,

the intensity of the generated THz wave is in frequency domain is given by [19]

$$\begin{aligned} I(\omega_{\mathrm{THz}}, L) &= \frac{1}{2}\varepsilon_0 c n_{\mathrm{THz}} |E(\omega_{\mathrm{THz}}, L)|^2 \\ &\approx \frac{d^2_{\mathrm{THz}} I_0^2 \omega^2_{\mathrm{THz}} L^2}{2\varepsilon_0 c^3 n_o^2 n_{\mathrm{THz}}}. \end{aligned} \tag{3.3}$$

Here

$$d_{\mathrm{THz}} = \frac{1}{4} n_o^4 r \tag{3.4}$$

is the nonlinear coefficient for THz-wave generation that scales with the electro-optic coefficient r[20], I_0 the pump intensity, n_o and n_{THz} the refractive indices at the pump optical and the generated THz frequencies, respectively. the conversion efficiency is

$$\eta = \frac{I(\omega_{\mathrm{THz}}, L)}{I_0} = \frac{d_{\mathrm{THz}}^2 I_0 \omega_{\mathrm{THz}}^2 L^2}{2\varepsilon_0 c^3 n_o^2 n_{\mathrm{THz}}} = \frac{1}{2\varepsilon_0 c^3} \mathrm{FM}_{\mathrm{THz}} \omega_{\mathrm{THz}}^2 I_0 L^2, \tag{3.5}$$

where the main material figure of merit for THz-wave generation FM_{THz} is given by [19]

$$\mathrm{FM}_{\mathrm{THz}} = \frac{d_{\mathrm{THz}}^2}{n_o^2 n_{\mathrm{THz}}} = \frac{n_o^6 r^2}{16 n_{\mathrm{THz}}}. \tag{3.6}$$

3.3.1 phase-matching conditions

To generate high energy THz pulses with high efficiency, the phase-matching conditions $\Delta\mathbf{k} \approx 0$ should also be fulfilled and $\Delta\mathbf{k}$ is given by :

$$\Delta\mathbf{k} = \mathbf{k}_{\mathrm{THz}} - (\mathbf{k}_1 - \mathbf{k}_2). \tag{3.7}$$

Here, $\mathbf{k}_{\mathrm{THz}}$ is the wave vector of THz with the amplitude $|\mathbf{k}_{\mathrm{THz}}| = 2\pi n_{\mathrm{THz}}/\lambda_{\mathrm{THz}}$, and k_1, k_2 are the two wave vectors of the two interacting fields $\mathbf{E}(\omega_1)$ and $\mathbf{E}(\omega_2)$ in the optical pump with the magnitude of $|\mathbf{k}_i| = 2\pi n_i/\lambda_i$ (i=1,2), respectively. For collinear propagation, since the THz wave frequency Ω is far less than the center frequency of the optical pump , the phase mismatch can be expressed as:

$$\begin{aligned} \Delta k(\Omega) &= k(\Omega) + k(\omega) - k(\omega + \Omega) \\ &\approx k(\Omega) - \Omega \frac{dk}{d\omega}\bigg|_{\omega_0} \\ &= \frac{\Omega}{c} \left[n(\Omega) - n_g(\omega_0) \right], \end{aligned} \tag{3.8}$$

where ω_0 is the center frequency of the optical pump pulse. This means the phase mismatch is proportional to the difference between the phase index of THz and group index of optical pulse. Consequently, the low refractive index mismatch is crucial to have an efficient OR process.

Table 3.2 shows the parameters of several candidates of nonlinear materials for THz generation. For organic materials, the phase-matching conditions are almost naturally satisfied. However, for nonlinear inorganic crystals such as $LiNbO_3$, the phase-matching conditions are not directly possible. To overcome this problem, the tilted-pulse-front (TPF) technique[1] is thus proposed, which uses the noncollinear phase-matching geometry. A detailed discussion about this will be followed in the next subsection.

Table 3.2 Selection of organic and inorganic NLO materials that have been investigated for THz-wave generation and their most relevant parameters. The parameters are given close to the optimal phase-matching range: refractive index n_o and the group index n_g at the pump optical wavelength λ; refractive index n_{THz} in the THz range; the electro-optic coefficient r; the NLO coefficient d_{THz} for THz-wave generation; the figure of merit FM_{THz} for THz-wave generation. Adapted from ref[19]

Material	n_o	n_g	n_{THz}	r (pm/V)	$d_{THz}(pm/V)$	$FM_{THz}\ (pm/V)^2$	λ (nm)
DAST	2.13	2.26	~ 2.3	47	240	5600	1500
DSTMS	2.08	2.19	~ 2.2	50	230	5800	1500
OH1	2.16	2.33	~ 2.3	52	280	7500	1300
ZnTe	2.85	3.2	~ 3.2	4	66	170	800
GaP	3.12	3.36	~ 3.35	1	24	17	1000
$LiNbO_3$	2.16	2.22	~ 5	30	160	1100	1000

For extremely strong-field THz generation, the most promising approach is to generate single-cycle broadband THz radiation with femtosecond laser pulses in organic crystal or lithium niobate crystal. Presently, THz pulse energies of 0.9 mJ and conversion efficiency of 3.0% were realized by using the organic crystal (DSTMS)[21], which covered the spectra range mostly from 2 to 10 THz. For lower frequency below 2 THz, $LiNbO_3$ has a record of 0.4 mJ THz pulse energy[22].

Table 3.3 Experimentally achieved THz parameters in different materials used for optical rectification.

Parameter	$LiNbO_3$[22]	ZnTe	DSTMS[23]
Frequency	0.14 THz	0.7 THz	3.0 THz
Energy	436μJ	14μJ	900μJ
Pulse duration	3.2 ps	0.85 ps	0.36 ps
Electric field E	1.05 MVcm^{-1}	1.0 MVcm^{-1}	48.4 MVcm^{-1}

3.3.2 Tilted-pulse-front technique in lithium niobate

The principle of the tilted-pulse-front (TPF) technique[1] exploits a noncollinear phase-matching geometry to fulfill the phase-matching conditions in Equation 3.7 in $LiNbO_3$. However, in normal noncollinear phase-matching configuration, the THz wave and optical beam suffer from walking away from each other in a short distance. The TPF technique cleverly avoids this by introducing a tilt angle of γ in the optical pulse front with respect to the phase front. A schematic illustration of TPF technique is shown in Fig. 3.4. The pump laser is incident on a grating, which is used to tilt the intensity front of the pump pulses. According to Huygens' principle, the THz radiation excited by the tilted pulse front of the optical pump

propagates perpendicularly to this front with a velocity v_{THz}. Therefore, the angle between the propagation direction of the THz radiation and the propagation direction of the pump pulse will be the same as the tilt angle γ. This leads to:

$$v_{\mathrm{THz}}^{\mathrm{ph}} = v_{\mathrm{pump}}^{\mathrm{gr}} \cos(\gamma). \tag{3.9}$$

With this in the noncollinear phase-matching geometry, the phase mismatch will be

$$\Delta k \approx \frac{\Omega}{c}\left[n(\Omega) - \frac{n_g(\omega_0)}{\cos\gamma}\right] = 0. \tag{3.10}$$

phase-matching conditions fulfilled!

For the experimental implementation of TPF technique, Mg doped stochiometric $LiNbO_3$ (sLN) is used to reduce the photorefractive effect (resulting in a lower loss of the pump laser) [24]. When pumped by 800nm ti:saphire laser in room temperature, the optical refractive index and the THz refractive index inside sLN crystal are 2.25 [25] and 4.96 [24], respectively. Therefore, we could set

$$\gamma = \cos^{-1}\frac{n_q(\omega_0)}{n(\Omega)} = \cos^{-1}\frac{2.25}{4.96} \approx 63^\circ \tag{3.11}$$

to fulfill phase-matching.

3.4 Nonlinear organic crystals

As early as 1992, the generation of THz pulses through optical rectification in organic crystalline salt DAST (4-N, N-dimethylamino-4'-N'-methyl stilbazolium tosylate) has been reported[26]. Since then, nonlinear organic crystals with their record-high second-order optical nonlinearity play a vital role to advance the progress of strong-field THz generation technology. Compared to $LiNbO_3$, Organic crystals have the following advantages:

- Higher optical nonlinearity hence higher conversion efficiency,
- No pulse front tilting required hence easy alignment,
- Low THz absorption coefficient hence no cryogenic cooling required,
- Low dielectric constant hence small Fresnel loss,
- Broad THz spectrum.

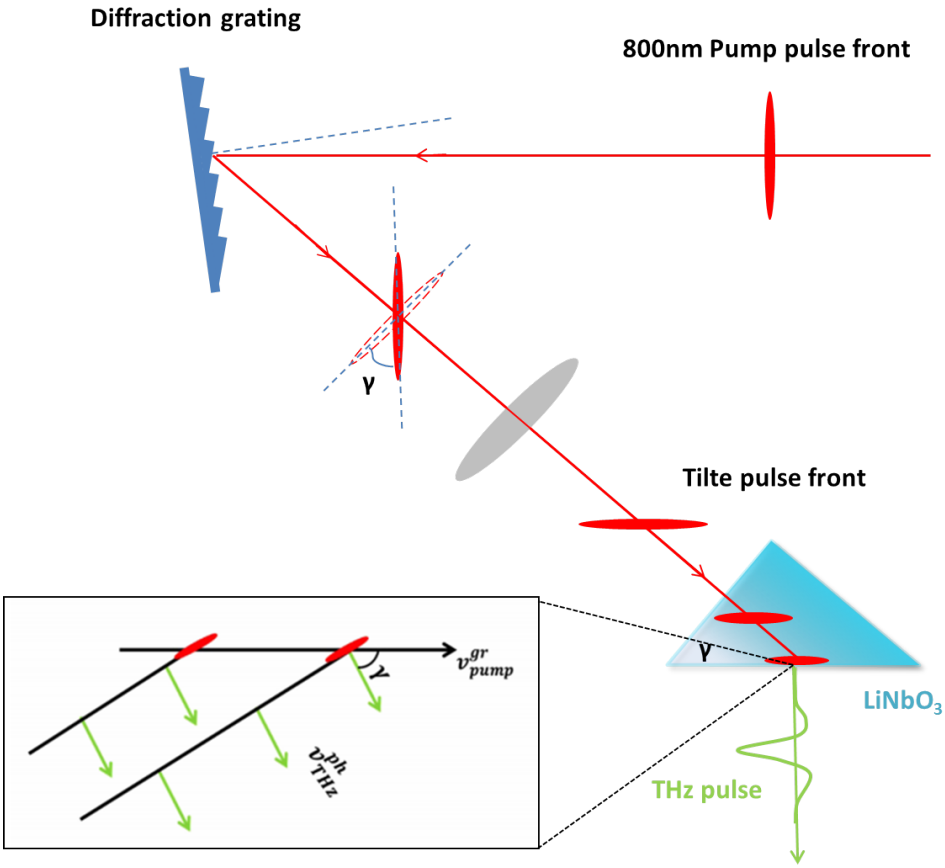

Fig. 3.4 Experimental setup scheme for THz generation by titled-pulse-front technique in $LiNbO_3$. An optical diffraction grating is used to title the pulse front.

Disadvantages

- Long pump wavelength (1.0-2µm) required hence limited in pump energies
- Low damage threshold
- Small crystal size available (< 2 cm x 2 cm)

3.4.1 Properties of DSTMS

The 4-N,N-dimethylamino-4'-N'-thyl-stilbazolium 2,4,6-trimethylbenzenesulfonate (DSTMS) molecular unit is composed of a positively charged stilbazolium chromophore and a counter-anion. In this way, it could shape noncentrosymmetric packing in the crystalline phase, which leads to a high second-order optical nonlinearity feature.

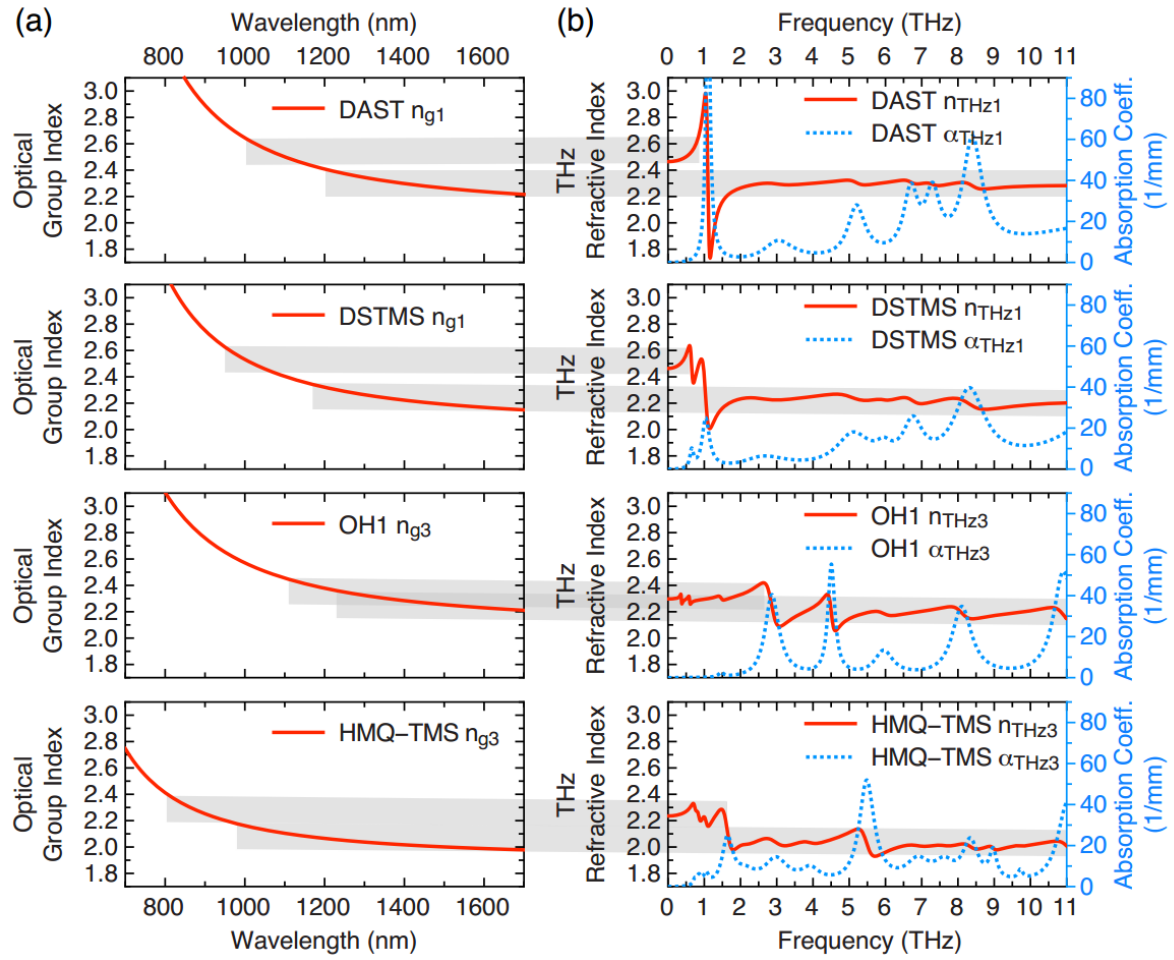

Fig. 3.5 (a) optical group index $n_g(\lambda)$ as a function of wavelength for selected organic crystals; (b) optical properties in the THz range: the refractive index $n_{\mathrm{THz}}(f)$ (red solid curves) and the absorption coefficient $\alpha_{\mathrm{THz}}(f)$ (blue dotted curves, right scale) as a function of frequency $f = \omega/(2\pi)$. The corresponding properties are given for selected organic crystals along their polar axis, which is most often employed in THz applications. Adapted from ref[19]

3.5 THz generation via DSTMS

For our THz source in the lab, the THz generator DSTMS is mounted on a 1-inch disc with aperture 5mm, thickness 490 μm (Shown in Fig.3.7). The waveform we generated from it is shown in Fig. 3.8.

3.6 Electro-optic sampling

Electro-optic(EO) sampling [28, 29] is a widely-used technique, to measure the electric field of a long-wavelength pulse(THz or far-infrared beam) utilizing the ultra short optical pulse as

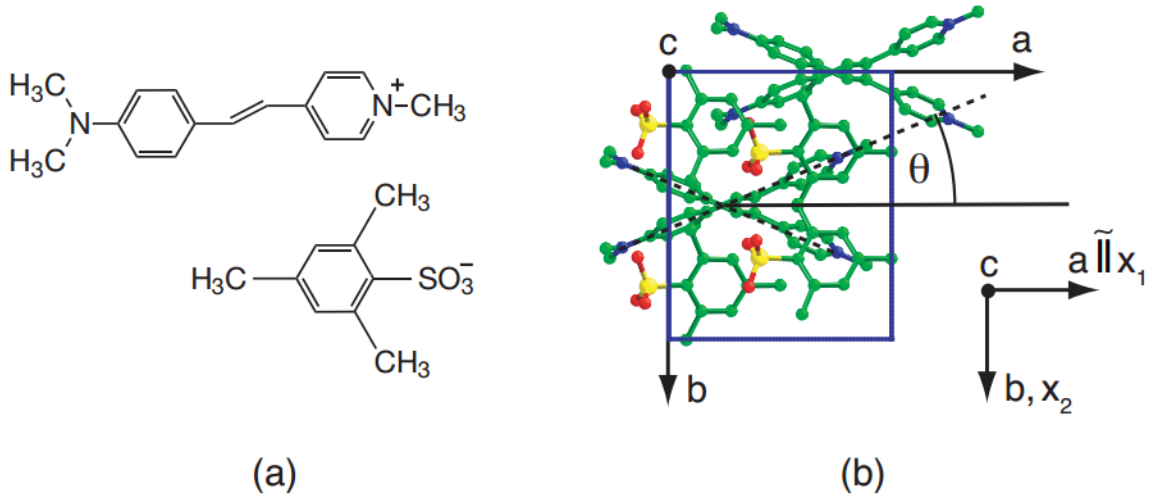

Fig. 3.6 (a) Positively charged nonlinear optical active chromophore stilbazolium and negatively charged 2,4,6-trimethylbenzenesulfonate anion. (b) Arrangement of the molecules in the unit cell as viewed along the c axis. adapt from ref[27]

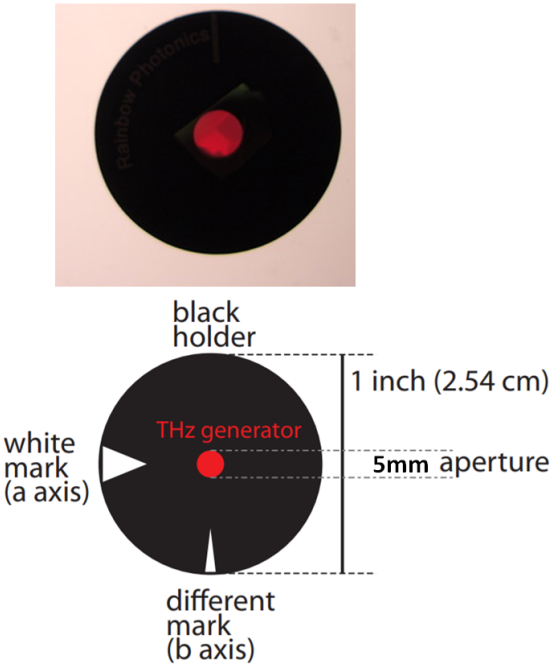

Fig. 3.7 THz generator DSTMS mounted on a 1-inch disc with aperture 5mm, thickness 490 μm

the probe. It can be treated as a reciprocal process of the optical rectification and exploits the birefringence induced in a crystal (usually with zincblende structure such as ZnTe, GaP) via the linear electro-optic effect. In this process, the refractive index difference for polarizations along different axes of the crystal in the eo material induced by THz wave is proportional to

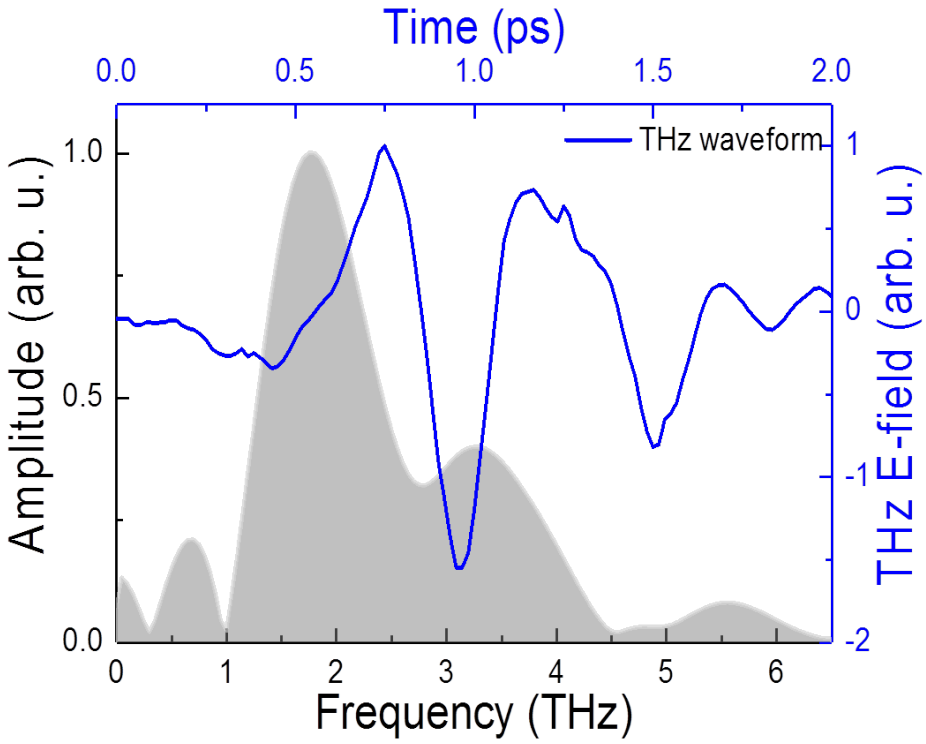

Fig. 3.8 THz waveform from DSTMS.

the THz electric field amplitude E_{THz} by :

$$\Delta n_{\mathrm{o}} = -\frac{n_{\mathrm{o}}^3}{2} r E_{\mathrm{THz}}, \tag{3.12}$$

where r is the exploited element of the electro-optic tensor. The change in the refractive index Δn_o proportionally modulates the polarization state of the optical probe pulse, causing the intensity change which could be detected by an electro-optic detector. As the period of THz electric field is much longer than the co-propagating optical probe pulse duration, the full THz waveform can be directly mapped in time through scanning the time delay between the optical probe and THz pulse.

A typical EO sampling setup is shown in Fig.3.9. A THz pulse and IR probe pulse overlapped in time pass through an EO crystal (typically ZnTe or GaP), both with linear polarization. The THz E-field modifies the refractive index ellipsoid of the EO crystal and leads to a difference in phase between the polarization components parallel to the crystal's a-axis and c-axis. This phase retardation results in an elliptical IR polarization at the output of the crystal and each step of the polarization configuration of IR is shown in fig.3.9. For [110] cut

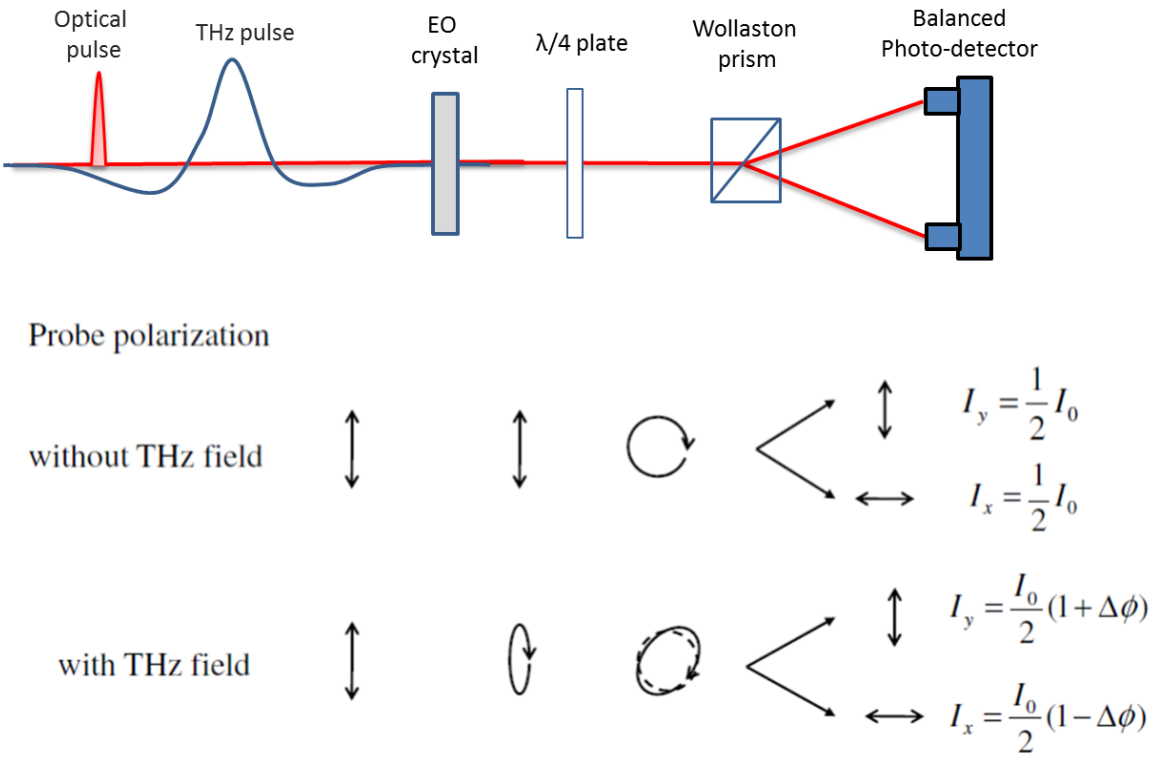

Fig. 3.9 schematic illustration of EO-sampling with balanced detection for THz detection.

EO crystal, the phase retardation induced by the THz field is given by[30]:

$$\Delta\phi = \frac{\omega L}{c} n_o^3 r_{41} E_{THz} \tag{3.13}$$

where L is the thickness of the crystal,n_o is the refractive index of the crystal in the optical range, r_{41} is the electro-optic coefficient of the crystal along the axis parallel to the THz polarization.

After transmitting through a $\lambda/4$ plate and a polarization-state analyzer such as Wollaston prism, the phase retardation of IR polarization can be measured by the intensity difference of a balanced photo-detector. This intensity difference between the two signals can be expressed in the following equations [18]:

$$I_s = I_y - I_x = I_0 \Delta\phi = \frac{I_0 \omega L}{c} n_o^3 r_{41} E_{THz} \tag{3.14}$$

with

$$I_x = \frac{I_0}{2}(1 - \sin\Delta\phi) \approx \frac{I_0}{2}(1 - \Delta\phi) \tag{3.15}$$

$$I_y = \frac{I_o}{2}(1+\sin\Delta\phi) \approx \frac{I_0}{2}(1+\Delta\phi) \tag{3.16}$$

Here we assume the phase retardation $\Delta\phi \ll 1$ for small angles, and I_s is the signal of the balanced photodetector. I_0 is the total intensity of the IR. Therefore, in a balanced measurement, the signal is linearly proportional to the electric field of the THz radiation.

The sensitivity of the EO sampling setup can be increased by modulating the pump beam with an optical chopper, and the THz-induced modulation on the probe beam is extracted by a lock-in amplifier. The spectral information can be captured by the Fourier transform of the full THz waveform in the time domain.

Chapter 4

THz induced birefringence study in molecular liquids

In this chapter, we investigate the THz-field induced birefringence study in molecular liquids utilizing the Kerr effect. In contrast to optical or near-infrared excitation, THz photons have frequencies below the intra-molecular vibrations and therefore leave the internal structure of the molecule mostly unaffected. We find experimental evidence for a THz-induced optical birefringence, which provides evidence for molecular orientation. Moreover, by studying liquid water, using a combination of THz pump and optical probe experiments, we demonstrate a transient orientation of their dipole moments, which is not possible by optical excitation. The resulting birefringence reveals that the polarizability of water is lower along its dipole moment than the average value perpendicular to it. This anisotropy, also observed in heavy water and alcohols, increases with the concentration of sodium iodide. Our results enable a more accurate parametrization and a benchmarking of existing and future water models.

These results are joint work with Peter Zalden and Liwei Song. The THz generation setup was built by Xiaojun Wu.

4.1 Kerr effect in liquids

As early as 1875, Kerr revealed that an isotropic liquid would become optically anisotropic or birefringent when a strong electric field is applied[31]. This phenomenon is known as Kerr effect.

Quantitatively, Kerr electro-optic effect states that the lowest-order change in the refractive index of the isotropic liquid depends quadratically on the strength of the applied static (or

low-frequency) field. We can describe this relationship by defining the Kerr coefficient B:

$$n_{\parallel} - n_{\perp} = \lambda B E^2, \tag{4.1}$$

where $n_{\parallel(\perp)}$ is the refractive index for light polarized parallel (perpendicular) to the direction of the applied electric field E and λ is the wavelength of the probe pulse traversing the liquid.

In a microscopic picture, the presence of an external electric field tends to orient the dipole moments of liquid molecules along the field direction and results in a fractional orientation in a liquid along this direction. This preference of molecules' alignment along the electric field direction causes macroscopic dielectric anisotropy and leads to the optical birefringence phenomenon (DC kerr effect), which could be used to detect the amount of molecular orientation. The field-induced anisotropy saturates when all the molecules have orientated along the field direction. In water, this threshold field strength is around 250 kV/cm [32], which is achievable from single-cycle THz sources in crystals like $LiNbO_3$ [1].

In a recent study, Hoffmann *etal*. pioneered the application of single-cycle electromagnetic pulses in the THz regime to induce birefringence in liquids [33, 34]. In his experimental results (Fig. 4.1), at the beginning, the Kerr signal follows the square of terahertz field, but after the terahertz pulse there is still a slow exponential response which is related to the molecular orientation. Relaxation time of 1.7 ps was obtained, which corresponds to the timescale of intermolecular dynamics [35].

4.2 Water molecule in strong electric field

A water molecule H_2O consists of one strongly electronegative oxygen atom bonded to two weakly electropositive hydrogen atoms. As a polar molecule, water molecule has a permanent dipole moment μ_i along its rotational symmetry axis. When an external electric field E_i is applied onto the water molecule, the interaction energy is dominated by the contribution of permanent dipole moment μ_i and polarizability α (induced dipole moment) as :

$$W = -\sum \mu_i E_i - \frac{1}{2}\sum \Sigma \alpha_{ij} E_i E_j - \ldots \tag{4.2}$$

where α_{ij} is the polarizability tensor. For the polarizability tensors in water molecule, we can define α_{zz} along the direction of permanent dipole moment μ_i, α_{xx} along the direction span the two hygrogen atoms and α_{yy} along the direction perpendicular to the water molecule plane (shown in figure 4.2).

The goal of our work is to use the Kerr effect to measure $\Delta\alpha = \alpha_{\parallel} - \alpha_{\perp}$, i.e., the difference of the polarizability along the permanent dipole moment, $\alpha_{\parallel}$, and the average value perpendicular

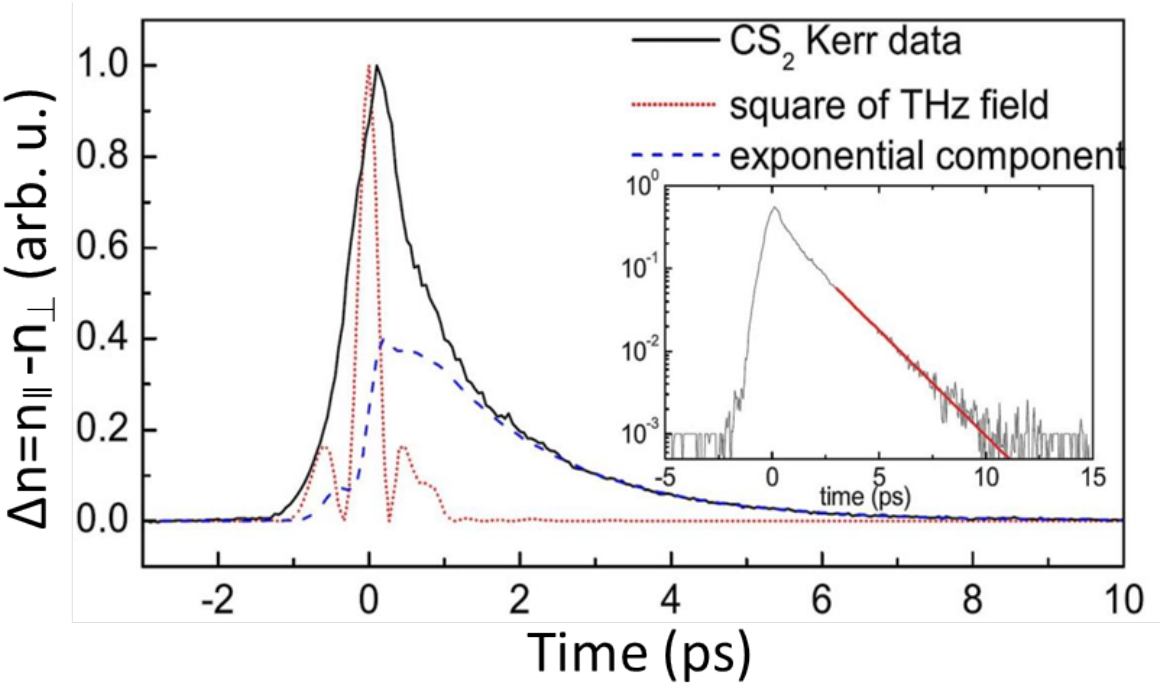

Fig. 4.1 Kerr signal in CS_2 vs THz E-field [33]. At the beginning the Kerr signal follows the square of terahertz field, but after the terahertz pulse there is still a slow exponential response which is related to the molecular orientation. Adapted from [33]

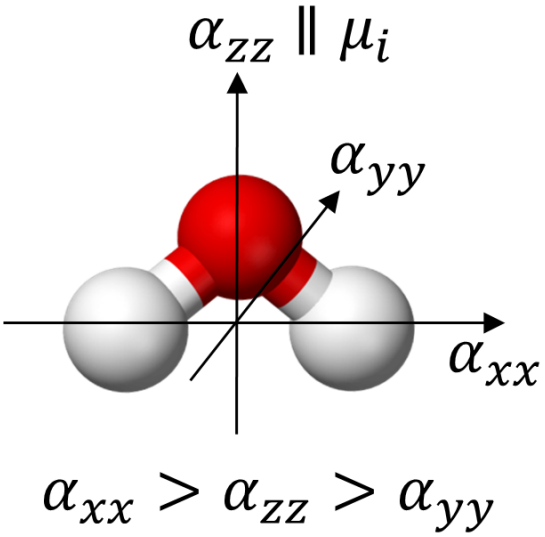

Fig. 4.2 The polarizability tensors of water molecule.

to it, $\alpha_\perp$. At present, the sign of $\Delta\alpha$ is still unknown but is vital to build an accurate water model. To determine whether the polarizability (and refractive index) of water would increase

(or decrease) upon application of an electric field that orients the dipole moments, we exploit the THz-induced Kerr effect (TKE) to have the first experimental determination of $\Delta\alpha$ of water in the liquid state. Our results would imply that the polarizability of water molecules is smaller parallel to the dipole moment than the average value perpendicular to it [36].

4.2.1 Dynamics of water in THz

The intermolecular hydrogen bonds form when an electromagnetic attraction created between the oxygen atom of one water molecule and the hydrogen atom(s) of one or two neighboring molecules. Water dynamics in the terahertz (THz)-regime is dominated by the intermolecular

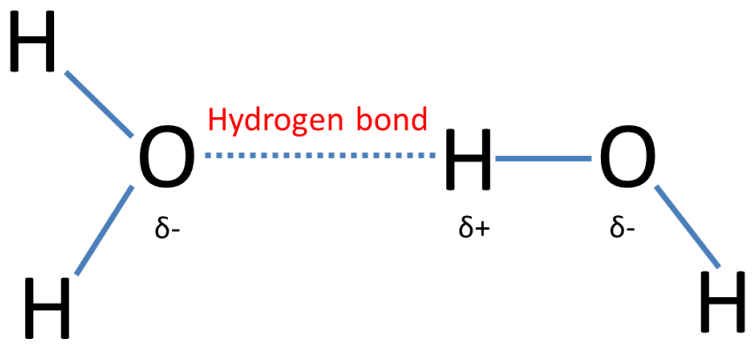

Fig. 4.3 The hydrogen bond in water.

forces of the hydrogen-bond network [37], which is held responsible for many of its anomalous properties [38]. While there is a recent consensus that these dynamics consist of three relaxation mechanisms [39, 40], their microscopic origin is still under debate [37]. Most commonly, they are associated with the rotation or libration of water molecules. At frequencies below $\sim$ 1 THz, the co-operative reorientation of water molecules is considered the dominating absorption mechanism [40]. To reveal this orientation mechanism in water, we measure the THz-induced Kerr effect (TKE) [36]. At these frequencies, the orientation of the water molecules can follow the electric field. The optical Kerr effect (OKE), on the other hand, is induced by visible or NIR pulses and is based on an alignment of the axes of highest polarizability with the laser field [41], and therefore cannot directly induce co-operative orientations of water molecules.

4.2.2 Kerr effect in water

Liquid water as solvent influences chemical reactions of proteins [43], and its structure and dynamics cause many of the anomalous properties, such as compressibility, density variation, and heat capacity [38]. These anomalous properties, essential for life, originate from the

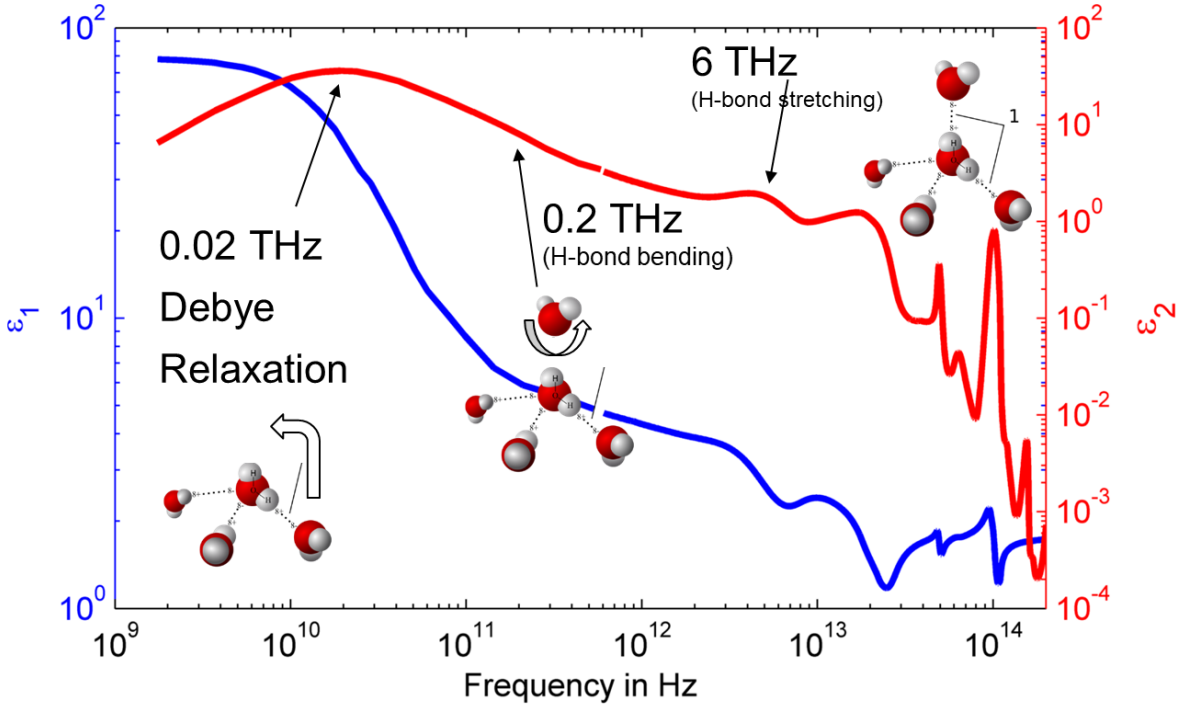

Fig. 4.4 Dielectric function of Water, THz directly excites H-bond dynamics. Adapted from [39, 42]

tendency of molecules to attract each other strongly through hydrogen bonds [38], i.e., from intermolecular forces. These forces and torques are determined by the permanent and induced molecular dipole moments. Therefore, the polarizability of water molecules is a crucial parameter, influencing its anomalous properties [44].

Despite the fundamental importance of these dipole moments, even the experimental uncertainty in the magnitude of the permanent dipole moment is significant, as experimental results spread between 2.6 and 2.9 D [45–47]. Till now, due to the lack of intense THz sources, no terahertz induced Kerr effect or molecular orientation in water was observed, since the weak Kerr signals were strongly absorbed by water(the propagation length is less than 100μm).

In the present work, we show that single-cycle terahertz (THz) pulses induce orientation of the water molecules, which subsequently relaxes. We use the THz-induced Kerr effect to characterize the polarizability of water molecules in the bulk liquid state. In the THz frequency regime, the dielectric function of water is dominated by three distinct relaxation mechanisms and a vibrational mode, which can be characterized by linear infrared spectroscopy [39]. The relaxation time constants τ were found to be 8.31, 1.0, and 0.10 ps. For later reference, we also give the corresponding frequencies $f = 2\pi\tau^{-1} = 0.019$, 0.20 and 2.0 THz, respectively. These relaxation processes are thought to originate from the dynamics of the hydrogen bond network, namely, the hopping of molecules to unoccupied sites in the tetrahedral structure,

the orientation time of a single molecule and the vibrational relaxation of hydrogen bonds, respectively [39].

For reference purposes, we also study two liquids without permanent dipole moments, carbon disulfide (CS_2) and benzene (C_6H_6).

The Kerr coefficient B of a molecular liquid, defined in equation (4.1), contains information about its permanent dipole moment μ, polarizability α and hyperpolarizabilities [48]. Phenomenologically, it can be described by the birefringence $\Delta n = n_{\parallel} - n_{\perp}$ caused by a strong electric field E with $\Delta n = \lambda B E^2$, where λ is the wavelength of the optical pulse used to probe it. Commonly, the strong electric field causing the birefringence is either static or at optical frequencies.

In case of water, static fields causing a noticeable birefringence in the optical regime also dissipate significant amounts of heat, which restricts these measurements to relatively low field strengths (<50 kV/cm [49] and <30 kV/cm [50]) as compared to the saturation field strength of ∼10 MV/cm [32].It was found that $B_{stat} = 2.92 \times 10^{-14}$m/V^{-2} at 25°C. Later, also optical pulses with tens of nanoseconds duration were employed to measure the Kerr effect. A Kerr coefficient of pure liquid water of $B_{stat} = 0.053 \times 10^{-14}$m/V^{-2} was obtained [51], using the reference value for benzene [52]. Optical pulses of 18 fs duration were also employed to induce birefringence in liquid water [53]. The resulting optical Kerr effect (OKE) signal can be time-resolved using a pump-probe technique. It was shown that the resulting transient modulation of the birefringence relaxes on timescales that correspond to intramolecular vibrational modes of water, so that no information on the hydrogen bond network could be derived. Terahertz excitation, therefore, offers novel scientific opportunities, because its frequency matches that of intermolecular processes and therefore directly excites the hydrogen bond network. At the same time, the short duration of single-cycle pulses of only a few picoseconds enables access to the high-field response of water without suffering from excessive Joule heating.

4.3 Experimental setup

Our experimental setup of the THz-pump optical-probe in liquids is schematically shown in Fig. 4.5. We use optical pulses from a Ti:Sapphire chirped-pulse amplifier(Legend Elite Duo, and cryogenic amplifier from Coherent) with a fundamental wavelength of 800 nm, 150 fs pulse duration and 7 mJ pulse energy to generate THz pulses by pulse-front-tilted optical rectification in $LiNbO_3$, cooled to 150 K to enhance the conversion efficiency[54]. The optical pulse fronts is tilted by a gold-coated blazed grating(the incident angle is 61.0°, and the diffraction angle is 46.5°) with a groove density of 2000 lines/mm. The reflected pulses go through a half-wave plate and are then focused onto a stoichiometric $LiNbO_3$ crystal. The $LiNbO_3$ crystal is doped

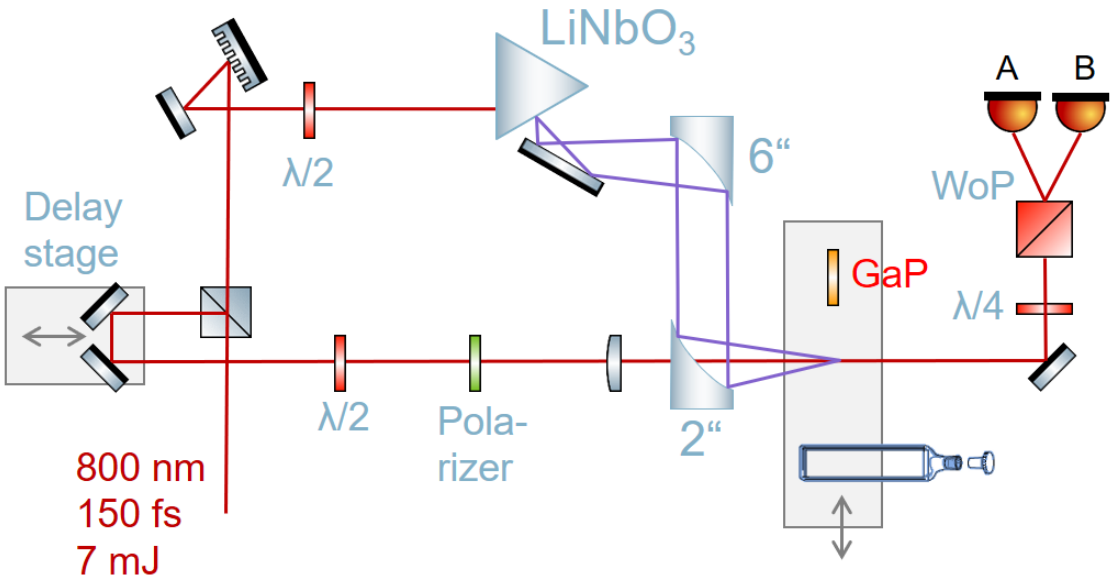

Fig. 4.5 Schematic of the experimental setup: The optical beam (red line) is split into a probe (weak) beam and pump (strong) beam, which are used to measure the optical birefringence with balanced photodiodes A and B sensitive to the probe intensity polarized parallel to the electric field of the THz pulse and perpendicular to it. The pump beam is used to generate THz pulses from $LiNbO_3$.

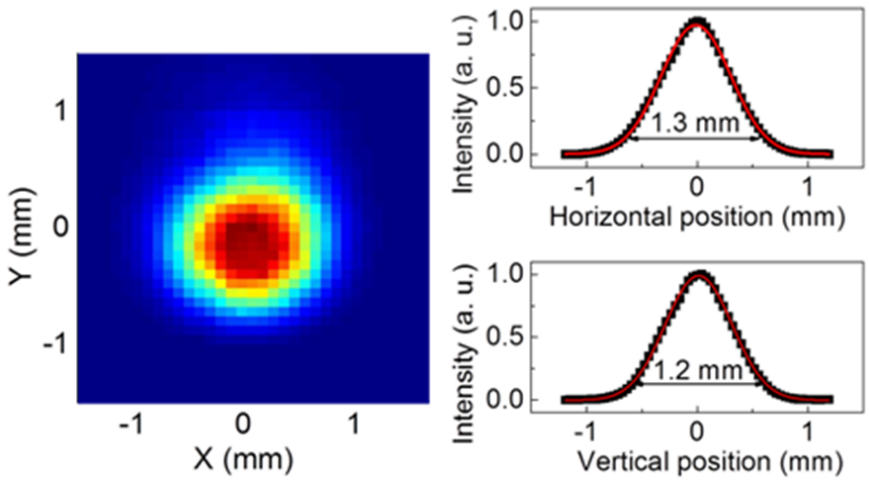

Fig. 4.6 The measured beam profile of THz focal spot, with a 1.3 mm diameter focal spot

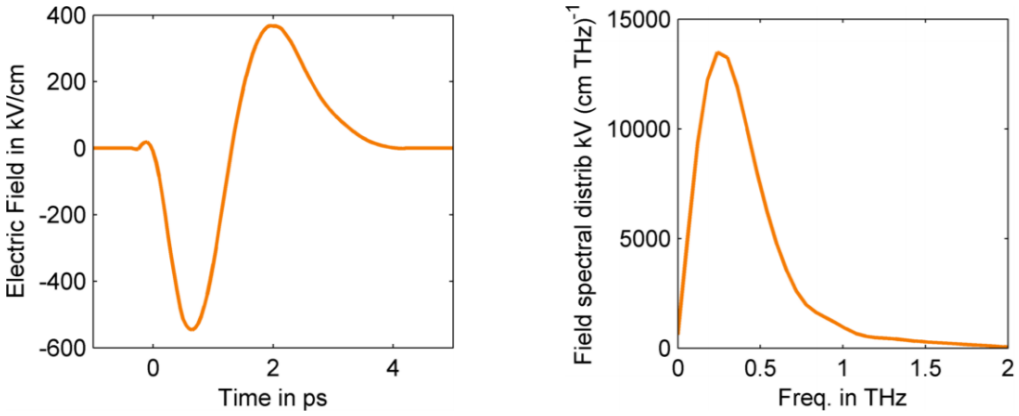

Fig. 4.7 THz pump pulse parameters in time domain and frequency domain,Peak field: ∼500 kV/cm; Pump frequency: 0.31 THz

with MgO at 5.0%, and z-cut into a right triangle with an apex angle of 56.0°. Both, the incident face for the exiting beam and the output face for terahertz wave was coated anti-reflective for 800 nm wavelength. We exploit a calibrated fast pyroelectric detector (Microtech Instruments) to measure the output THz energy and a pyroelectric camera (Spiricon Pyrocam IV) covered by a 2-mm-thick silicon wafer to measure the THz beam profile.

The THz pulses generated from this source are then de-magnified and re-focused using two off-axis parabolic mirrors with 4" and 2" focal lengths. In the focus, they are characterized by electro-optic (EO) sampling using a 50-μm-thick <110>-cut GaP and a 200-μm-thick <110>-cut ZnTe crystal. The electric field waveform consists of a single cycle with peak electric field strength of 510 kV/cm and 0.31-THz center frequency (see Fig. 4.7). The THz beam diameter in the focus is around one millimeter (See Fig. 4.6) and an order of magnitude larger than the optical probe spot.

For the measurement of liquid samples, Spectrosil® (synthetic fused silica) cuvettes are used with 1 cm diameter aperture, 1.2-mm-thick windows enclosing a 0.2-mm-thick sheet of liquid. Only for carbon disulfide, due to its low THz absorption, a cuvette of 2-mm-inner thickness was used. To measure the optical birefringence, the polarization of the probe beam is tilted by 45° with respect to the THz electric field polarization. A Kerr effect time trace is recorded by scanning the delay between the pump (500 Hz repetition rate) and the probe (1 kHz), reading the pump-induced modulation detected by the balanced photodiodes using a Lock-In amplifier.

Due to the group-velocity mismatch between the optical and THz pulses in some liquids, it is important to consider the dielectric function in the THz regime for each liquid. Therefore, we measured the complex dielectric functions of all liquids in the same geometry, using a

dedicated commercial setup for THz time-domain spectroscopy (TDS). The resulting data are shown in Fig. 4.19 and Fig. 4.20.

All liquids except neat water were obtained commercially with >99.9% purity for methanol and 2-propanol, >99.8% purity for ethanol, benzene and D_2O and >99% for CS_2. Ultra-pure water was obtained from a lab-based purification system, specified to $< 0.1\mu S/cm$ at 20°C. During all measurements, the liquid was held at a constant temperature of 296 ± 1 K.

4.4 THz-induced birefringence in liquids

4.4.1 Field dependence

To understand the field dependence of the liquids, we firstly measured the Kerr effect in CS_2 as a reference. By scaling the pump energy, the Kerr signal under different pump energy was observed (shown in Fig. 4.8). The maximum of the Kerr signal scaled linearly with the pump energy (shown in Fig. 4.9). A detailed analysis will be shown in next section.

Similarly, we test the polar liquid trans-anetholes sample. In Fig. 4.10, the unipolar shape of the signal corresponds to the squared electric field waveform of the THz pulse, providing evidence for the observation of an intensity-driven effect. This implies that we indeed observe a Kerr effect, where the optical modulation is due to a partial orientation of the anethole molecules along the electric field. The relaxation of this molecular orientation can be followed after THz excitation at delays between 2 and 5 ps with a time constant of (3.5 ± 0.4)ps. Fig. 4.10 (c) shows the square root of the peak rotation angle as a function of the peak field strength inside the anethole. The linear scaling confirms that this effect scales with the THz intensity. Based on the slope of this curve we can determine the Kerr coefficient for the THz-induced optical anisotropy. The highest field strength obtained inside anethole is 310 kV/cm after accounting for reflection losses at the air-silica (n = 2.1[55]) and silica-anethole (n= 1.62) interface. Based on the evidenced rotation of the probe beam polarization, $\Delta\varphi = 1.5$ mrad, we calculate the change in refractive index $\Delta n = \Delta\varphi \times \lambda\,(2\pi d_{\text{eff}})^{-1}$, where d_{eff} is the effective interaction length, limited by the walk-off of THz and optical (n = 1.561 [56]) beams. With $d_{\text{eff}} = 500\mu$m it follows that $\Delta n = 3.8 \times 10^{-7}$, so that the THz Kerr coefficient B$= (5 \pm 1) \times 10^{-16}$m/V^2, which is two orders of magnitude smaller than the optical Kerr coefficient of anethole, B$= 7 \times 10^{-14}$m/V^2 [52]. Since this value was measured with pump and probe wavelengths of 694 nm and 488 nm, respectively, the Kerr coefficient at 800 nm probe wavelength might differ. We have verified, by measuring the empty silica cuvettes, that the Kerr effect originates from the liquid inside the cell and not from the window material. Each window absorbs $< 2\%$ of the THz intensity and 2

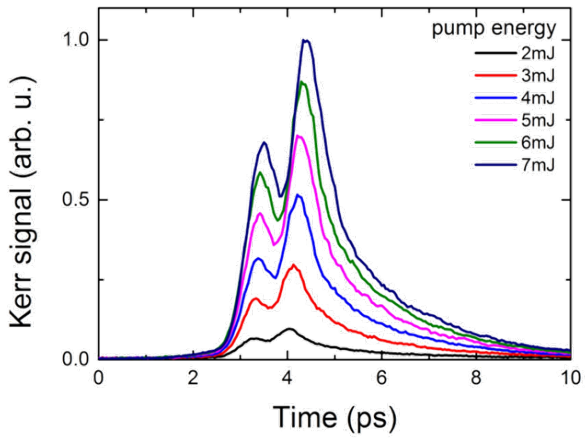

Fig. 4.8 The field dependant birefringence in CS_2.

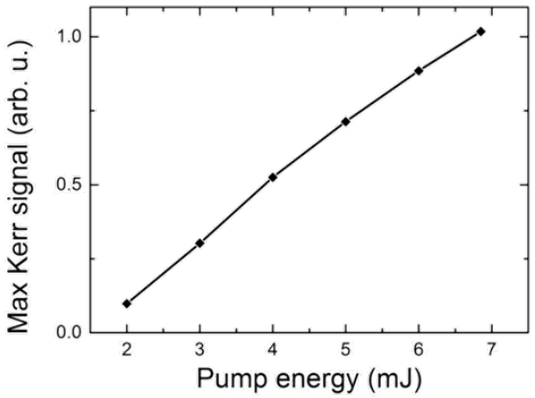

Fig. 4.9 The pump energy dependance in CS_2.

mm of anethole absorbs $(70 \pm 7)\%$, so that the effective interaction length is not significantly reduced by absorption.

Fig. 4.11 shows the EO sampling curves as function of the pump energy on the $LiNbO_3$ crystal. From these curves we derive the field strength reached at each pump fluence. Fig. 4.11(b)-(d) shows Kerr effect measurements on the empty cuvette, methanol and water for different fluences of 7.4 mJ, 5 mJ and 3 mJ. The numbers in the data mark the time delay at which the values were extracted to determine the fluence dependence. Fig. 4.11(e) shows the induced birefringence as a function of the electric field in the THz pulse together with a linear and a quadratic fit. The relation $\Delta\Phi \propto E^2$ is clearly observed with a slight tendency toward a higher exponent, which is probably caused by a non-linear scaling of the EO sampling crystal.

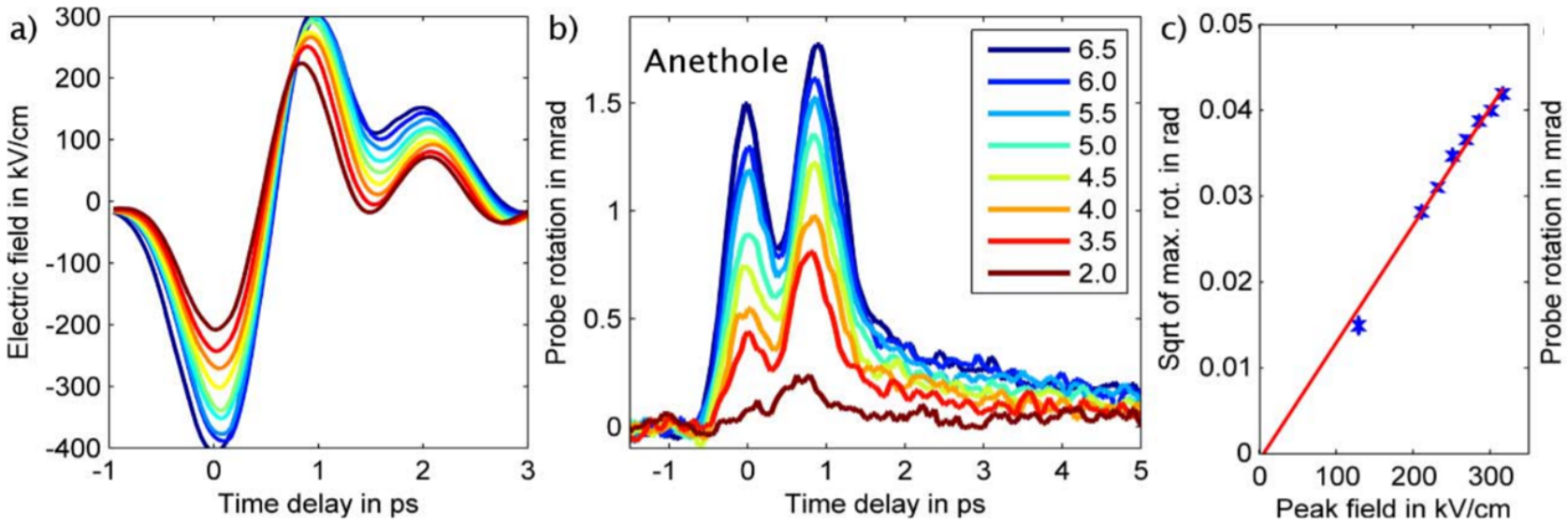

Fig. 4.10 (a) Electro-optic sampling trace of the incoming THz pulses. At a delay of 2 ps, a backreflected THz pulse again modulates the 50 μm thick GaP. The color code and the values in the legend denote the 800 nm pump energy in mJ consistently for all panels. The scaling shows a constant conversion efficiency in this regime of the cryogenically cooled $LiNbO_3$ crystal. (b) THz-induced optical anisotropy in anethole: The electric field of the THz pulse induces an instantaneous modulation of the optical properties and an additional long-lived modulation occurs due to the relaxation of molecular orientation. (c) The magnitude of the optical modulation scales linearly with the THz intensity, thereby confirming the Kerr-like nature of the observation.

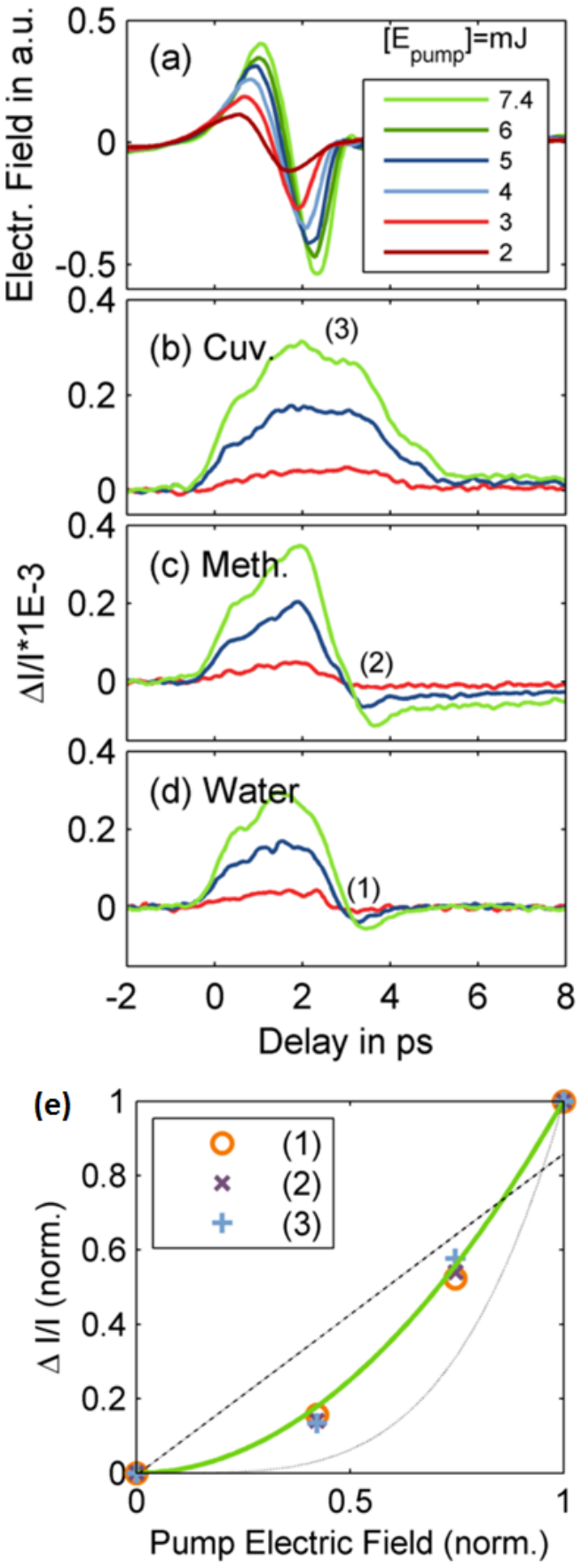

Fig. 4.11 Field dependant birefringence in methanol and water [57]: (a) shows the EO sampling curves as function of the pump energy on the $LiNbO_3$ crystal. From these curves we derive the field strength reached at each pump fluence. (b)-(d) shows Kerr effect measurements on the empty cuvette, methanol and water for different fluences of 7.4 mJ, 5 mJ and 3 mJ. The numbers in the data mark the time delay at which the values were extracted to determine the fluence dependence. (e) shows the induced birefringence as function of the electric field in the THz pulse together with a linear and a quadratic fit. The relation $\Delta\Phi \propto E^2$ is clearly observed with a slight tendency toward a higher exponent, which is probably caused by a non-linear scaling of the EO sampling crystal.

4.5 Study of molecular polarizability anisotropy of liquid water

4.5.1 Model for THz-induced Kerr effect

In our experiment, the Kerr effect is induced by single-cycle electromagnetic THz pulses $E(t)$. The resulting birefringence is probed by the phase shift $\Delta\Phi(t)$ of a co-propagating optical pulse of 150 fs duration and wavelength $\lambda = 800$ nm with linear polarization tilted 45° with respect to the polarization of the THz field. The measured phase shift $\Delta\Phi(t)$ is caused by the birefringence $\Delta n(z,t)$ at position z along the direction of propagation, via

$$\Delta\Phi(t) = \frac{2\pi}{\lambda} \times \int_0^L \Delta n(z,t) dz \tag{4.3}$$

where L denotes the thickness of the sample. Furthermore, Δn can be decomposed into two contributions - a temperature-independent electronic effect,

$$\Delta n_e(z,t) = \lambda B_e E^2(z,t), \tag{4.4}$$

which follows the square of the instantaneous THz electric field and a molecular mechanism. The latter is temperature-dependent and can be modeled from a Langevin dynamics model [58], which is derived in Appendix on the basis of Brownian motion of a molecule in the overdamped and dilute limit (equation (A.17)) under the assumption of an isotropic rotational diffusion tensor [36],

$$\begin{aligned} \Delta n_{\mathrm{m}}(z,t) = & \frac{2\pi B_{\mathrm{m}}^{(1)}}{\tau_2} \beta \int_{-\infty}^{t} \mathrm{d}t' E^2(z,t') \times \exp\left(-\frac{t-t_1}{\tau_2}\right) \\ & + \frac{2\pi B_{\mathrm{m}}^{(2)}}{\tau_1 \tau_2} \beta^2 \int_{-\infty}^{t} \mathrm{d}t'' \, E(z,t'') \\ & \times \exp\left(-\frac{t-t''}{\tau_2}\right) \\ & \times \int_{-\infty}^{t''} \mathrm{d}t' E(z,t') \times \exp\left(-\frac{t'-t''}{\tau_1}\right) \end{aligned} \tag{4.5}$$

Here $\beta = (k_{\mathrm{B}}T)^{-1}$ and the birefringence at time t is influenced by the THz electric field at all earlier times $t', t'' < t$. The relaxation times are related to the Debye relaxation time via $\tau_1 = \tau_{\mathrm{D}}$ and $\tau_2 = \tau_{\mathrm{D}}/3$. The two terms scaled by $B_m^{(1)}$ and $B_m^{(2)}$ correspond to polarization-induced alignment and dipole moment-induced orientation. The coefficient $B_{\mathrm{m}}^{(1)} = c_1 \left(\Delta\alpha \times \Delta\varepsilon + \frac{3}{4} \times \Delta\alpha^+ \times \Delta\varepsilon^+\right)$, where $c_1 > 0$, α is the optical polarizability tensor at the probe frequency and ε is the dielectric tensor at the THz pump frequency. $\Delta\alpha = \alpha_{zz} - 0.5 \times (\alpha_{xx} + \alpha_{yy})$ and $\Delta\alpha^+ = \alpha_{xx} - \alpha_{yy}$, where z is defined as the axis of the permanent dipole moment; or in the absence of a dipole moment

as the axis of rotational symmetry. As $\Delta\mathscr{E}$ is defined similarly and both tensors are expected to share no different shape between the THz and optical regime, $B_m^{(1)}$ would scale with $\Delta\alpha^2$ and results in a positive sign. This term describes the alignment of molecules along their highest polarizability. The coefficient $B_{\mathrm{m}}^{(2)} = c_2\Delta\alpha\mu^2$, where $c_2 > 0$ and μ is the permanent dipole moment of the molecule. This term describes an orientation by the permanent dipole moment. It enables the determination of the sign of $\Delta\alpha$ based on the sign of Δn_{m} alone. This is because the temporal average of the term scaling with $B_m^{(2)}$ in equation (4.5.1) would follow the sign of $B_m^{(2)}$ and dominates over the one with $B_m^{(1)}$ in case of all polar liquids discussed here [41, 59]. Therefore, for polar molecules$\Delta n_m \propto \Delta\alpha$.

4.5.2 Experimental results

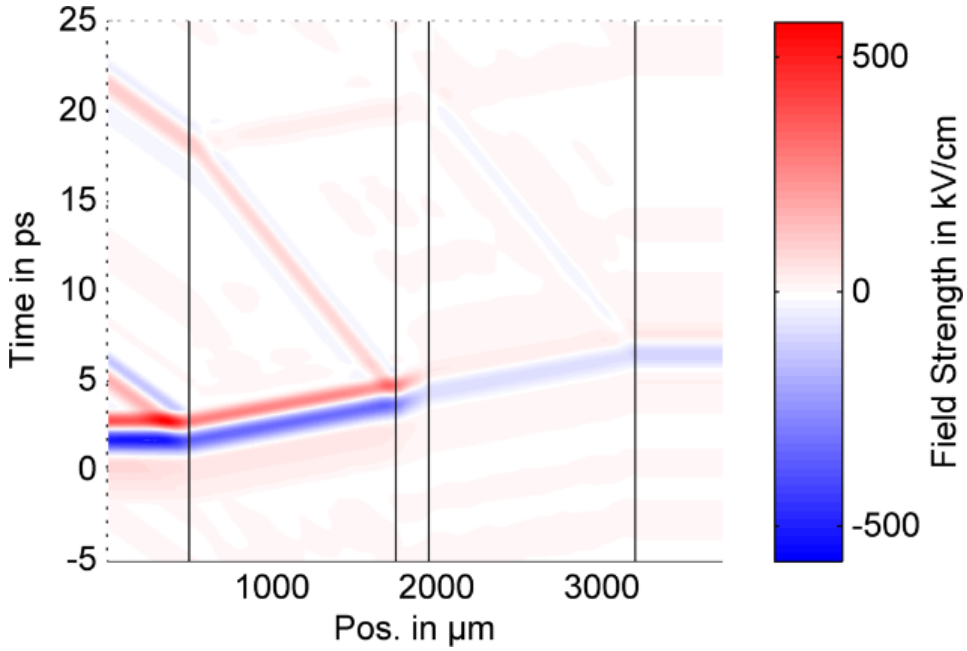

Fig. 4.12 Propagation of the single cycle THz pulse through a cuvette filled with water [57]. The vertical lines indicate the interfaces between the two 1.2 mm thick fused silica windows and the 0.2 mm thick sheet of water. The THz pulse propagates from left to right. Color code corresponds to electric field strength in kV/cm.

The Kerr effect traces of carbon disulfide and benzene are shown in Fig. 4.16, with the phase shift caused by the optical birefringence Δn ,

$$\Delta\Phi(t) = \frac{2\pi}{\lambda} \times \int_0^L \Delta n(z,t)dz \tag{4.6}$$

plotted on the vertical axis. L is the thickness of the material along the propagation direction z of both beams. The integral runs over the thickness of the material under investigation. Both liquids were included in this study for reference with earlier THz and optical measurements [33, 52] and because their Kerr coefficients are large, while at the same time they are transparent in the THz regime (see Tab 4.1).

The raw data of carbon disulfide (L=2 mm) can be decomposed into two contributions, $\Delta n_e(z,t) = \lambda B_e E^2(z,t)$ (orange curve), which follows the instantaneous electric field of the THz pulse and

$$\Delta n_m(z,t) = \frac{2\pi B_m}{\tau} \int_{-\infty}^{t} dt' E^2(z,t') \times \exp\left(\frac{t'-t}{\tau}\right) \tag{4.7}$$

(green curve), which at time t is influenced by the electric field at time $t' < t$. The electric field $E(t)$ is obtained directly and in absolute units from EO sampling. This phenomenological model can be matched with great accuracy to the experimental data by refining the three parameters B_e, B_m and τ, whose resulting values are summarized in Tab 4.1.

The accuracy of the model implies that the experiment can be described by an instantaneous birefringence and an excitation-relaxation mechanism, which is dominated by the timescale of a single microscopic process. The Kerr coefficient of carbon disulfide obtained in this work, B=B_e+ $B_m = 0.50 \times 10^{-14}$m/V^2 is almost an order of magnitude smaller than the one reported previously (B= 2.4×10^{-14}m/V^2 [33].The decay time constant τ =1.84 ps, which is in good agreement with earlier THz-based work (1.7 ps [33]) and the calculated collective molecular orientation time 1.64 ps [35]. This indicates that the origin of the mechanism connected to B_m is the relaxation of molecular orientation induced by the electric field of the THz pulse. In previous Fig. 4.11, we provide experimental results for the fluence dependence of the data, confirming that this effect is indeed a Kerr effect with $\Delta\Phi \propto E^2$.

The quartz windows of the used cuvettes also induce a birefringence, which is depicted in Fig. 4.13(f) and is found to be negligible as compared to the signal from carbon disulfide.

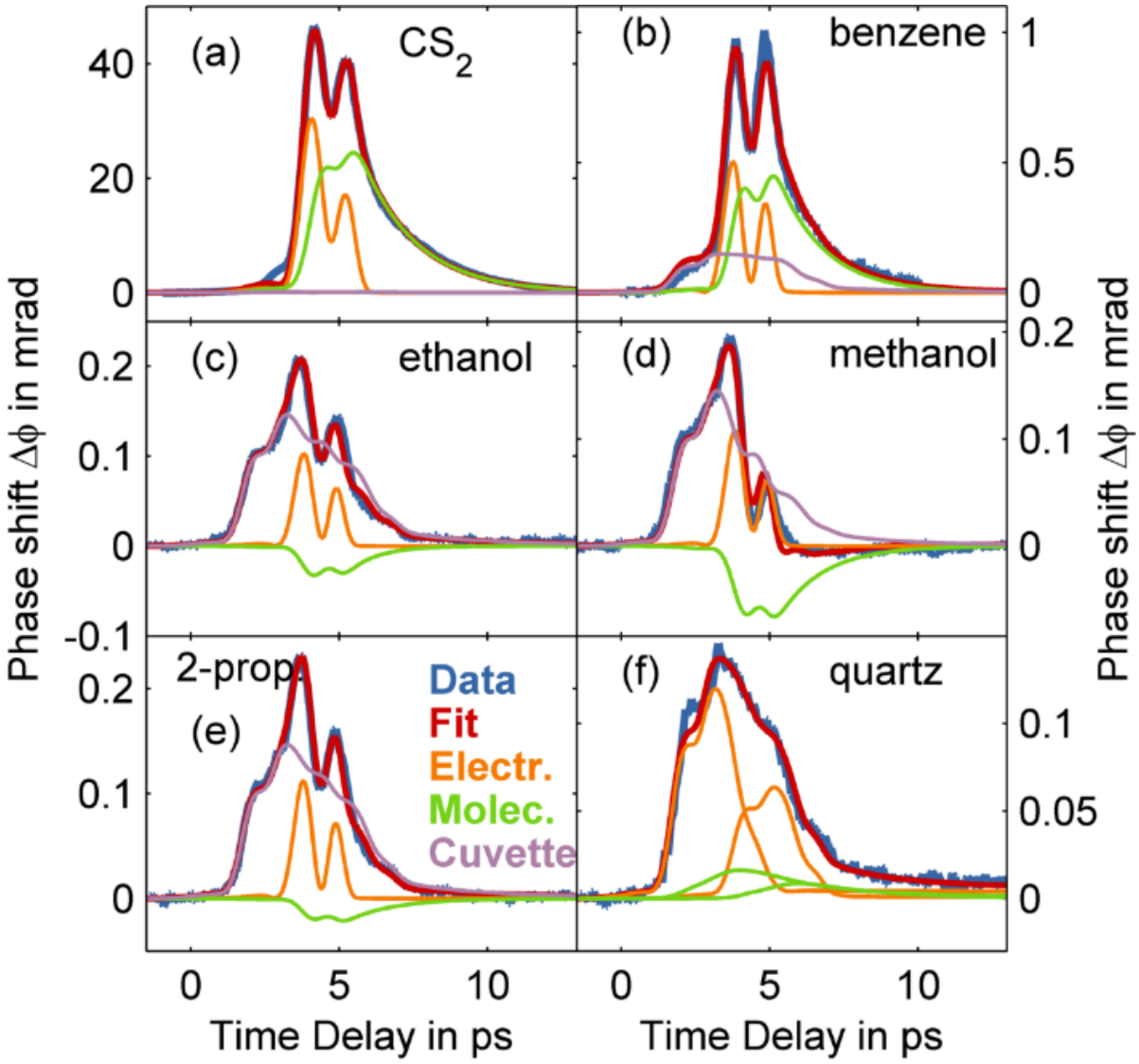

Fig. 4.13 The THz-induced Kerr effect in water and reference liquids [57]. The raw Kerr traces induced by THz without subtracting the background from the cuvette. THz-induced Kerr effect, as evidenced by the phase shift of the transmitted probe beam. The refinement (red curve) is the sum of two contributions: An instantaneous electronic birefringence (orange curve) and a delayed, molecular birefringence (green curve). While in the non-polar molecules CS_2 and benzene (a,b), a positive molecular alignment effect is observed together with a positive electronic response, the polar molecules (ethanol, methanol and 2-propanol) shown in (c-e) reveal a negative molecular orientation effect.

Table 4.1 Summary of literature and experimental parameters relevant to this study. All values without literature reference are the result of this work. B_{opt} is the Kerr coefficient derived from OKE experiments.

	n (λ=800nm)	n (λ=800 μm) (0.37 THz)	α(λ=800 μm) in cm^{-1}	B_{opt} in 10^{-14} m/V^2 ($\lambda_{pump}/\lambda_{probe}$)	B_{stat} in 10^{-14} m/V^2	B_e in 10^{-14} m/V^2	$B_m^{(1)}$ in 10^{-14} m/V^2	$B_m^{(2)}$ in 10^{-14} m/V^2	B_m/B_e	τ_2 in ps
CS_2	1.6058 [60]	1.7	<0.5	4.1(694/488) [52]	3.244	0.28	0.22	-	0.77	1.84
2-propanol	1.379 [61]	1.54	22	0.052(1064/442) [52]	3.142	0.0097	-	-0.0033	-0.34	1.52
ethanol	1.3573 [60]	1.6	22	0.051 (1064/442) [52]	0.4442	0.0093	-	-0.0067	-0.72	0.96
methanol	1.323 [61]	1.8	64	0.034 (1064/442) [52]	2.1742	0.016	-	-0.018	-1.14	1.46
H_2O	1.3282 [60]	2.48	143	0.035 (694/488) [52]	2.9243	< 0.003	-	-0.025	< -8.3	1.1
H_2O+1M NaI	1.347 [62]	2.51	160			< 0.003	-	-0.027	< -9.1	1.1
H_2O+3M NaI	1.388 [62]	2.63	166			< 0.003	-	-0.043	< -14.3	1.1
H_2O+5M NaI	1.420 [62]	2.76	165			< 0.003	-	-0.071	< -23.8	1.0
H_2O+9.5M	1.475 [62]	2.91	157			< 0.003	-	-0.102	< -33.9	1.0
D_2O	1.324 [63]	2.34	130	0.029 (1064/442) [52]		< 0.003	-	-0.021	< -6.9	1.36
fused silica	1.453 [64]	1.95	1.5	0.018 (1064/1064) [65]		0.0033	0.0004	-	0.13	2.38
benzene	1.489 [66]	1.51 (1.51 [67])	∼1 (1.42 [67])	0.70 (694/488) [52]	0.39 [68]	0.035	0.029	-	0.84	1.55

The same phenomenological model is applied to refine the data on quartz and can be used in the following to subtract the Kerr effect caused by the cuvette. This is demonstrated for benzene in Fig. 4.16(b), where the signal from the cuvette (purple curve) is subtracted before applying the same model. Again, the phenomenological model accurately reproduces the experimental data and we conclude that all information from the experimental data can be expressed by three parameters, B_e, B_m and τ. The resulting ratio of the Kerr coefficients B_e for carbon disulfide and benzene is 8.0, which is in good agreement with an earlier THz-based result of 9.2 [33], where the absorption of benzene was not considered and therefore a larger value was obtained.

Fig. 4.13(c)-(e) show the Kerr effect traces of three different alcohols. Again, the phenomenological model reproduces the experimental data of all liquids, but it turns out that the sign of the molecular component B_m is negative for all alcohols investigated. Also, the ratio B_m/B_e scales with the size of the molecules. Its magnitude decreases continuously with increasing mass and size: -1.14 for methanol (CH_4 O), -0.72 for ethanol (C_2 H_6O) and -0.34 for 2-propanol (C_3 H_8O). It is worth mentioning that their permanent dipole moments are almost equal (methanol 1.70 D, ethanol 1.69 D, 2-propanol 1.56 D [69]).

Finally, the Kerr effect traces for liquid water are shown in Fig. 4.14(a). Given the low Kerr coefficient of water, known from earlier experiments [51], it is not surprising to see that the signal from the cuvette is of a similar order of magnitude as the effect of water. Due to the high absorption in the THz regime, the signal cannot be increased by using a thicker cuvette. Given the experimental uncertainties, we can only give an upper limit of 0.003×10^{-14}m/V^2 for B_e, which corresponds to the value of B_e at which the residual discrepancy between data and model doubles. In contrast to the alcohols, $B_m^{(2)} = -0.025 \times 10^{-14}$m/V^2 is of significantly larger magnitude than B_e and one can wonder what causes this mechanism. Comparing the relaxation time constant τ of 1.1 ps with those of the known relaxation mechanisms, one finds good agreement with the orientation relaxation time of single water molecules of 1.0 ps [39]. This shows that the electric field of the THz pulse partly orients the water molecules.

4.5.3 Kerr effect in aqueous solutions

We also prepared aqueous solutions of NaI, producing solutions with 1, 3, 5 and 9.5M. The resulting data in Figs. 4.14 (b) and Figs. 4.14 (c) reveal that the Kerr effect remains qualitatively unchanged with the same parameters B_e and τ. The magnitude of the molecular orientation mechanism B_m, however, increases proportional to the concentration of NaI up to $B_m = -0.10 \times 10^{-14}$m/V^2 at 9.5M. A full overview of Kerr signals in solutions of various salts with different concentrations are shown in Fig. 4.15. Similarly, the magnitude of the molecular orientation mechanism B_m also qualitatively increases proportional to the concentration of all the other salts.

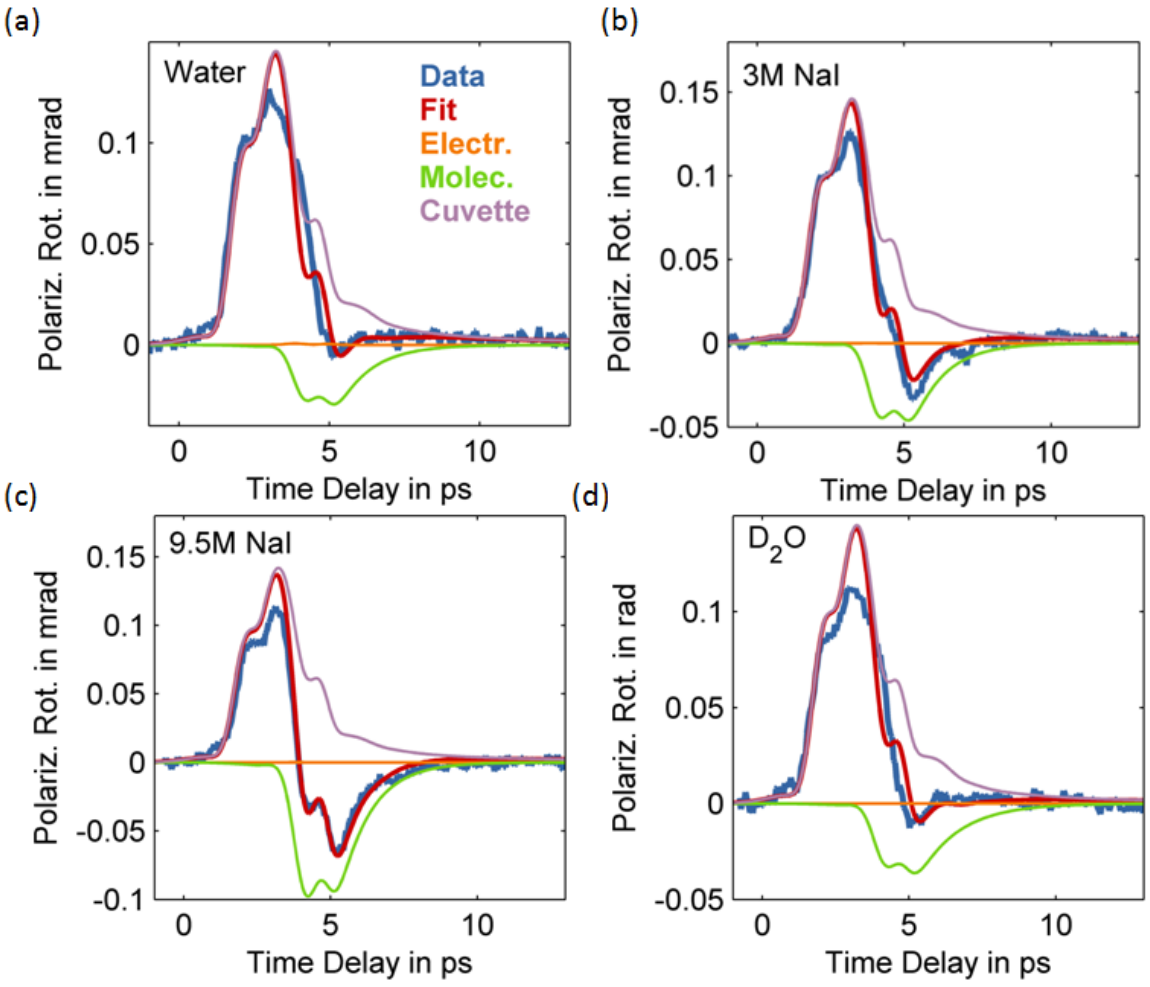

Fig. 4.14 The raw Kerr traces (blue curves) in (a) water, (b) water with 3 M NaI, (c) water with 9.5 M NaI, (d) heavy water (D_2O), which shown before subtracting the background from the cuvette (purple curves) based on the known Kerr coefficient obtained from the refinement of an empty cuvette.

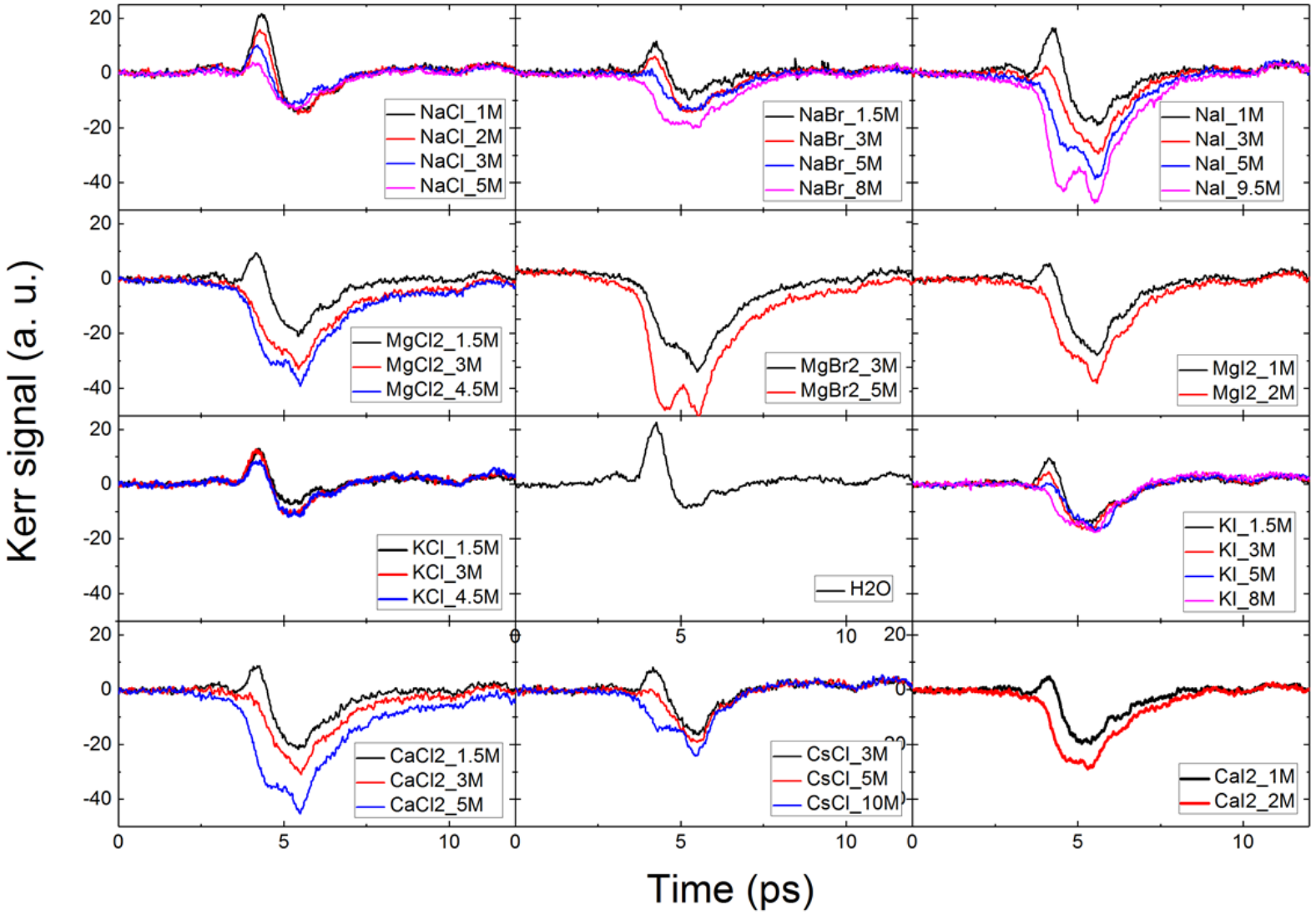

Fig. 4.15 An overview of Kerr signals in solutions of various salts with different concentrations.

Finally, we have studied heavy water in the same geometry and find that the only parameter that significantly changes with respect to hydrogen-based water is the relaxation time τ, which increases to 1.36 ps - consistent with an increase of the molecular mass and inertia and in good agreement with the 29% increase in relaxation time [70].

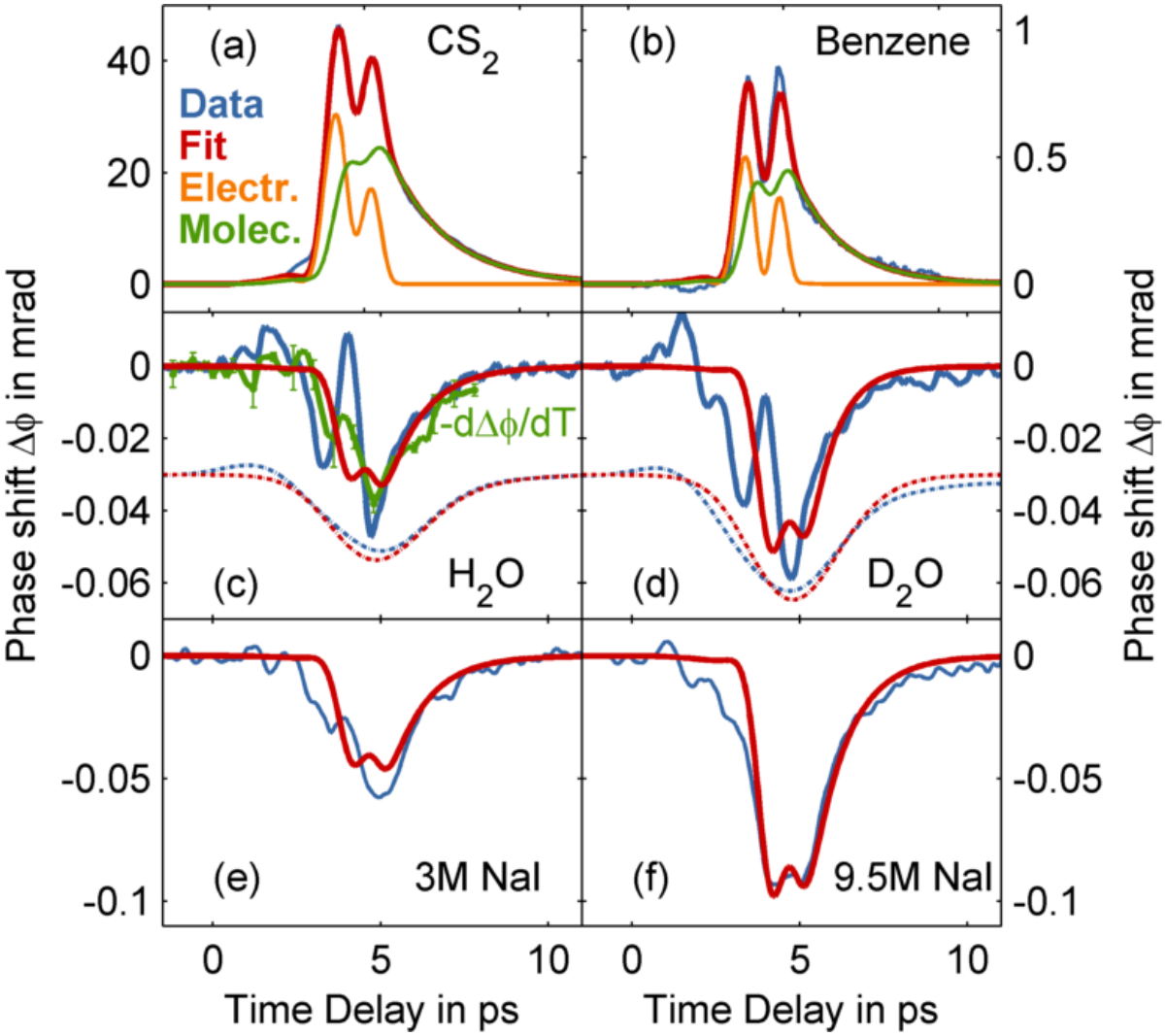

Fig. 4.16 THz-induced Kerr effect, as evidenced by the phase shift of the transmitted probe beam. The refinement (red curve) is the sum of two contributions: An instantaneous electronic birefringence (orange curve) and a delayed, molecular birefringence (green curve). While in the non-polar molecules CS_2 and benzene(a,b), a positive molecular alignment effect is observed together with a positive electronic response, the polar water molecules (c-f) reveal a negative molecular orientation effect. The electronic Kerr effect background of the cuvette was subtracted. We also isolate the molecular orientation mechanism of water based on its temperature dependence $-d\Delta\Phi(t)/dT$ (green curve) in a background-free measurement. In (c,d), additional dotted curves, offset by -0.03 mrad, correspond to a convolution with a Gaussian $\sigma = 1.4$ ps.

4.5.4 Temperature-dependence of the TKE in water

To further support the decoupling of the Kerr effect of water into an electronic and a negative molecular contribution, the measurement was repeated at various temperatures T between 23 and 68°C. The resulting temperature-dependent signal, $-d\Delta\Phi(t)/dT \propto \Delta\Phi_m$ (green curve) scales with the molecular contribution to the Kerr effect alone. This implies that any influence from the electronic effects inside the cuvette and from water are not relevant. Indeed, the Kerr signal of an empty cuvette is found confirmed to be temperature-independent (see Fig 4.17). On the other hand, the resulting temperature-dependence for a cuvette filled with water is in good agreement with the earlier decoupling by refining eq. 4.6 and eq. 4.7 based on the known electric field $E(z,t)$. We conclude that the residual signal, not observed in the temperature dependence, originates from electronic effects in water and in the cuvette. Therefore, the average TKE in water is found to be negative, as can also be seen from the dashed curves, which are obtained after convolution with a Gaussian of width σ=1.4 ps and correspond to the results expected when performing the experiment with longer probe pulses, not resolving the fast dynamics.

4.6 Time domain spectroscopy

4.6.1 Principle of THz time-domain spectroscopy

The THz time-domain spectroscopy (TDS) utilizes a broadband terahertz pulses that propagate through a sample. The electric field of the transmitted pulse $E_{sample(t)}$ is measured as a function of time. Then a reference waveform $E_{ref.(t)}$ without the sample in the beam path is additionally measured to gain quantitative information about the linear optical properties of the sample. The refractive index $n(\omega)$ and the absorption coefficient $\alpha(\omega)$ can be extracted from analysing the ratio of the Fourier transforms of the terahertz transients $E_{\text{sample}}(\omega)/E_{\text{ref.}}(\omega)$.

For the analysis, define $r(\omega) = \left|E_{\text{sample}}(\omega)\right| / \left|E_{\text{ref.}}(\omega)\right|$ and the phase difference $\phi(\omega) = \phi_{\text{sample}}(\omega) - \phi_{\text{ref.}}(\omega)$:

$$E_{\text{sample}}(\omega) = \left|E_{\text{sample}}(\omega)\right| \exp\left[i\phi_{\text{sample}}(\omega)\right] \tag{4.8}$$

$$E_{\text{ref.}}(\omega) = \left|E_{\text{ref.}}(\omega)\right| \exp\left[i\phi_{\text{ref.}}(\omega)\right] \tag{4.9}$$

$$\frac{E_{\text{sample}}(\omega)}{E_{\text{ref.}}(\omega)} = r(\omega)\exp[i\phi(\omega)] \tag{4.10}$$

Taking into account the Fresnel transmission coefficients at the surfaces of the sample and the propagation and the attenuation of the pulse within the sample, the complex ratio of the

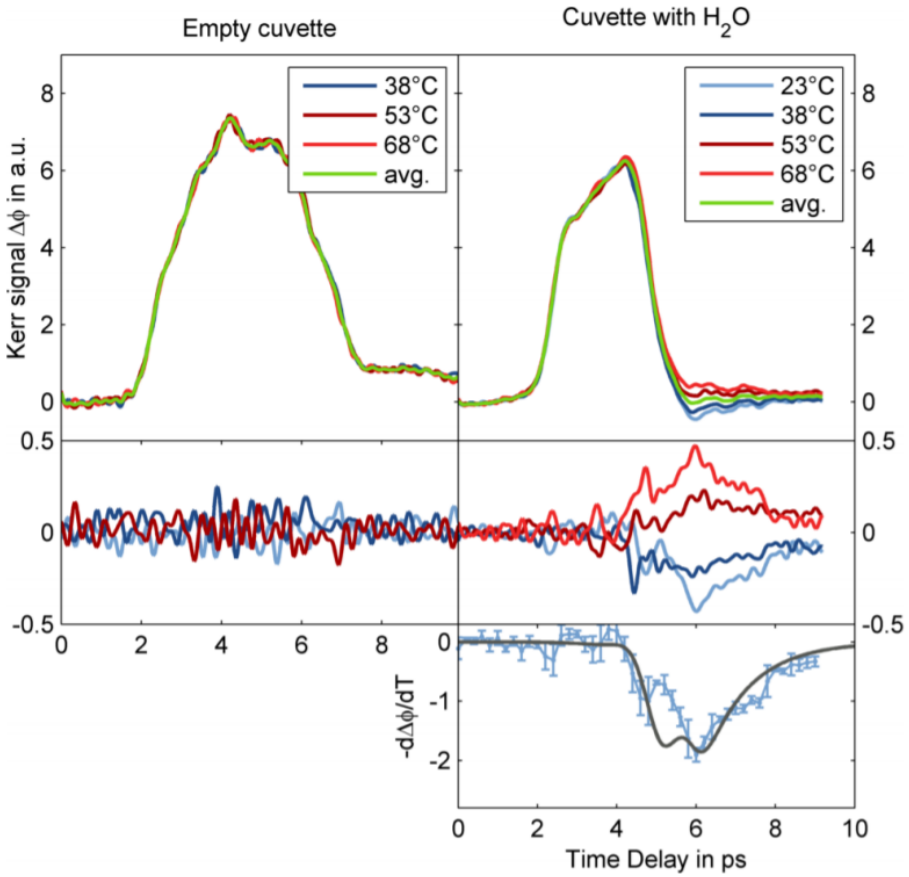

Fig. 4.17 Temperature dependence of the TKE from an empty cuvette (left panels) and from water inside the cuvette (right panels) with temperatures given in the legend [57]. The two middle panels show the difference of each curve and their average (green curve). While the purely electronic signal from the cuvette is temperature independent, the TKE from water shows a clear temperature dependence.

spectra can be written as:

$$\frac{E_{\text{sample}}(\omega)}{E_{\text{ref.}}(\omega)} == \frac{t_{12}\, e^{i\omega d n_2/c}\, \hat{t}_{23}\, e^{i\omega l \hat{n}_3/c}\, \hat{t}_{32}\, e^{i\omega d n_2/c}\, t_{21}}{t_{12}\, e^{i\omega d n_2/c}\, t_{21}\, e^{i\omega l n_1/c}\, t_{12}\, e^{i\omega d n_2/c}\, t_{21}} = \frac{\hat{t}_{23}\, \hat{t}_{32}}{t_{21}\, t_{12}} e^{\frac{i\omega l}{c}(\hat{n}_3 - n_1)} \tag{4.11}$$

where, t_{ij} is the Fresnel transmission coefficient for normal incidence, $\hat{t}_{ij} = 2\hat{n}_i/\left(\hat{n}_i + \hat{n}_j\right)$, $\hat{n}_3 = n_3 + i\kappa_3$ is the complex refractive index of the liquid sample, l is the thickness of the liquid chamber(shown in Fig. 4.18). The experiments are usually carried out in a dry air atmosphere whose complex refractive index $\hat{n}_{\text{air}}(\omega) = n_{\text{air}}(\omega) + i\kappa_{\text{air}}(\omega) \approx 1$. Let $\tilde{n}(\omega) = \hat{n}_3$ denote the complex refractive index of the sample, we obtain:

$$\frac{E_{\text{sample}}(\omega)}{E_{\text{ref.}}(\omega)} = \frac{4\tilde{n}(\omega)}{(1+\tilde{n}(\omega))^2} \exp\left[i\frac{\omega l(\tilde{n}(\omega)-1)}{c}\right] \tag{4.12}$$

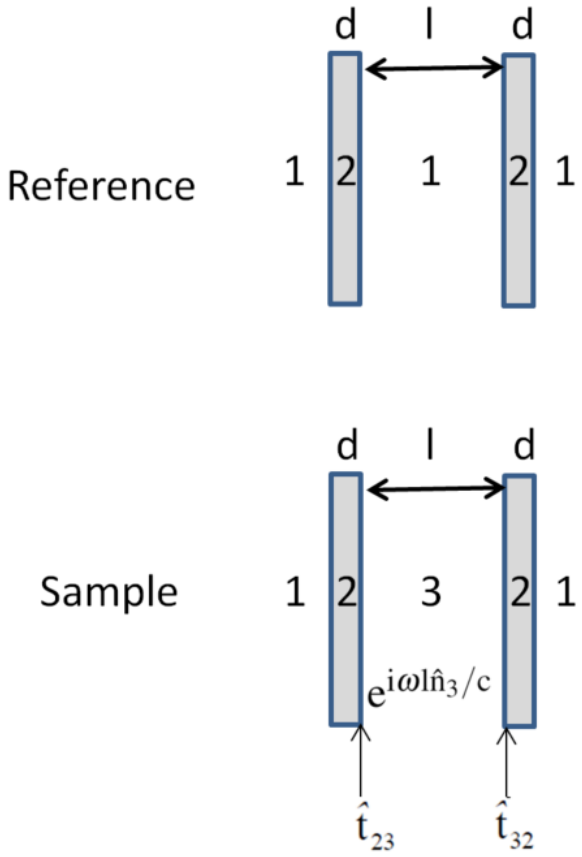

Fig. 4.18 Schematic representation of the sample cell. 1 air, 2 fused sillica, and 3 the liquid.

The power absorption coefficient $\alpha(\omega)$ is related to the imaginary part of the complex refractive index $\kappa(\omega)$ as follows: $\alpha(\omega) = \frac{2\omega}{c}\kappa(\omega)$. Substitute $\alpha(\omega)$ into $\tilde{n}(\omega) = n(\omega) + i\kappa(\omega)$ and combine equation(4.10) and equation (4.12), we obtain

$$n(\omega) = 1 + \frac{c\phi(\omega)}{\omega l} \tag{4.13}$$

$$\alpha(\omega) = -\frac{2}{l}\ln\left(\frac{(n(\omega)+1)^2}{4n(\omega)}r(\omega)\right) \tag{4.14}$$

With equation:(4.13 and equation:(4.14), we can easily deduce the complex refractive index of the sample from the TDS data.

4.6.2 Experimental Results

In the experiment, TDS was performed using a commercial fiber-laser and antenna based THz-generation system operating at MHz repetition rates. The TDS scans were performed

under nitrogen purging, and for every sample the empty cuvette was sealed and measured as reference. Two cuvettes of different thickness were used to adjust for the absorption in each liquid. Both cuvettes are made of two flat fused silica windows, each of thickness $d' = 1.2$mm. In the thick cuvette with $d = 2$mm path length, all backreflections can be removed by temporal windowing, but for the thinner 200 μm-thick cuvettes, a transfer function approach must to be employed, which considers the back reflections inside the sample volume,

$$\frac{E_{cuv}(\omega)}{E_{mty}(\omega)} = \frac{16N'^2 \times \exp((N'-1)\,2i\omega d'/c)}{\exp(2i\omega d/c) \times \left(1-N'^2\right)^2 - (N'+1)^4} \tag{4.15}$$

where $E_{mty}(\omega)$ and $E_{cuv}(\omega)$ are the complex-valued Fourier transformed TDS traces of the empty beam path and the empty cuvette, respectively. N' is the refractive index of the cuvette material (fused silica), which can be determined numerically for each frequency value in the data. Similarly,

$$\frac{E_{liq}(\omega)}{E_{cuv}(\omega)} = N\frac{\exp(i\omega d/c) \times (N'-1)^2 - \exp(-i\omega d/c) \times (N'+1)^2}{\exp(i\omega dN/c) \times (N'-N)^2 - \exp(-i\omega dN/c) \times (N'+N)^2} \tag{4.16}$$

for the filled cuvette, $E_{liq}(\omega)$, with refractive index N of the liquid inside the cuvette, again considering backreflections through the liquid. Data obtained in this way are depicted in Fig 4.19 and Fig 4.20 , where the THz dielectric function of water and methanol is shown for different concentrations of NaI.

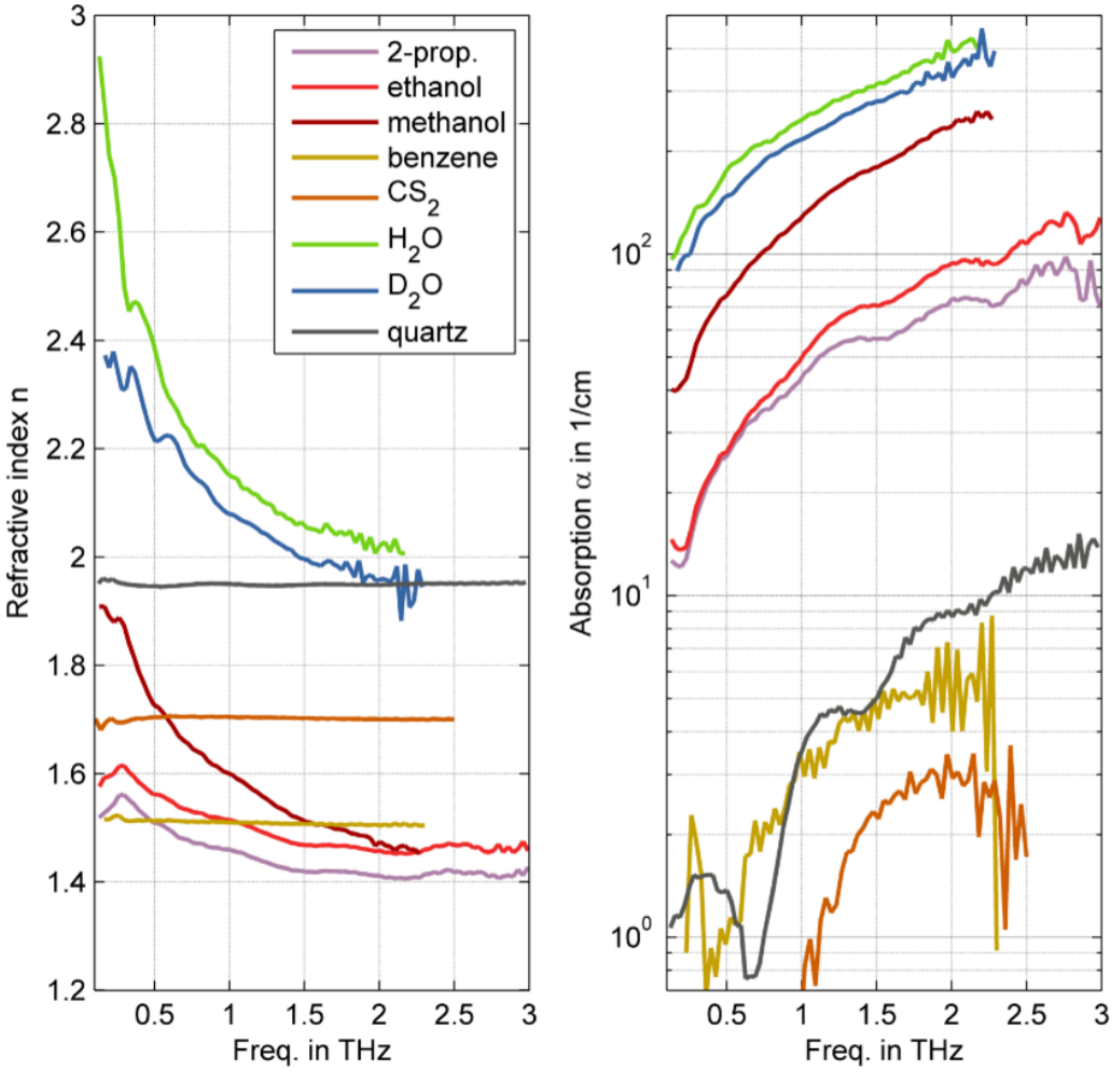

Fig. 4.19 THz complex refractive index of the liquids [57]. The spectra are obtained by time-domain spectroscopy (TDS). The large absorption coefficient of some liquids, water and methanol must be considered for the calculation of the Kerr coefficient. Periodic oscillations in the data are caused by interferences inside the cuvette, which are not fully subtracted by the transfer function formalism described here.

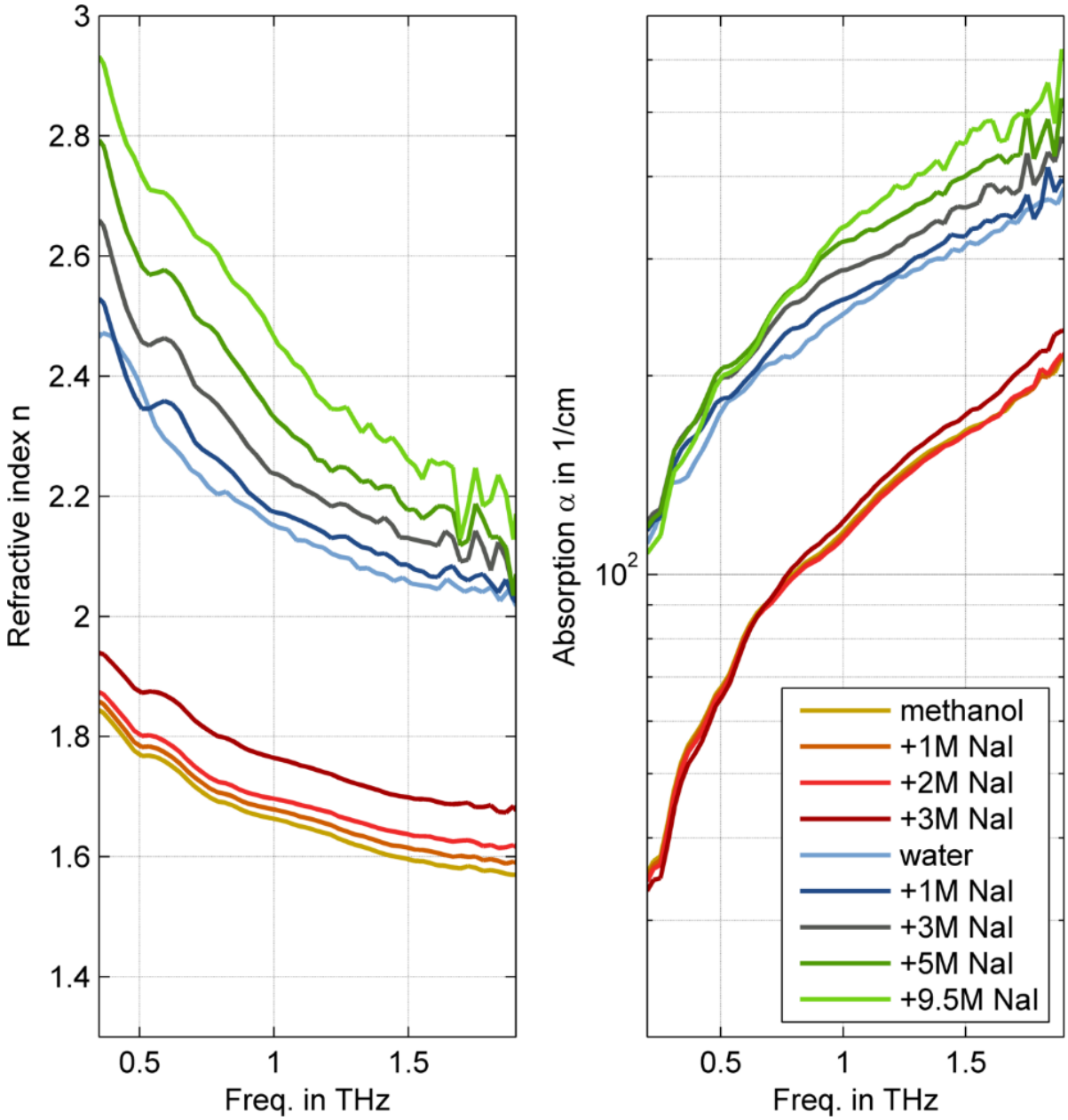

Fig. 4.20 Complex refractive index data of water and methanol at different concentrations of NaI, obtained using TDS [57]. In water and methanol there is a clear trend of increasing refractive index and only slight increase in absorption above about 1 THz.

Chapter 5

Ultrafast control of even-order harmonic generation from solids by an intense THz field

In this chapter, we will give a brief overview of high-harmonic generation in solids, followed by a general discussion of the crystalline symmetries of solids, which implies the symmetry control of harmonic generation in solids. Afterwards we present our experimental proofs of achieving ultrafast control of even-order harmonic generation from solids by an intense terahertz field. Uniquely, we can reduce the initial inversion symmetry to reach different symmetry classes using the THz field. And this could be extended to advanced symmetry control by manipulation of THz beam parameters(such as beam direction, polarization). The transient generation of even-order harmonics along the waveform of THz electric field is measured. For crystals without even-order susceptibility, such as Si and diamond, the intensity of the generated harmonics is affected by the THz polarization which determines the even-order nonlinear polarity. While for crystals with initial even-order susceptibility, such as GaAs, the even-order harmonic generation can be either enhanced or inhibited regarding the direction of the THz electric field. This study paves a way to ultrafast all-optical crystal symmetry control, which can be used in high-harmonic generation, optical frequency conversion, THz electric field measurement and other applications.

5.1 High-harmonic generation in solids

Historically, the invention of the laser [71] and the discovery of second-harmonic generation [72] opened the gate to the nonlinear optics world. Under the assumption that the laser

field strength is far smaller than the field strength of the outer shell electron feels on its orbital, these nonlinear phenomena are already well described by the anharmonic electronic response using perturbation theory. However, when the strength of the laser field is comparable to the atomic bonding strength of a material, this perturbation assumption fails and nonperturbative novel extreme nonlinear optical effects like high-harmonic generation (HHG) arise.

Traditionally, HHG from atomic gases has been well understood for decades through the well-known three-step model consisting of tunnel ionization, free acceleration, and recombination [73–75]. A typical spectrum of the radiation emitted from gas-phase HHG is odd harmonics with a plateau stretching out to the photon energy of $I_\mathrm{p} + 3.17U_\mathrm{p}$, where I_p is the ionization potential of the neutral atom and $U_\mathrm{p} = e^2E_0^2\lambda^2/16\pi^2mc^2$ is the ponderomotive energy. The E_0 and λ here are the peak field strength and wavelength of the laser, and e and m are the charge and mass of the electron, respectively. The strong-field approximation(SFA) [76], which neglects the contribution of the Coulomb potential to the propagation of the tunnel-ionized electrons in the laser field, builds the simplest recollision framework of this process.

High-order harmonic generation from bulk solids emerged, however, only recently from the year of 2010 [77]. The experimental set-up scheme is shown in Fig. 5.1a [77]. The laser pulse hits the 500-μm-thick ZnO crystal at peak intensity around $\sim 5\mathrm{TWcm}^{-2}$ (field strength$\sim 0.6\mathrm{V\AA}^{-1}$, pulse energy$\sim 3\mu$J) and generated high harmonics up to the 25th order without damaging the sample. The observed HHG spectrum featured a plateau as well as an abrupt high-energy cutoff beyond the ZnO band gap, which deviates strongly from a power law (harmonic order) expected from perturbative nonlinear optics. Notably, the cutoff energy from solids scale linearly with the peak field strength rather than a quadratic dependence predicted by the three-step model [73–75].

Thinking within the three-step model recollision picture, as the amplitude of the maximum excursion of a recolliding electron $r_\mathrm{max} = eE\lambda^2/4\pi^2mc^2 = 32\mathrm{\AA}$, which is many times the typical nearest neighbor distance. This suggests the possibility of ionization from one site and recombination on another, while it is still a coherent process thanks to the lattice periodicity (shown in Fig. 5.2a). Therefore, the single atom-based picture of HHG and the assumption of the strong-field approximation(SFA) [76] would be invalid here.

Following this initial solid HHG experiments in ZnO [77], a wide variety of other materials , including wide band gap dielectrics [79–81], 2D monolayer crystals (graphene [82] and MoS_2 [83]), have been investigated with pump wavelengths ranging from the THz to the near-infrared regions. This made a way to study the strong-field and ultrafast electron dynamics in the condensed phase. To understand the underlying microscopic mechanisms for solid-state HHG, several theoretical models have been proposed based on the intra- and interband electron dynamics [77, 79–81, 84–95]. A schematic comparison of the microscopic mechanism

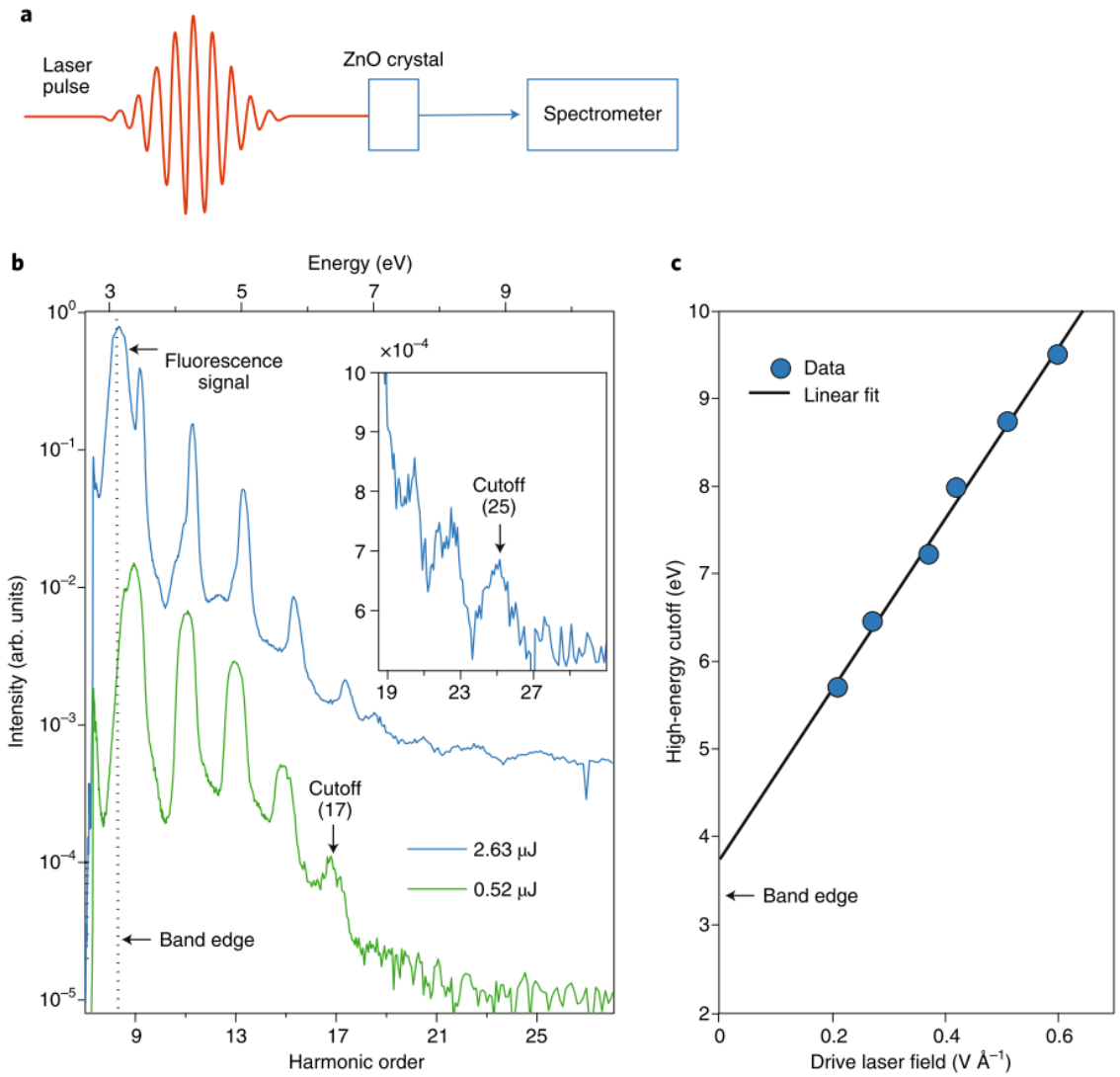

Fig. 5.1 High-order harmonic generation in ZnO crystals [78]. a, Schematic diagram of the experimental set-up. A 500-μm-thick sample is pumped by an intense femtosecond mid-infrared laser pulse and high harmonics are collected in transmission using a spectrometer. b, Representative measured spectra for two pulse energies. At 0.52 μ J, the spectrum extends to the 17th-order harmonic, which is well beyond the band edge (as shown by the dotted line). At 2.63 μ J, the spectrum extends further to the 25th-order harmonic. The arrows show the locations of abrupt cutoffs. c, High-energy cutoff as a function of the peak field, along with a linear fit. The intercept along the energy axis is near the bandgap (3.2 eV).

process between solid-state HHG and the standard three-step model in both real and momentum (reciprocal) space has been illustrated in Fig.5.2 [78]. In the real space shown in Fig.5.2a, scattered from the periodic Coulomb potential termed as Bloch oscillations, the driven electron could recombine with the associated hole (ion) and recollide with the first- and second-nearest

holes (ions). In the three-step model(shown in Fig.5.2c), however, the tunnel ionized electrons could only recombine with its parent ions.

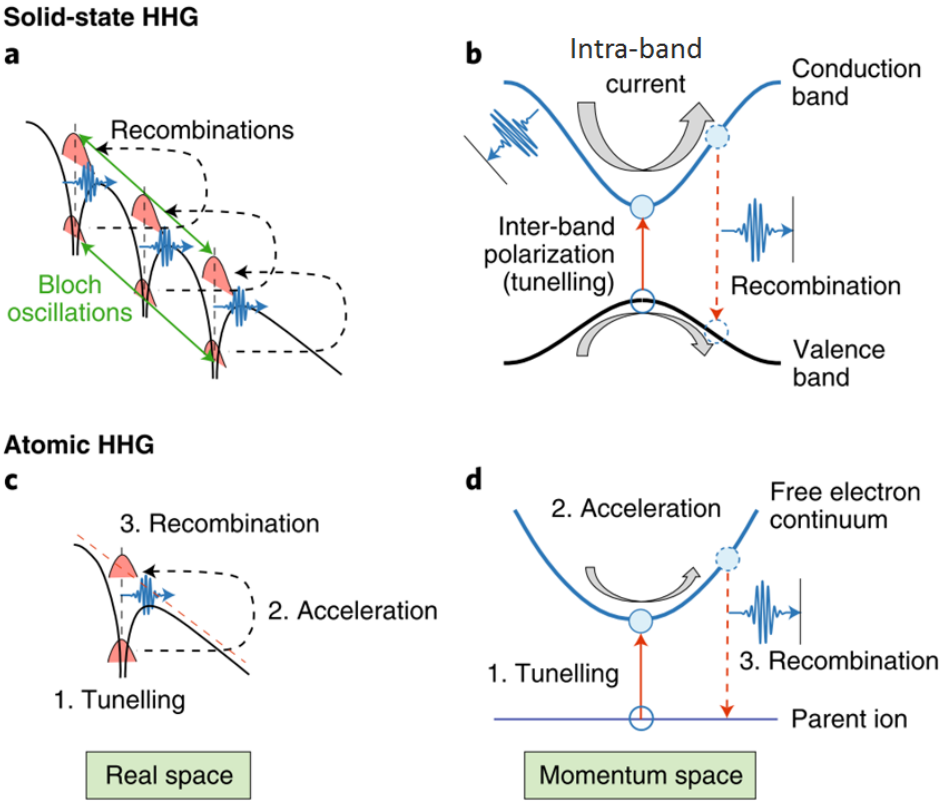

Fig. 5.2 Microscopic mechanisms for atomic and solid-state HHG [78]. a, The real-space picture with several possibilities; the driven electron could scatter from the periodic Coulomb potential termed as Bloch oscillations, recombine with the associated hole (ion) and recollide with the first- and second-nearest holes (ions) because of closely packed atoms. Periodic arrays of atoms in a crystal exhibit a collective response. b, The momentum-space version of a using simple cosine bands, showing intraband Bloch oscillations in the conduction band and interband coupling between the valance band and the conduction band, both emitting high-frequency radiation in the forward direction. c, Schematic diagram of the three-step model comprising tunnel ionization, free- acceleration and recombination. d, The momentum-space version of c, where the electron tunnels from the bound state to the continuum state, accelerates in the parabolic continuum band and then recombines to the bound state (parent ion) emitting high-frequency radiation.

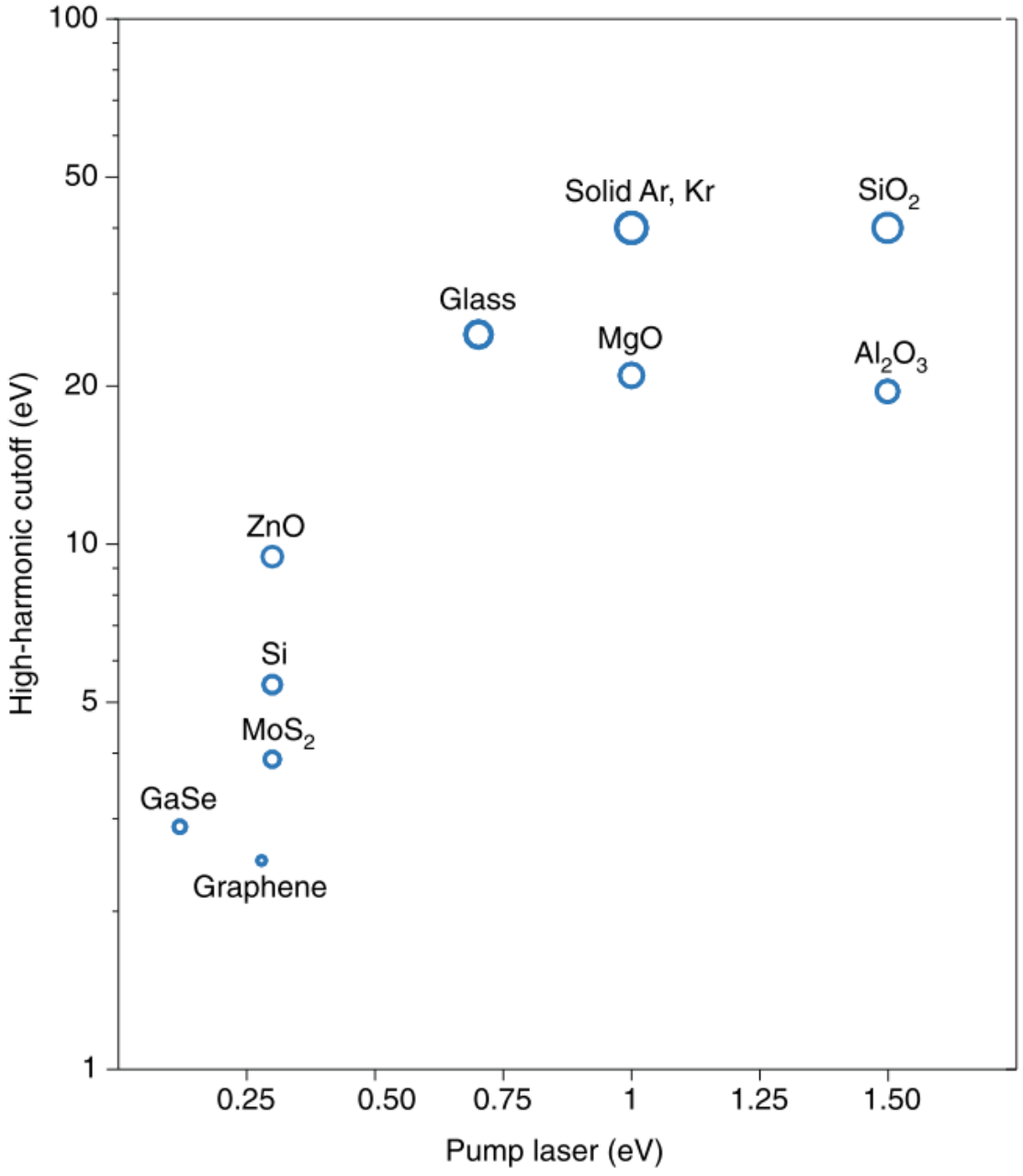

Fig. 5.3 Recent progress in high harmonics from solids [78]. The photon energy of the highest-order harmonic observed from a wide range of materials. Metals and semiconductors need terahertz or mid-IR fields because of the smaller bandgap. XUV photon energies have been generated in wide-bandgap dielectrics, as they can be pumped by near-IR laser fields with higher peak fields because of their higher damage threshold. The size and location of the circle approximately respectively represent the bandgap and high-energy cutoff. The materials are, in ascending order: graphene [82], GaSe [79], MoS_2 [96], Si [97], ZnO [77], MgO [98], glass [99], Al_2O_3 [100], SiO_2 [80], solid Kr and solid Ar [81].

5.2 Even harmonic generation and centro-symmetry

In nonlinear optics, even-harmonic generation is forbidden in centro-symmetric media. This could easily be deduced from the centro-symmetry property. The centro-symmetry (also called inversion symmetry) possesses a center of inversion. In the optical response formula 2.1, for a space inversion operation $r \to -r$, if we change the sign of the applied electric field $E(t) \to -E(t)$, the inversion symmetry leads to the sign of the induced $P(t) \to -P(t)$. Since $(-E(t))^2 = E^2(t)$,$(-E(t))^4 = E^4(t)$,... it follows that $\chi^{(2)} = \chi^{(4)} = \ldots = 0$. Therefore, even-harmonic generation is only possible in media without centro-symmetry. (In this assumption of formula 2.1 , we neglect the magnetic contribution to the nonlinear optical polarization P, or this conclusion will be invalid [101].)

5.3 Symmetry control of harmonic generation in solids

Since its first observation in 2011 [77, 86], high-order harmonic generation (HHG) in bulk crystalline materials suggests a promising route towards a new generation of compact high-harmonic sources. Developing techniques to deliberately manipulate the harmonics' properties, such as the harmonics' yields and polarization states [103, 104], becomes increasingly important for time-resolved spectroscopy of ultrafast electronic dynamics in the plethora of known solids and emerging quantum materials [105].

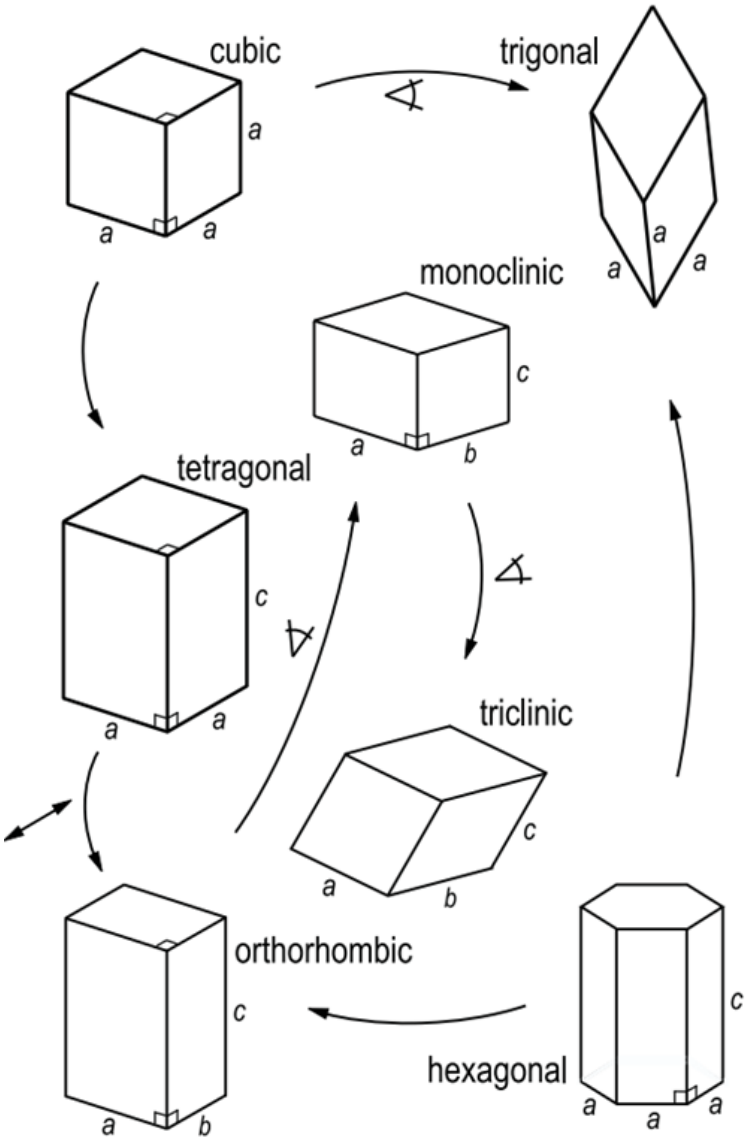

Fig. 5.4 The 7 crystal systems and their hierachy [102].

One viable approach is to control the selection rules of harmonic generation by reducing the symmetry of solids. This has been realized previously in conventional perturbative second-harmonic generation (forbidden in centrosymmetric crystals), e.g., by applying strain [106, 109], DC electric fields [107] in silicon waveguides, or even exploiting a strong THz pulse in an inorganic ferroelectric [108]. In nonperturbative high-order harmonic generation (HHG) from crystalline solids, symmetries also play a decisive role(shown in Fig. 5.8 [77]). Extending symmetry control to nonperturbative HHG [110, 97], we propose and demonstrate to use

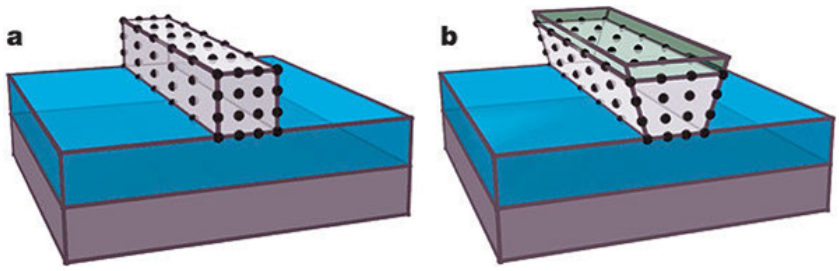

Fig. 5.5 Applying strain to crystalline silicon. a, Waveguide fabricated in the top layer of a silicon-on-insulator (SOI) wafer. b, The same waveguide with a straining layer deposited on top. The straining layer breaks the inversion symmetry and induces a linear electro-optic effect [106].

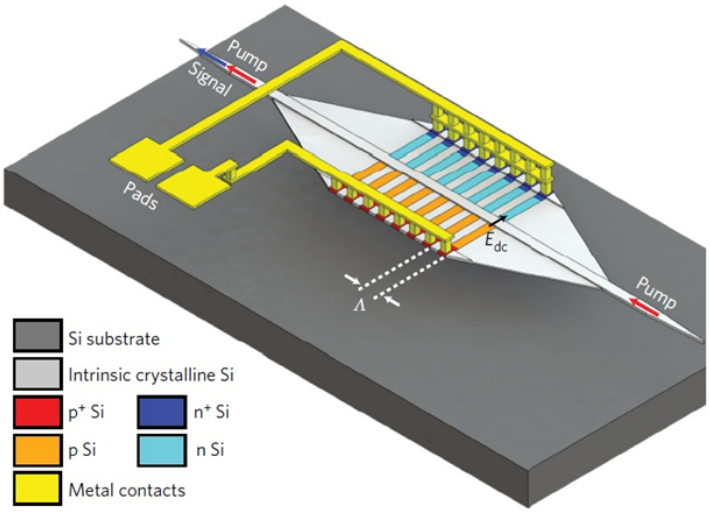

Fig. 5.6 Electric-Field Induced Second Harmonic(EFISH) [107].

an intense THz electric field to break the centro-symmetry of cubic crystals and therefore transiently reduce the symmetry of these crystals on a sub-THz-cycle time scale.

5.4 THz-dressing for ultrafast symmetry control of HHG in solids

To theoretically derive the impact of THz-dressing for the symmetry sensitive even harmonics emission in our solid system, we consider a centro-symmetric material, for which only the odd order response functions are non-zero by symmetry. In such material, the polarization can be expressed as

$$P = \sum_{i}^{\text{odd}} \chi^{(i)} E^i = \chi^{(1)} E + \chi^{(3)} EEE + \ldots \tag{5.1}$$

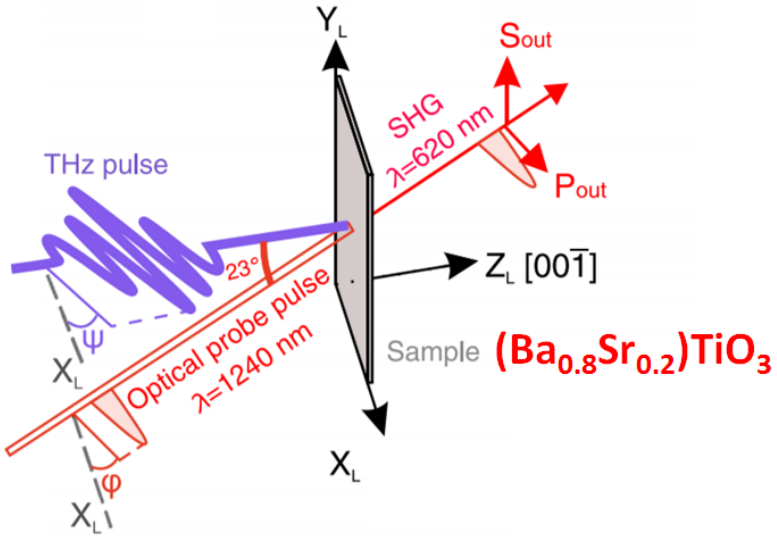

Fig. 5.7 THz Electric-Field Induced Second Harmonic Generation (THz EFISH) in the inorganic ferroelectric (Ba08Sr02)TiO3, which is explained by dynamical ferroelectric order parameter [108].

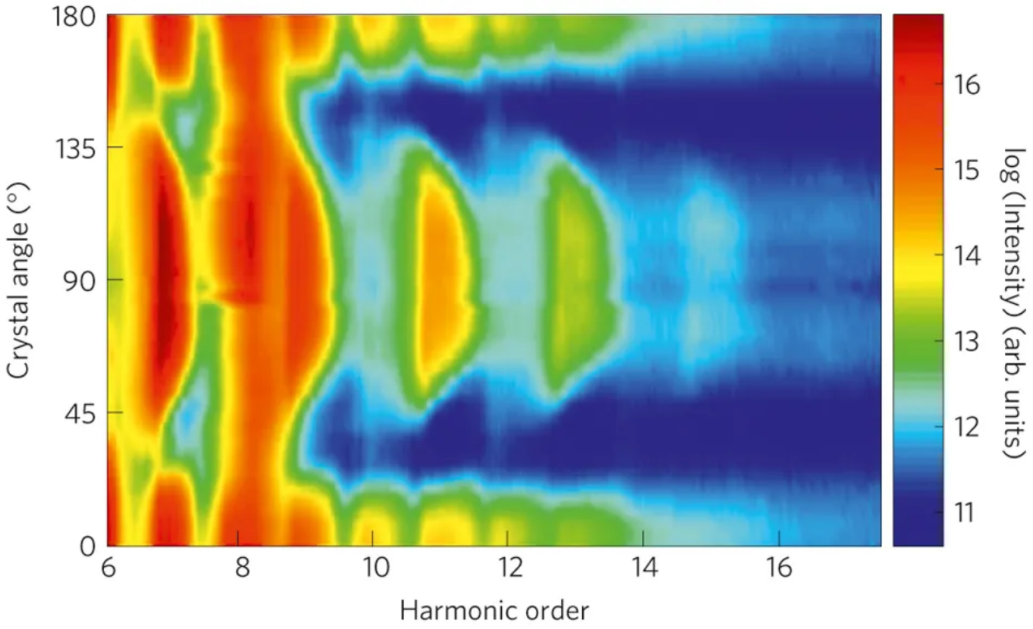

Fig. 5.8 The crystal angle rotation dependance of nonperturbative HHG in ZnO [77]

where $\chi^{(i)}$ is the i-th order response function. In the case of a driving field oscillating at a frequency ω, the polarization at 2ω and 3ω can be written as

$$P(2\omega) = 0 \tag{5.2}$$

$$P(3\omega) = \chi^{(3)} E(\omega)E(\omega)E(\omega) + \dots \tag{5.3}$$

We now assume that instead of the IR pump laser, we also add a THz field. We assume that the THz field is weak enough not to introduce non-linear effects whereas the IR goes up to the non-pertubative regime. As the THz wavelength is very long, we take it as explicitly 0 here, for conciseness of notations. We therefore now have

$$P(2\omega) = \chi^{(3)}(2\omega;\omega,\omega,0)E(\omega)E(\omega)E_{\mathrm{THz}} + \dots \tag{5.4}$$

$$P(3\omega) = \chi^{(3)}(3\omega;\omega,\omega,\omega)E(\omega)E(\omega)E(\omega) + \chi^{(4)}(3\omega;\omega,\omega,\omega,0)E(\omega)E(\omega)E(\omega)E_{\mathrm{THz}} + \dots \tag{5.5}$$

The THz field therefore induces second-harmonic generation, a phenomenon known as EFISH (electric field induced second harmonic). In fact, all even harmonics become available as the THz field breaks the inversion symmetry of the crystal. This becomes more obvious if we define an "effective" susceptibility, compared to the "bare" susceptibility, i.e., without the THz field. These effective susceptibilities read as

$$\chi^{(i)}_{\mathrm{eff}}(i\omega;\omega,\dots,\omega) = \chi^{(i)}(i\omega;\omega,\dots,\omega)E(\omega)^i + \chi^{(i+1)}(i\omega;\omega,\dots,\omega,0)E(\omega)^i E_{\mathrm{THz}} \tag{5.6}$$

Note that no-higher order susceptibilities are implicitly included in this expression. We indeed neglected the possible nonlinearities originating from the THz field. Two cases are present: i) An even harmonic, where the bare susceptibility is vanishing, due to the centro-symmetry. ii) Odd harmonics where the two terms in Eq. 5.6 contribute.

Let us now see what we can predict for the THz induced second-harmonic generation from Si($\bar{4}3m$), driven by a 2μm laser field.

For Si, there are only 4 non-zero components of the $\chi^{(3)}$, which are the components iiii, ijij, ijji, iijj. We denote $\mathbf{e}^{\omega}$ the polarization direction of the IR field, $\mathbf{e}^{\mathrm{THz}}$ the one of the THz, and $\mathbf{e}^{2\omega}$ the one of the emitted second harmonic. Therefore the polarization inside the medium is given by

$$\mathbf{P}(\mathbf{r};2\omega) = \overleftrightarrow{\chi}^{(3)}(\omega,\omega,0) : \mathbf{E}^{\omega}(\mathbf{r})\mathbf{E}^{\omega}(\mathbf{r})\mathbf{E}^{\mathrm{THz}}(\mathbf{r}) \tag{5.7}$$

where we assumed for simplicity that bulk quadrupolar and higher number of photons do not play any role.

We take the IR polarization to be in the x-y plane, with an angle α to the x direction, and the THz field is oriented under an angle β to the y direction. Taking the dipole approximation, i.e., the field is uniform in the material (except from a phase factor which is not relevant here), we obtain

$$\mathbf{P}(2\omega) = \frac{1}{3} \overset{\leftrightarrow(3)}{\chi} (\omega,\omega,0) : \left[\mathbf{E}^{\omega}\mathbf{E}^{\omega}\mathbf{E}^{\mathrm{THz}} + \mathbf{E}^{\omega}\mathbf{E}^{\mathrm{THz}}\mathbf{E}^{\omega} + \mathbf{E}^{\mathrm{THz}}\mathbf{E}^{\omega}\mathbf{E}^{\omega}\right] \tag{5.8}$$

To make things explicit, we obtain after some algebra that

$$\begin{aligned}
\mathbf{E}^{\omega}\mathbf{E}^{\omega}\mathbf{E}^{\mathrm{THz}}/\left|\mathbf{E}^{\omega}\right|^2\left|\mathbf{E}^{\mathrm{THz}}\right| = &\cos(\alpha)^2(\cos(\beta)\hat{\mathbf{x}}\hat{\mathbf{x}}\hat{\mathbf{x}} + \sin(\beta)\hat{\mathbf{x}}\hat{\mathbf{x}}\hat{\mathbf{y}}) \\
&+ \cos(\alpha)\sin(\alpha)\cos(\beta)(\hat{\mathbf{x}}\hat{\mathbf{y}}\hat{\mathbf{x}} + \hat{\mathbf{y}}\hat{\mathbf{x}}\hat{\mathbf{x}}) \\
&+ \cos(\alpha)\sin(\alpha)\sin(\beta)(\hat{\mathbf{x}}\hat{\mathbf{y}}\hat{\mathbf{y}} + \hat{\mathbf{y}}\hat{\mathbf{x}}\hat{\mathbf{y}}) \\
&+ \sin(\alpha)^2(\cos(\beta)\hat{\mathbf{y}}\hat{\mathbf{y}}\hat{\mathbf{x}} + \sin(\beta)\hat{\mathbf{y}}\hat{\mathbf{y}}\hat{\mathbf{y}})
\end{aligned} \tag{5.9}$$

$$\begin{aligned}
\mathbf{E}^{\omega}\mathbf{E}^{\mathrm{THz}}\mathbf{E}^{\omega}/\left|\mathbf{E}^{\omega}\right|^2\left|\mathbf{E}^{\mathrm{THz}}\right| = &\cos(\alpha)^2(\cos(\beta)\hat{\mathbf{x}}\hat{\mathbf{x}}\hat{\mathbf{x}} + \sin(\beta)\hat{\mathbf{x}}\hat{\mathbf{y}}\hat{\mathbf{x}}) \\
&+ \cos(\alpha)\sin(\alpha)\cos(\beta)(\hat{\mathbf{x}}\hat{\mathbf{x}}\hat{\mathbf{y}} + \hat{\mathbf{y}}\hat{\mathbf{x}}\hat{\mathbf{x}}) \\
&+ \cos(\alpha)\sin(\alpha)\sin(\beta)(\hat{\mathbf{x}}\hat{\mathbf{y}}\hat{\mathbf{y}} + \hat{\mathbf{y}}\hat{\mathbf{y}}\hat{\mathbf{x}}) \\
&+ \sin(\alpha)^2(\cos(\beta)\hat{\mathbf{y}}\hat{\mathbf{x}}\hat{\mathbf{y}} + \sin(\beta)\hat{\mathbf{y}}\hat{\mathbf{y}}\hat{\mathbf{y}})
\end{aligned} \tag{5.10}$$

$$\begin{aligned}
\mathbf{E}^{\mathrm{THz}}\mathbf{E}^{\omega}\mathbf{E}^{\omega}/\left|\mathbf{E}^{\omega}\right|^2\mathbf{E}^{\mathrm{THz}}| = &+\cos(\alpha)^2(\cos(\beta)\hat{\mathbf{x}}\hat{\mathbf{x}}\hat{\mathbf{x}} + \sin(\beta)\hat{\mathbf{y}}\hat{\mathbf{x}}\hat{\mathbf{x}}) \\
&+ \cos(\alpha)\sin(\alpha)\cos(\beta)(\hat{\mathbf{x}}\hat{\mathbf{x}}\hat{\mathbf{y}} + \hat{\mathbf{x}}\hat{\mathbf{y}}\hat{\mathbf{x}}) \\
&+ \cos(\alpha)\sin(\alpha)\sin(\beta)(\hat{\mathbf{y}}\hat{\mathbf{x}}\hat{\mathbf{y}} + \hat{\mathbf{x}}\hat{\mathbf{y}}\hat{\mathbf{x}}) \\
&+ \sin(\alpha)^2(\cos(\beta)\hat{\mathbf{x}}\hat{\mathbf{y}}\hat{\mathbf{y}} + \sin(\beta)\hat{\mathbf{y}}\hat{\mathbf{y}}\hat{\mathbf{y}})
\end{aligned} \tag{5.11}$$

As we know the non-zero matrix elements for $\chi^{(3)}$ for silicon, we end up with

$$\begin{aligned}
\frac{\mathbf{P}(2\omega)}{3|\mathbf{E}^{\omega}|^2|\mathbf{E}^{\mathrm{THz}}|} &= 3\cos(\alpha)^2\cos(\beta)\hat{\mathbf{x}}\chi^{(3)}_{xxxx}(\omega,\omega,0)\\
&\cos(\alpha)^2\sin(\beta)\hat{\mathbf{y}}\chi^{(3)}_{yxyx}(\omega,\omega,0)+\cos(\alpha)\sin(\alpha)\cos(\beta)\left(\hat{\mathbf{y}}\chi^{(3)}_{yxyx}(\omega,\omega,0)+\hat{\mathbf{y}}\chi^{(3)}_{yyxx}(\omega,\omega,0)\right)\\
&+\cos(\alpha)\sin(\alpha)\sin(\beta)\left(\hat{\mathbf{x}}\chi^{(3)}_{xxyy}(\omega,\omega,0)+\hat{\mathbf{x}}\chi^{(3)}_{xyxy}(\omega,\omega,0)\right)+\sin(\alpha)^2\cos(\beta)\hat{\mathbf{x}}\chi^{(3)}_{xyxy}(\omega,\omega,0)\\
&+\cos(\alpha)^2\sin(\beta)\hat{\mathbf{y}}\chi^{(3)}_{yxyx}(\omega,0,\omega)+\cos(\alpha)\sin(\alpha)\cos(\beta)\left(\hat{\mathbf{y}}\chi^{(3)}_{yxxy}(\omega,0,\omega)+\hat{\mathbf{y}}\chi^{(3)}_{yyxx}(\omega,0,\omega)\right)\\
&+\cos(\alpha)\sin(\alpha)\sin(\beta)\left(\hat{\mathbf{x}}\chi^{(3)}_{xxyy}(\omega,0,\omega)+\hat{\mathbf{x}}\chi^{(3)}_{xyyx}(\omega,0,\omega)\right)+\sin(\alpha)^2\cos(\beta)\hat{\mathbf{x}}\chi^{(3)}_{xyxy}(\omega,0,\omega)\\
&+\cos(\alpha)^2\sin(\beta)\hat{\mathbf{y}}\chi^{(3)}_{yyxx}(0,\omega,\omega)+\cos(\alpha)\sin(\alpha)\cos(\beta)\left(\hat{\mathbf{y}}\chi^{(3)}_{yxxy}(0,\omega,\omega)+\hat{\mathbf{y}}\chi^{(3)}_{yxyx}(0,\omega,\omega)\right)\\
&+\cos(\alpha)\sin(\alpha)\sin(\beta)\left(\hat{\mathbf{x}}\chi^{(3)}_{xyxy}(0,\omega,\omega)+\hat{\mathbf{x}}\chi^{(3)}_{xyyx}(0,\omega,\omega)\right)+\sin(\alpha)^2\cos(\beta)\hat{\mathbf{x}}\chi^{(3)}_{xxyy}(0,\omega,\omega)\\
&+3\sin(\alpha)^2\sin(\beta)\hat{\mathbf{y}}\chi^{(3)}_{yyyy}(\omega,\omega,0).
\end{aligned} \tag{5.12}$$

where we explicitly added the frequency dependence to avoid any mistake and confusion. In order to simplify this expression, we use the permutation rules

$$\begin{aligned}
\frac{\mathbf{P}(2\omega)}{|\mathbf{E}^{\omega}|^2|\mathbf{E}^{\mathrm{THz}}|} &= \cos(\alpha)^2\cos(\beta)\hat{\mathbf{x}}\chi^{(3)}_{xxxx}(\omega,\omega,0)\\
&\cos(\alpha)^2\sin(\beta)\hat{\mathbf{y}}\chi^{(3)}_{yxxy}(\omega,\omega,0)\\
&+\hat{\mathbf{y}}\cos(\alpha)\sin(\alpha)\cos(\beta)\left[\chi^{(3)}_{yyxx}(\omega,\omega,0)+\chi^{(3)}_{yxyx}(\omega,\omega,0)\right]\\
&+\hat{\mathbf{x}}\cos(\alpha)\sin(\alpha)\sin(\beta)\left[\chi^{(3)}_{xxyy}(\omega,\omega,0)+\chi^{(3)}_{xyxy}(\omega,\omega,0)\right)]\\
&+\hat{\mathbf{x}}\sin(\alpha)^2\cos(\beta)\chi^{(3)}_{xyyx}(\omega,\omega,0)\\
&+\hat{\mathbf{y}}\sin(\alpha)^2\sin(\beta)\chi^{(3)}_{yyyy}(\omega,\omega,0)
\end{aligned} \tag{5.13}$$

We can further factorize this expression into

$$\begin{aligned}
\frac{\mathbf{P}(2\omega)}{|\mathbf{E}^{\omega}|^2|\mathbf{E}^{\mathrm{THz}}|} &= \hat{\mathbf{x}}\left(\cos(\alpha)^2\cos(\beta)\chi^{(3)}_{xxxx}(\omega,\omega,0)+\sin(\alpha)^2\cos(\beta)\chi^{(3)}_{xyyx}(\omega,\omega,0)\right.\\
&\left.+\cos(\alpha)\sin(\alpha)\sin(\beta)\left[\chi^{(3)}_{xxyy}(\omega,\omega,0)+\chi^{(3)}_{xyxy}(\omega,\omega,0)\right)]\right)\\
&+\hat{\mathbf{y}}\left(\cos(\alpha)^2\sin(\beta)\chi^{(3)}_{yxxy}(\omega,\omega,0)+\sin(\alpha)^2\sin(\beta)\chi^{(3)}_{yyyy}(\omega,\omega,0)\right.\\
&\left.+\hat{\mathbf{y}}\cos(\alpha)\sin(\alpha)\cos(\beta)\left[\chi^{(3)}_{yyxx}(\omega,\omega,0)+\chi^{(3)}_{yxyx}(\omega,\omega,0)\right]\right)
\end{aligned} \tag{5.14}$$

We finally note that $\chi^{(3)}_{xxyy}(\omega,\omega,0)=\chi^{(3)}_{xyxy}(\omega,\omega,0)$ due to cubic symmetry. Thus

$$\begin{aligned}
\mathbf{P}(2\omega) &= \hat{\mathbf{x}}\left(\cos(\alpha)^2\cos(\beta)\chi^{(3)}_{xxxx}(\omega,\omega,0)+\sin(\alpha)^2\cos(\beta)\chi^{(3)}_{xyyx}(\omega,\omega,0)\right.\\
&\left.+2\cos(\alpha)\sin(\alpha)\sin(\beta)\chi^{(3)}_{xyxy}(\omega,\omega,0))\right)|\mathbf{E}^{\omega}|^2\left|\mathbf{E}^{\mathrm{THz}}\right|\\
&+\hat{\mathbf{y}}\left(\cos(\alpha)^2\sin(\beta)\chi^{(3)}_{yxxy}(\omega,\omega,0)+\sin(\alpha)^2\sin(\beta)\chi^{(3)}_{yyyy}(\omega,\omega,0)\right.\\
&\left.+2\cos(\alpha)\sin(\alpha)\cos(\beta)\chi^{(3)}_{yxyx}(\omega,\omega,0))\right)|\mathbf{E}^{\omega}|^2\left|\mathbf{E}^{\mathrm{THz}}\right|
\end{aligned} \tag{5.15}$$

The values of $\chi^{(3)}_{ijkl}(\omega,\omega,0)$ have been computed in the PhD thesis of Lucie Prussel [111] and it was found from first-principles, at $\omega = 0.4$eV , that $|\chi^{(3)}_{iiii}(\omega,\omega,0))| = 0.479\times10^4$a.u., $|\chi^{(3)}_{ijij}(\omega,\omega,0))| = 0.227\times10^4$ *a.u.*, and $|\chi^{(3)}_{ijji}(\omega,\omega,0))| = 0.215\times10^4$ *a.u.*. The fact that $\chi^{(3)}_{ijij}(\omega,\omega,0)$ and $\chi^{(3)}_{ijji}(\omega,\omega,0)$ are very similar is expected from Kleinman symmetries in the limit $\omega\to0$.

Taking these values, one obtains the angular plot for the second-harmonic with THz dressing is shown in Fig. 5.9. We obtain here that the second harmonic induced by the THz field has two-fold symmetry, as observed experimentally. We can redo the same for the term corresponding to the third harmonic, but without the THz field

$$\mathbf{P}(\mathbf{r};3\omega) = \overset{\leftrightarrow}{\chi}^{(3)}(\omega,\omega,0) : \mathbf{E}^{\omega}(\mathbf{r})\mathbf{E}^{\omega}(\mathbf{r})\mathbf{E}^{\omega}(\mathbf{r}) \tag{5.16}$$

We obtain

$$\begin{aligned}\mathbf{P}(3\omega) = &\left(\hat{\mathbf{x}}\cos(\alpha)^3+\hat{\mathbf{y}}\sin(\alpha)^3\right)\chi^{(3)}_{iiij}|\mathbf{E}^{\omega}|^3\\ &+\hat{\mathbf{y}}\cos(\alpha)^2\sin(\alpha)\left[\chi^{(3)}_{ijji}+\chi^{(3)}_{ijij}+\chi^{(3)}_{iijj}\right]|\mathbf{E}^{\omega}|^3\\ &+\hat{\mathbf{x}}\sin(\alpha)^2\cos(\alpha)\left[\chi^{(3)}_{iijj}+\chi^{(3)}_{ijji}+\chi^{(3)}_{ijij}\right]|\mathbf{E}^{\omega}|^3\end{aligned} \tag{5.17}$$

$$\begin{aligned}\mathbf{P}(3\omega) = &\left(\hat{\mathbf{x}}\cos(\alpha)^3+\hat{\mathbf{y}}\sin(\alpha)^3\right)\chi^{(3)}_{iiii}|\mathbf{E}^{\omega}|^3\\ &+[\cos(\alpha)\hat{\mathbf{y}}+\sin(\alpha)\hat{\mathbf{x}}]\cos(\alpha)\sin(\alpha)\left[\chi^{(3)}_{ijji}+\chi^{(3)}_{ijij}+\chi^{(3)}_{iijj}\right]|\mathbf{E}^{\omega}|^3\end{aligned} \tag{5.18}$$

As $\chi^{(3)}_{ijij}(\omega,\omega,\omega) = \chi^{(3)}_{iijj}(\omega,\omega,\omega) = \chi^{(3)}_{ijji}(\omega,\omega,\omega)$, we obtain for the previous expressions

$$\begin{aligned}\mathbf{P}(3\omega) = &\left(\hat{\mathbf{x}}\cos(\alpha)^3+\hat{\mathbf{y}}\sin(\alpha)^3\right)\chi^{(3)}_{iiii}(\omega,\omega,\omega)|\mathbf{E}^{\omega}|^3\\ &+3[\cos(\alpha)\hat{\mathbf{y}}+\sin(\alpha)\hat{\mathbf{x}}]\cos(\alpha)\sin(\alpha)\chi^{(3)}_{ijij}(\omega,\omega,\omega)|\mathbf{E}^{\omega}|^3\end{aligned} \tag{5.19}$$

An values for $\left|\chi^{(3)}_{ijij}(\omega,\omega,\omega)\right|$ and $\left|\chi^{(3)}_{iiii}(\omega,\omega,\omega)\right|$ can be estimated from the results of Ref. [112] in which these values were computed from first principles. At 0.5eV, one obtains that $\left|\chi^{(3)}_{ijij}(\omega,\omega,\omega)\right| = 0.06\times10^{-10}$cgs and $\left|\chi^{(3)}_{iiii}(\omega,\omega,\omega)\right| = 0.11\times10^{-10}$cgs. Moreover these two response functions have the same phase, see Fig. 8 of Ref. [112]. Taking these values, one obtains the following angular plot for the third harmonic without THz dressing shown in Fig. 5.10. The third harmonic here has four-fold symmetry, as expected from (cubic) silicon. This section is based on the theoretical work of our collaborator Nicolas Tancogne-Dejean.

5.5 TDDFT simulation

Time-dependent density-functional theory (TDDFT) simulations of even-order HHG from THz-dressed silicon was performed by our collaborator Nicolas Tancogne-Dejean(the method

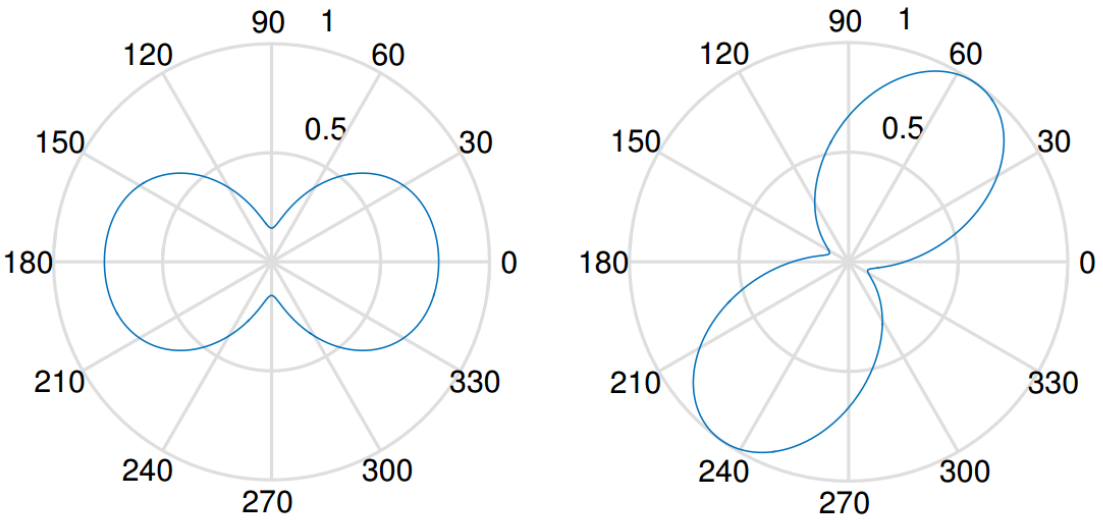

Fig. 5.9 $|P(2\omega)|^2$ as given by equation (5.14) for $\beta = 0°$ (left panel) and $\beta = 131°$ (right panel). The two plots are normalized together.

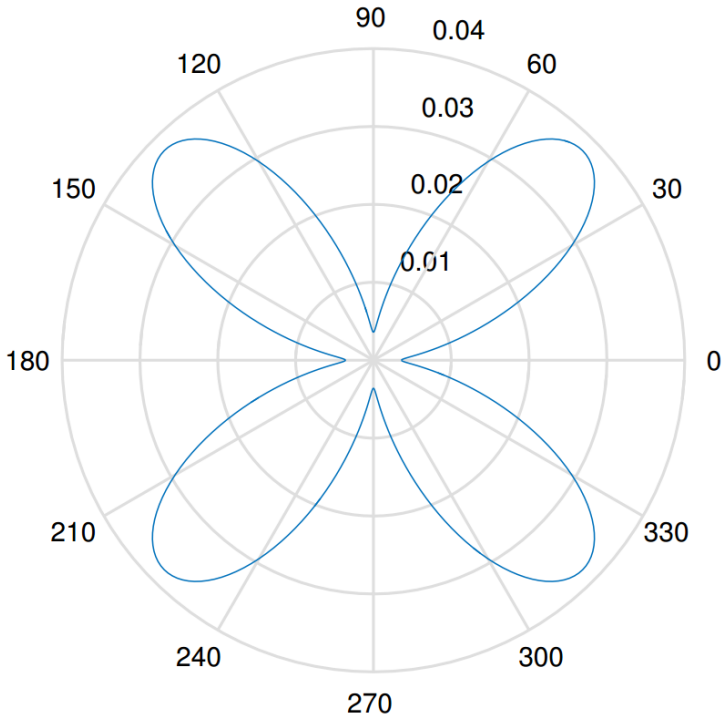

Fig. 5.10 The four-fold symmetry of third harmonics generation $|P(3\omega)|^2$ as given by equation (5.19).

Ref. [103, 85]). The ab-initio approach is based on time-dependent density-functional theory (TDDFT) [113, 114]. The conditions for the TDDFT simulation are as follows:

- Driving laser pulse of 25-fs duration, with a sin-square envelope of the vector potential;
- The peak intensity inside silicon is taken to be $I_0 = 10^{12}\mathrm{W/cm}^{-2}$;
- the carrier wavelength λ is 800 nm and the THz frequency is centered at 33 THz (both chosen for numerical reasons).

The evolution of the wave-functions and the evaluation of the time-dependent current is computed by propagating the Kohn-Sham equations within TDDFT, as provided by the Octopus package [115], in the local density approximation (LDA). The calculated Fig. 5.11 reveals that in centro-symmetric materials (such as Si), the even-harmonic generation can be realized by dressing the solid with a relatively weak THz field (compared to the field strength of IR wave). Moreover, for parallel polarizations, it is predicted that the intensity of the transiently induced even-order harmonics in Si should be 3 times higher than for orthogonal polarizations.

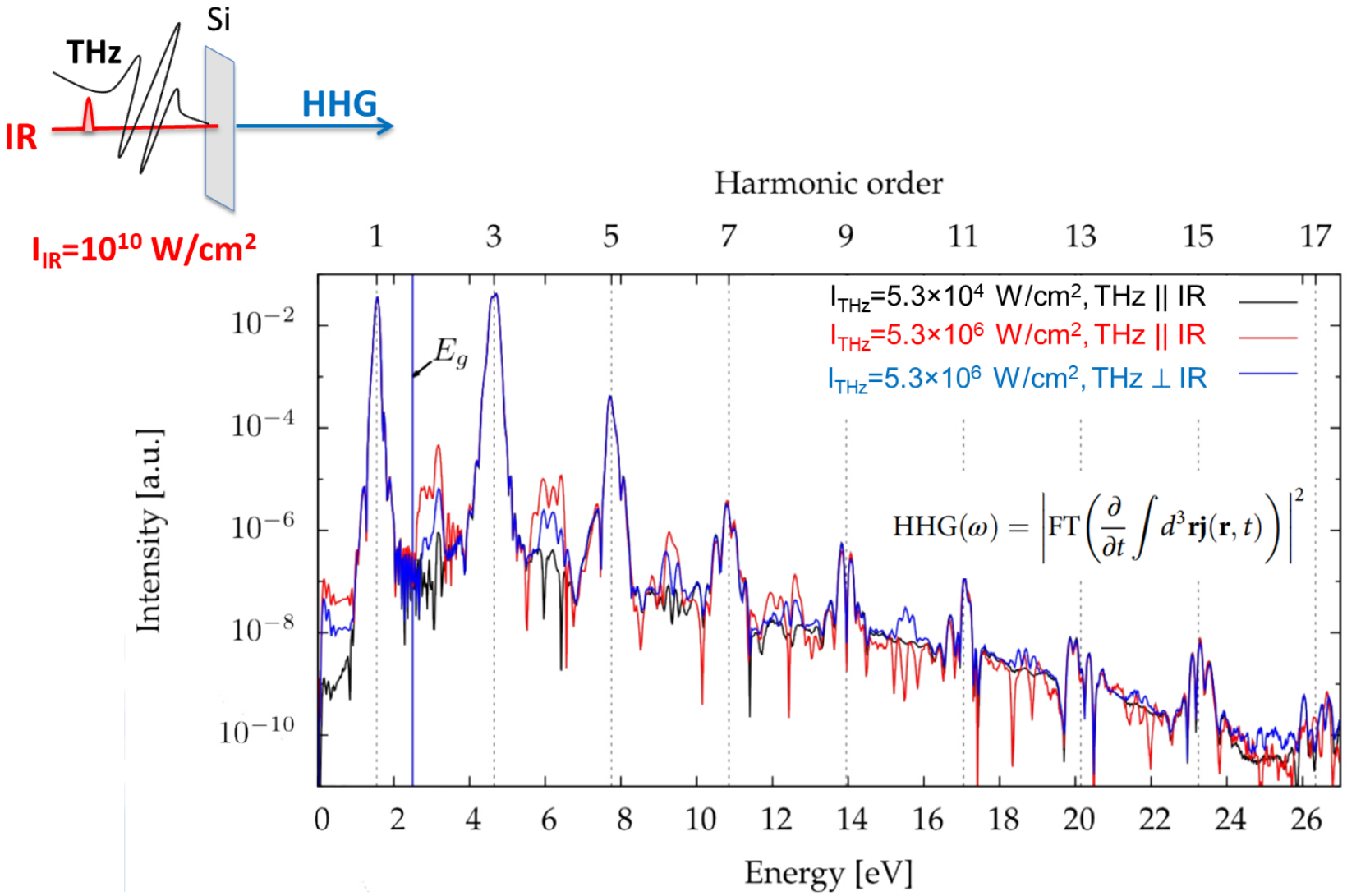

Fig. 5.11 TDDFT simulation of even-order HHG from THz-dressed silicon done by our collaborator Nicolas Tancogne-Dejean(the method ref [103, 85])

5.6 Experimental setup

The centro-symmetric crystal systems we study are the cubic systems diamond and silicon. Specifically, we choose free-standing, (100)-cut, 1-μm-thick and (110)-cut, 5-μm-thick Si crystals as well as a free-standing, (110)-cut, 20-μm-thick diamond crystal as samples. The experimental setup is shown in Fig. 5.12. The laser system employed for the experiments is a home-built infrared (IR) optical parametric amplifier (OPA) pumped by a Ti:sapphire chirped-pulse amplifier with the fundamental wavelength of 800nm, 40-fs pulse duration, 3k repetition rate, and 4-mJ pulse energy (Coherent Elite DUO, Coherent Inc.). The details of this OPA are described in chapter 2. The signal and idler pulses of the OPA are centered at wavelengths of 1.55 μm and 1.75 μm, respectively [8]. By optical rectification of the signal pulse in a 0.6-mm-thick DSTMS crystal [23] (Rainbow Photonics Inc.) , a $\sim 6\mu$ J THz pulse centered at $\sim$ 2.5 THz is generated. After being combined on a pellicle beam splitter, the THz and idler pulses are then focused onto the sample at normal incidence. A half-wave plate (HWP) is used to adjust the polarization direction of the IR idler driving field. The generated harmonics are recorded by an Ocean Optics USB2000 spectrometer. The IR beam is centered at 1.75μm with 60fs pulse duration, and the intensity is 1.5×10^{12} W/cm^2, which ensures that the high harmonic generation is in the nonperturbative regime. The THz beam is centered at 2.5THz with 5×10^7 W/cm^2 peak intensity. The THz electric field is characterized via electro-optical sampling (EOS) with a 100-μm-thick GaP crystal (see Fig. 5.15). Note that the generated intense THz field is still a comparably weak, perturbative dressing field compared to the strong IR driving field.

5.7 Experimental results

The breaking of the centro-symmetry can also be realized by applying strain or DC electric fields. The advantage of our terahertz-dressing scheme lies in the versatility in controlling the polarization state and direction of the perturbing terahertz field.

Fig. 5.14 shows the importance of controlling the polarization direction of the THz-dressing field with respect to the infrared driving field. For parallel polarization, the intensity of the transiently induced even-order harmonics is $\sim$3 times higher than for orthogonal polarization, in agreement with the TDDFT simulations [103, 85]. This flexibility of control would not be possible with a custom-fabricated silicon platform, such as strained waveguides.

In Fig. 5.15 shows the even-order harmonics (2nd, 4th, and 6th) spectra from silicon versus time delay of THz electric field (bottom panel) for parallel polarization configuration (IR $\parallel$ THz). Meanwhile, the compare spectra of the even-order harmonics (2nd and 4th) in Si and diamond

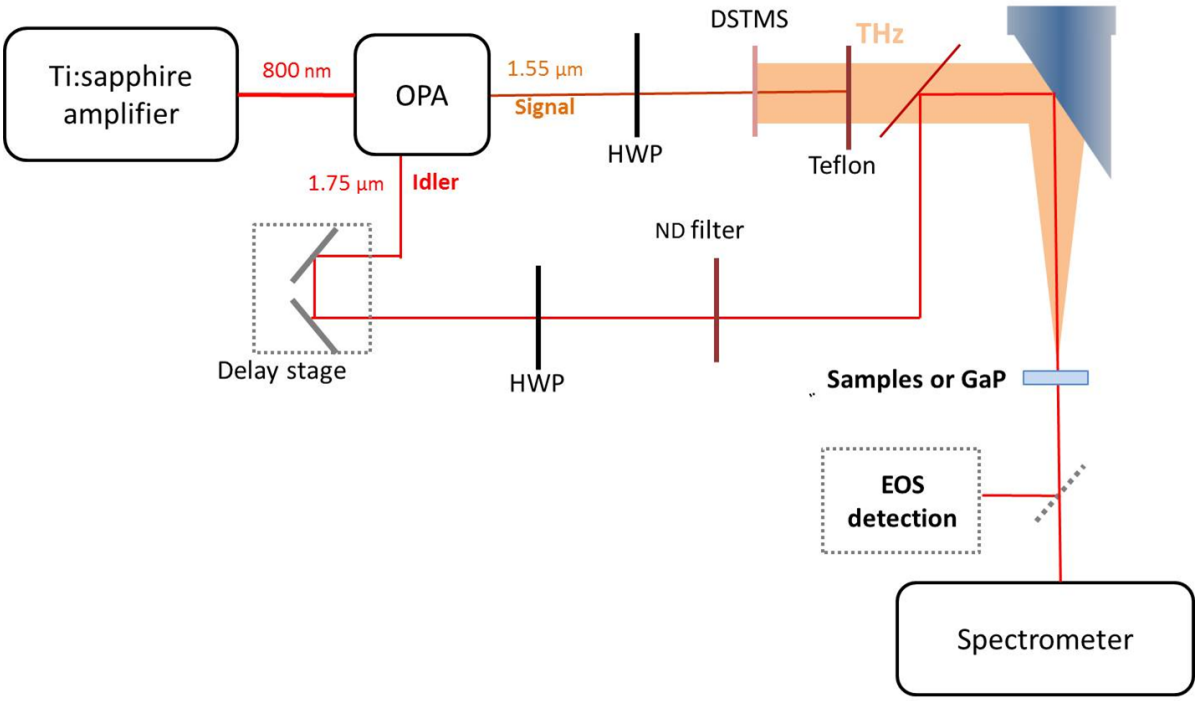

Fig. 5.12 Scheme of the experimental setup: OPA, optical parametric amplifier; HWP, half-wave plate; DSTMS, organic crystal [23]; ND filter, neutral density filter; EOS, electro-optic sampling employing a GaP crystal.

versus time delay of THz electric field (bottom panel) for parallel polarization configuration (IR ∥ THz) are shown in Fig. 5.16. The transient generation of even-order harmonics along the THz electric field is measured. For crystals without even- order susceptibility, such as Si and diamond, the intensity of the generated harmonics is affected by the THz polarization which determines the even-order nonlinear polarity.

we also investigated the sample rotation dependence of induced even-order harmonics in Si. In Fig. 5.15, we observe a four-fold symmetry of the 2nd, 4th, and 6th harmonics, compatible with reducing the cubic symmetry of bare silicon to a tetragonal symmetry of dressed silicon.

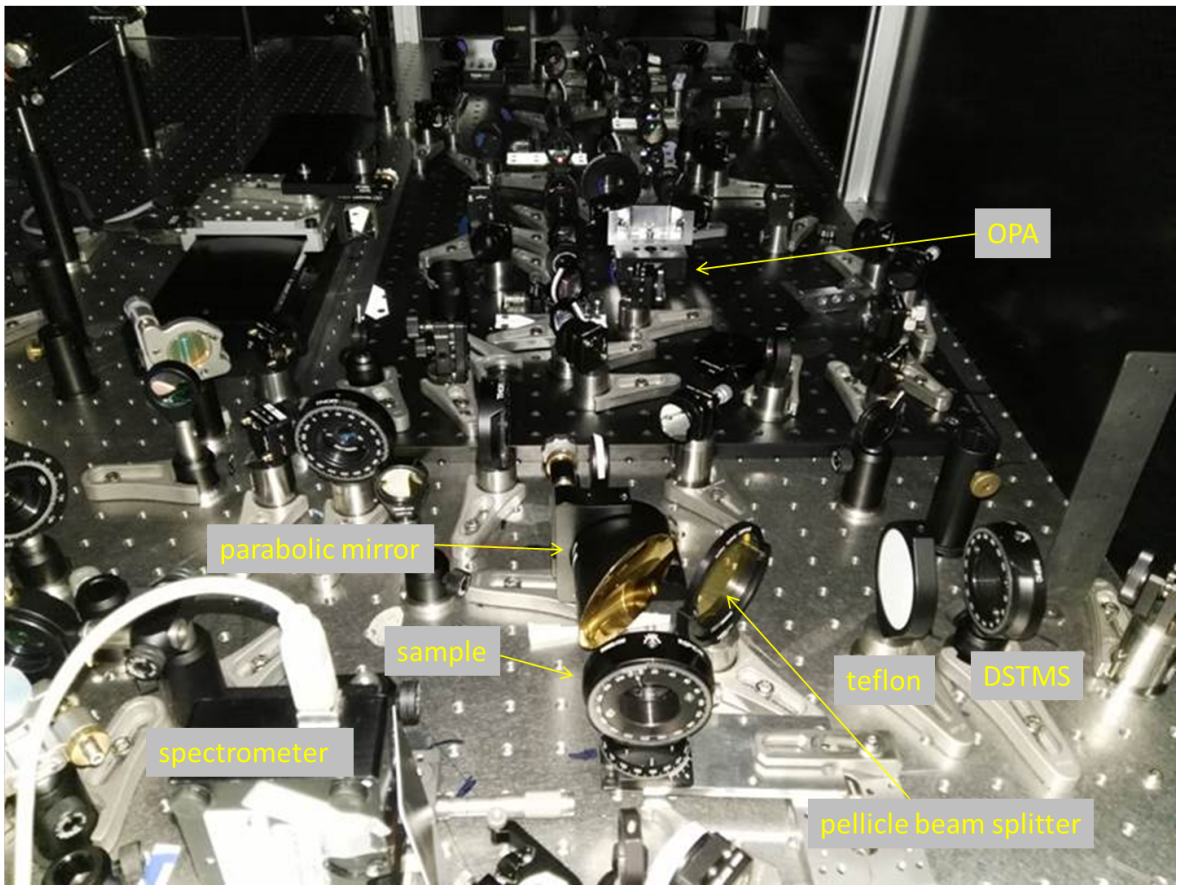

Fig. 5.13 Experimental setup in the lab. The IR OPA is built on the breadboard in the background. In the foreground, from right to left labeled the DSTMS crystal mounted in the black rotator, the white Teflon, the pellicle beam splitter, the parabolic mirror, sample holder, and the Ocean Optics USB2000 spectrometer.

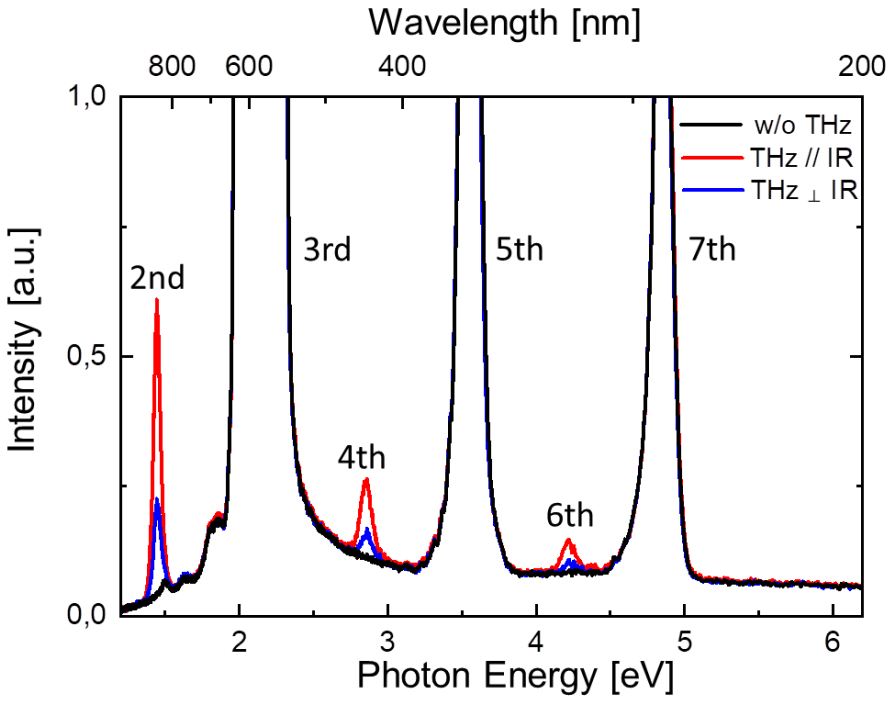

Fig. 5.14 Higher-harmonic spectra from bare (without THz, black curve) and dressed silicon for polarization of the intense THz transient parallel (blue curve) and orthogonal (red curve) with respect to the infrared driving polarization. Even-order harmonics ∼3 times stronger for parallel than for orthogonal polarizations [110].

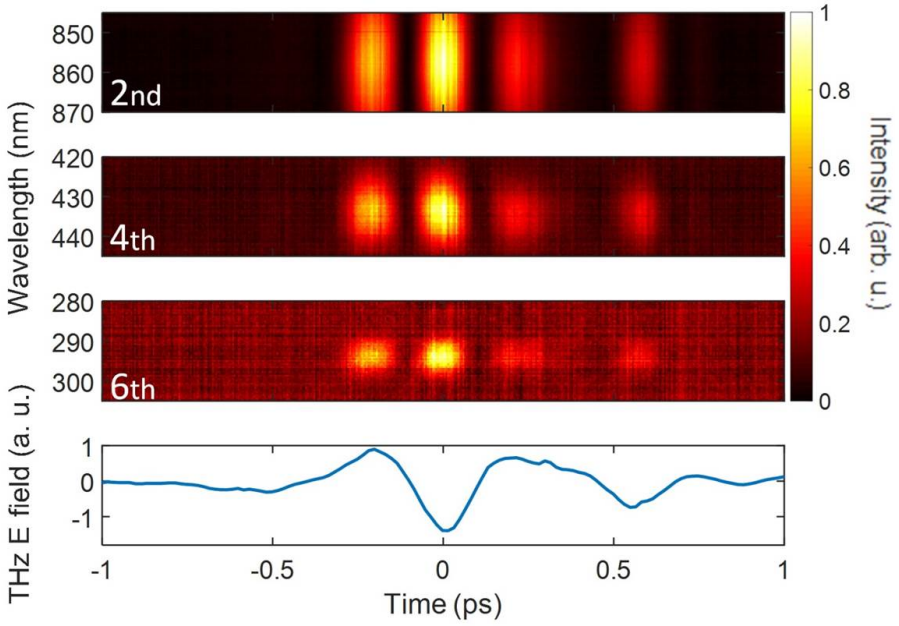

Fig. 5.15 The even-order harmonics (2nd, 4th, and 6th) spectra from silicon versus time delay of THz electric field (bottom panel) for parallel polarization configuration (IR ∥ THz). The sample's rotation angle around its normal is chosen to maximize the even harmonics [110].

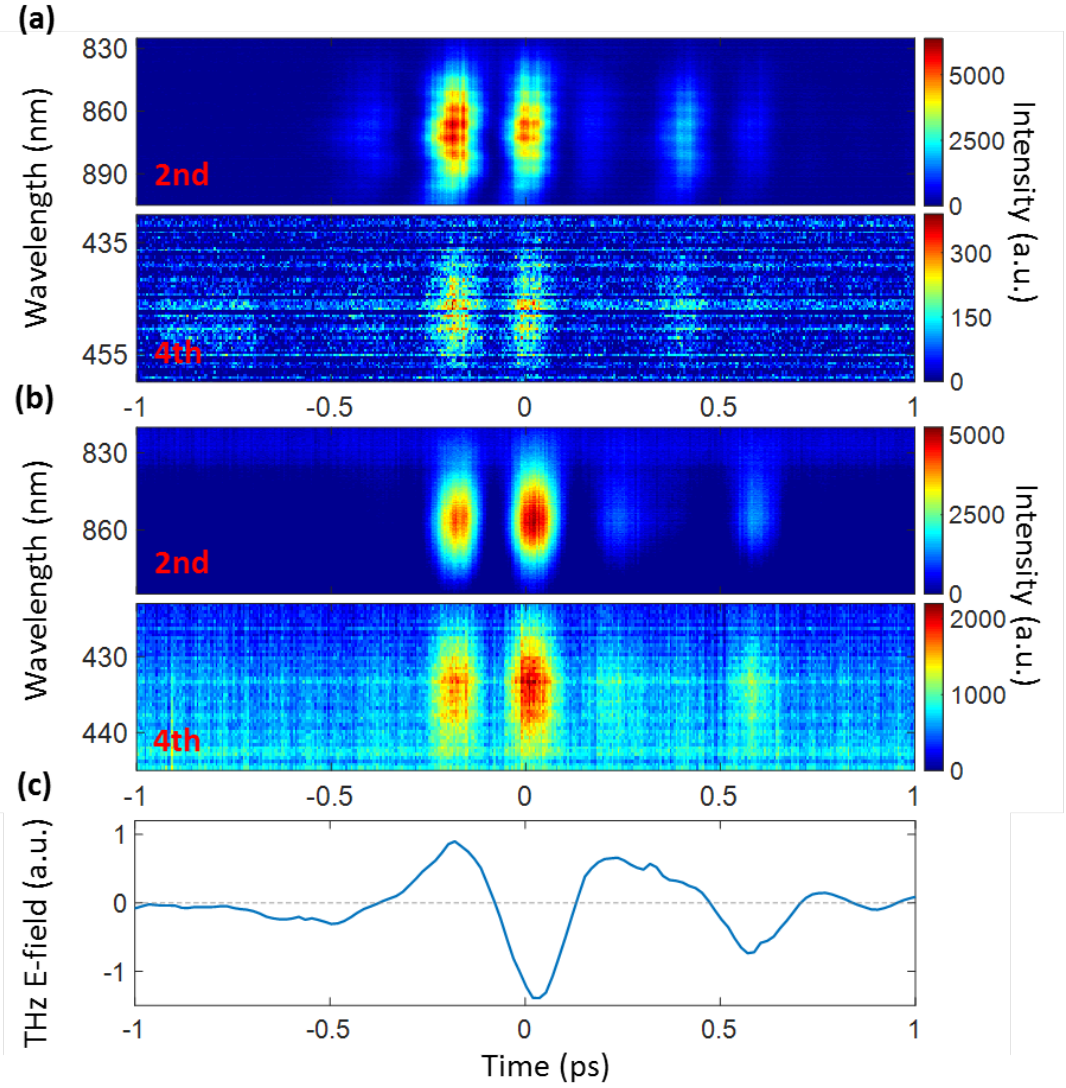

Fig. 5.16 The compare spectra of the even-order harmonics (2nd, 4th) from (a) diamond and (b) (100)-cut silicon versus time delay of (c) temporal profile of the THz electric field, for parallel polarization configuration (IR $\|$ THz). The samples' rotation angles around their normal are chosen to maximize the even harmonics.

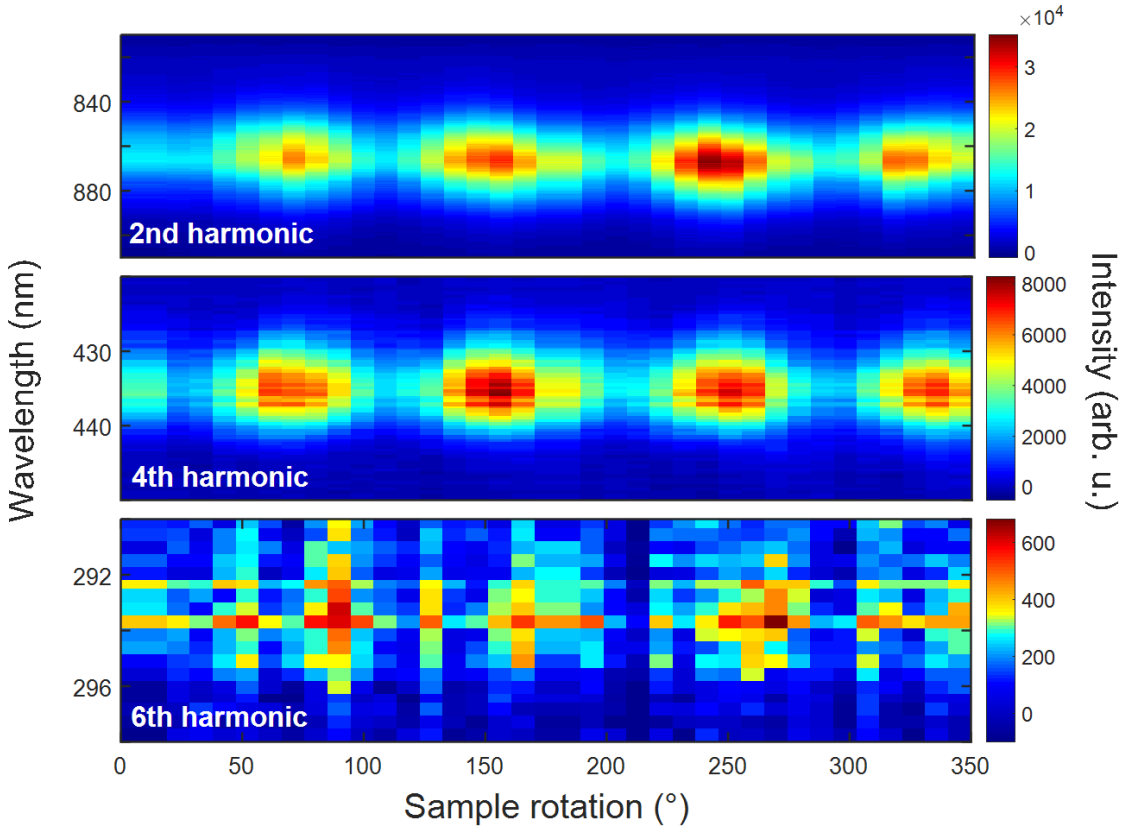

Fig. 5.17 Sample rotation dependence of the even-order harmonics in Si for parallel polarization configuration [110].

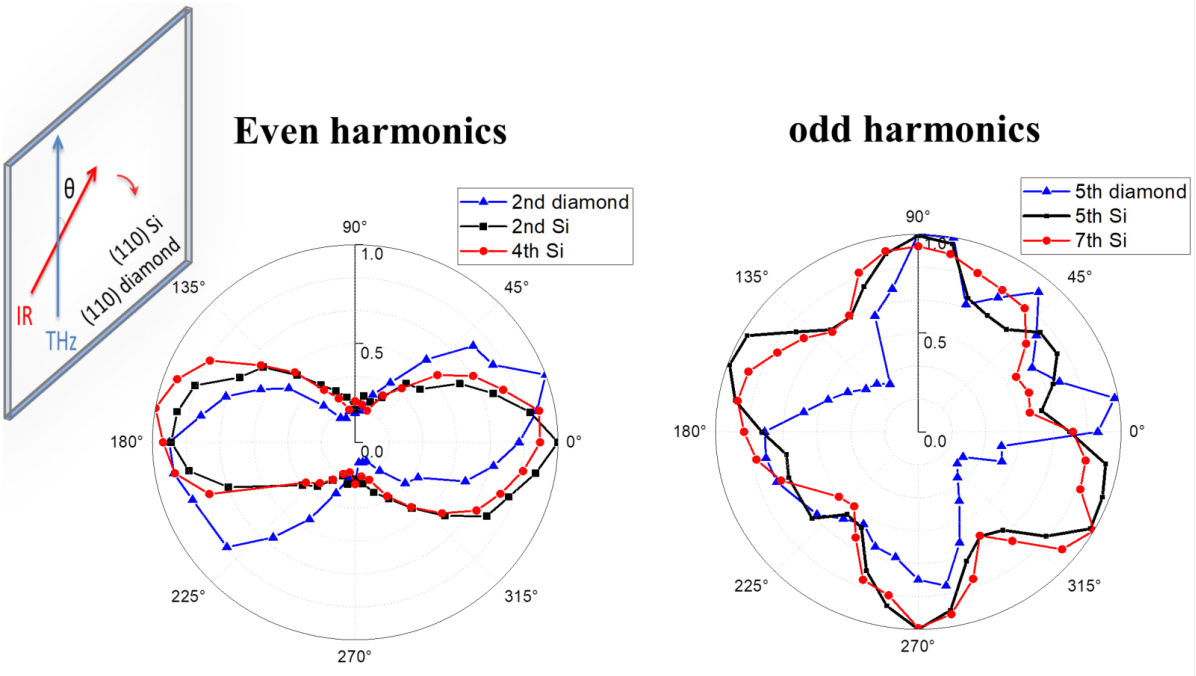

Fig. 5.18 Harmonic yields versus IR polarization angle. 0° corresponds to IR ∥THz, the samples' rotation angles around their normal are chosen to maximize the even harmonics. (a) Even harmonics (2nd, 4th in (110)-cut Si and 2nd in diamond) exhibiting a 2-fold symmetry; (b) odd harmonics (5th, 7th in (110)-cut Si and 5th in diamond).

5.8 Symmetry breaking in GaAs

A 500nm-thick (100)-cut GaAs crystal is also used for high harmonic generation to demonstrate the symmetry manipulation by intense THz beam. With a zinc blende crystal structure, GaAs has initial even-order susceptibility which means even-order harmonics can be generated without an additional electric field. When the THz field is applied, the initial polarization is distorted. The total second order polarization can be written as:

$$\mathrm{P}(2\omega) = \chi^{(2)}\mathrm{E}(\omega)\mathrm{E}(\omega) + \chi^{(3)}\mathrm{E}(\omega)\mathrm{E}(\omega)\mathrm{E}_{\mathrm{THz}} \tag{5.20}$$

where $\chi^{(2)}$ and $\chi^{(3)}$ are the second and third order response function, and $E(\omega)$ and E_THz are the electric field of the IR and THz pulses. The other even-order susceptibility can also be written similarly. Therefore, the overall even-order polarization is affected not only by the amplitude but also by the direction of the THz electric field, which means if the THz-induced polarization is in the same direction of the initial one, the polarization will be increased; otherwise, it will be decreased. This can be probed by even-order harmonic generation of IR pulses with different polarization. The trace of the generated 2nd and 4th harmonics along the THz electric field is recorded for a differently polarized IR pump, as shown in fig. 5.21a and b, respectively. There are even-order harmonics before the THz pulse arrives, which is because of the initial even-order susceptibility. Set the direction which has the largest initial even-order susceptibility as 0°. The polarization of the THz pulse is in 0° direction. During the rotation of the IR polarization, the generation of the even-order harmonics along THz electric field changes significantly. This is different from the case of Si because of the initial even-order susceptibility. From $-30°$ to 30°, the negative THz electric field offers more significant enhancement than the positive part. Fig. 5.21 b also shows that, when the IR polarization is 0° and 30°, the 4th harmonic generation is inhibited by the positive THz electric field but enhanced by the negative THz electric field. From 60° and 120°, the even-order harmonic generation is more enhanced by the positive part than the negative part of the THz electric field.

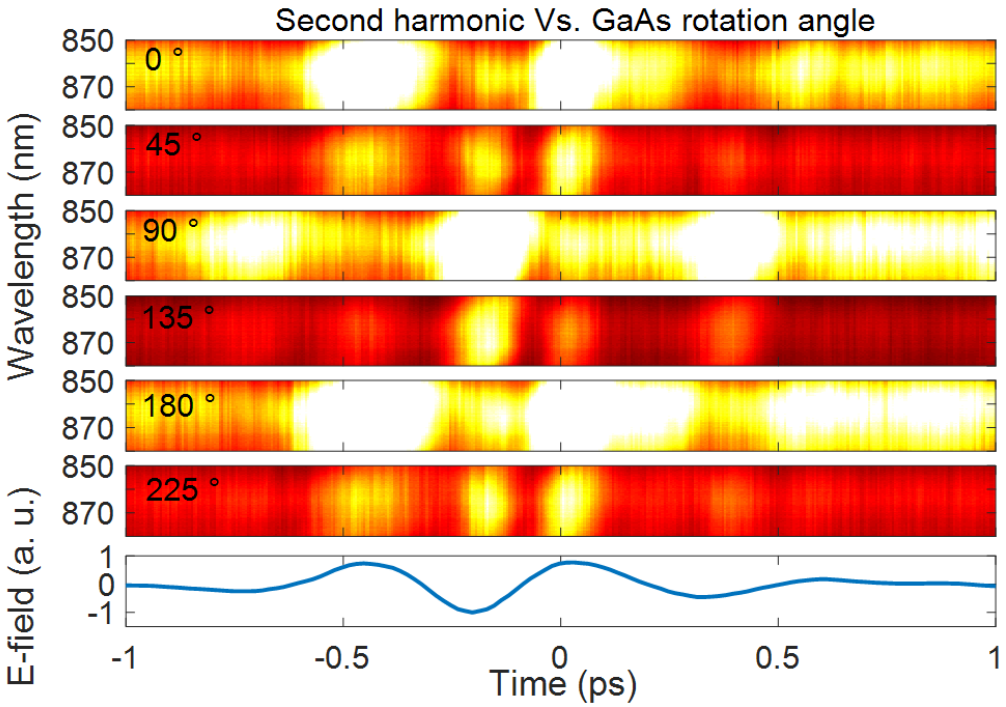

Fig. 5.19 Measured second harmonic generation with different crystal orientation in GaAs versus time delay of THz electric field.

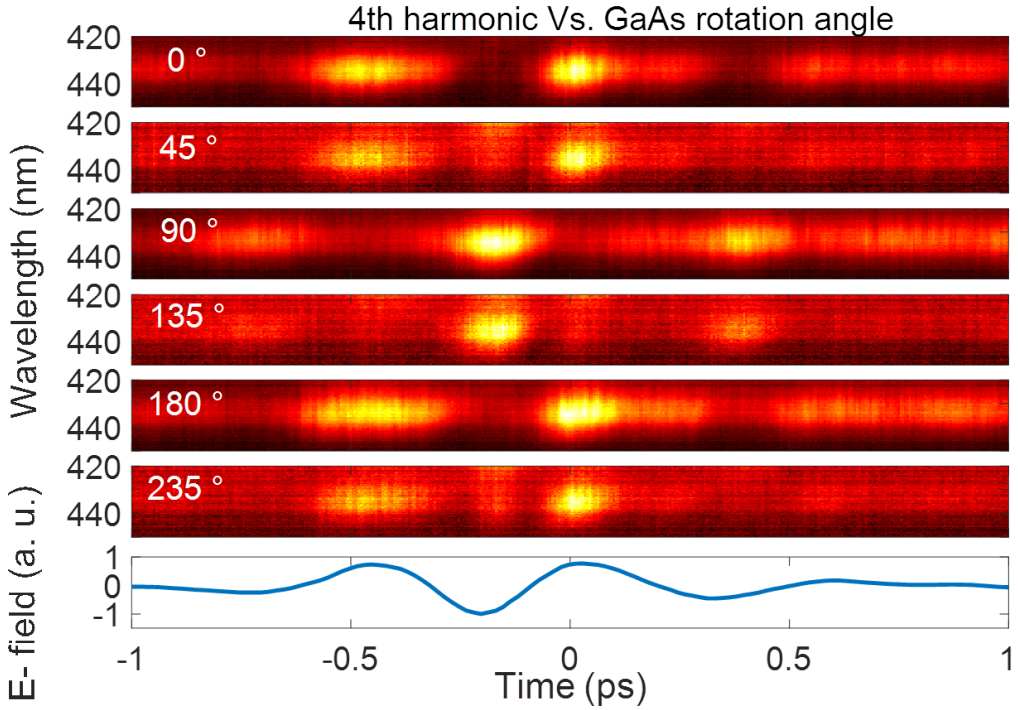

Fig. 5.20 Measured fourth harmonic generation with different crystal rotation angle from GaAs versus time delay of THz electric field. The intensity scale are normalized with the same level for all traces

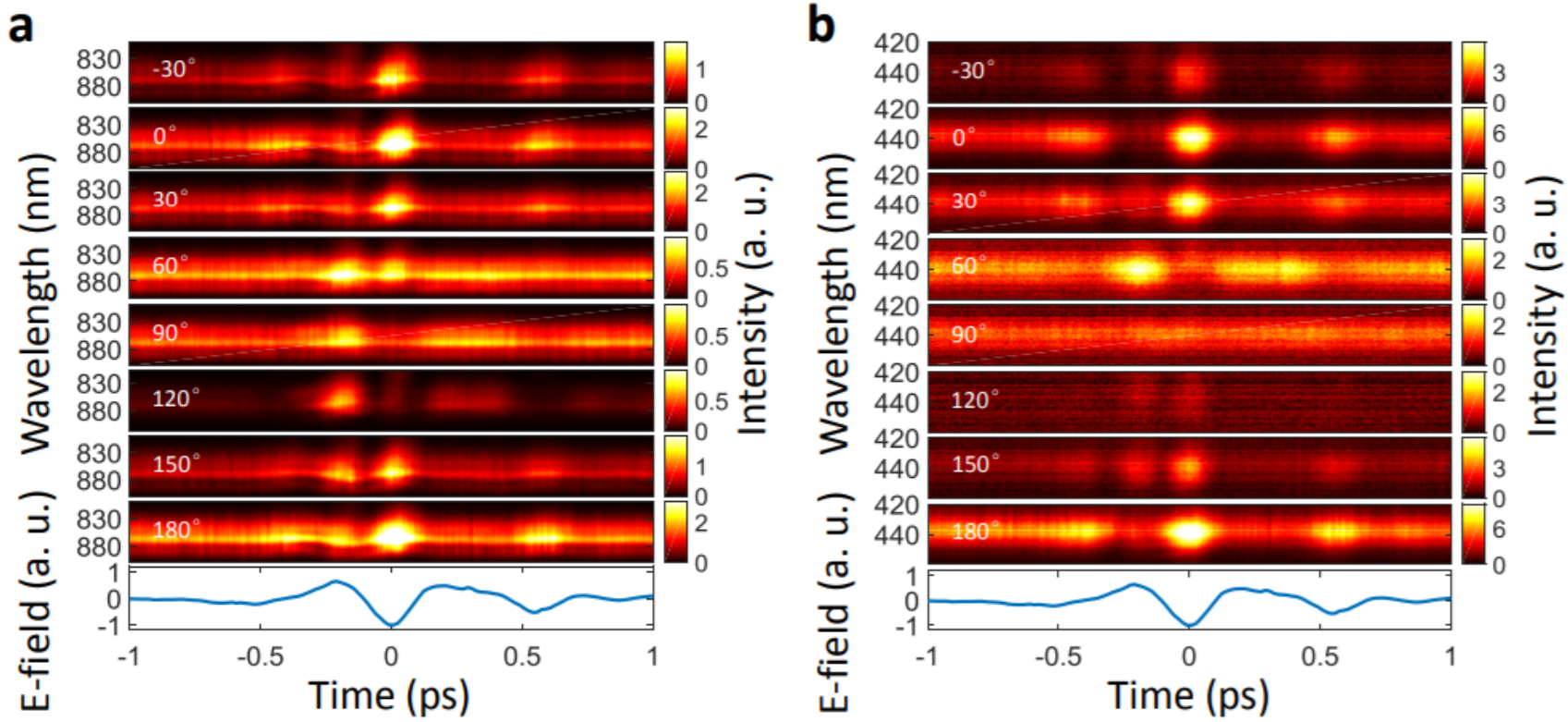

Fig. 5.21 Polarization dependence of even-order harmonic generation in GaAs. Measured 2nd and 4th harmonic generation of different IR polarization directions against THz polarization direction in GaAs versus time delay of THz E-field. The direction which has the largest initial even-order polarization is set as 0°. THz polarized along 0°.

Chapter 6

Solid-state HHG in the XUV

In this chapter, I will firstly introduce the motivation of setting up a compact XUV beamline for our experiment. Then I will go into engineering details of how to set up the compact XUV beamline. A gated XUV detection is introduced to improve the signal to noise ratio and some first results of XUV signals from MgO and NiO are shown. The XUV emission from MgO shows HHG features, while the XUV emission from NiO does not behave as expected. So more experiments and theoretical calculations are needed to understand this XUV emission mechanism and to create nonperturbative higher-order harmonics from NiO. These results are based on joint work with Nicolai Klemke.

6.1 Motivation for buliding a XUV beamline

Magnetic materials are at the heart of the field of spintronics. Below given temperature, the spin of the electrons for these materials aligns in regular patterns with neighboring spins. For Ferromagnetic and antiferromagnetic materials, this temperature is called the Curie temperature. It was recognized for a long time that this preferred ordering of the spin, which determines the electronic and optical properties of these materials, is a direct consequence of the correlation between electrons. Understanding these materials' behavior such as HHG features when driven by intense infrared light pulses will thus deepen our understanding of how electron correlation effects build up on the attosecond timescale. Moreover, for the microscopic mechanisms of solid-state HHG [78] introduced in section 5.1 is under the approximation that the band structure of a solid stays frozen while the electronic occupations of the bands change during the light matter interaction [116] . This frozen-band-structure approximation, which seems to work well for HHG in solids assuming independent electrons such as bulk silicon [103] and MgO [117], could be invalid in correlated materials such as transition metal oxides. So the study of HHG from correlated materials might reveal new interesting features contributed by

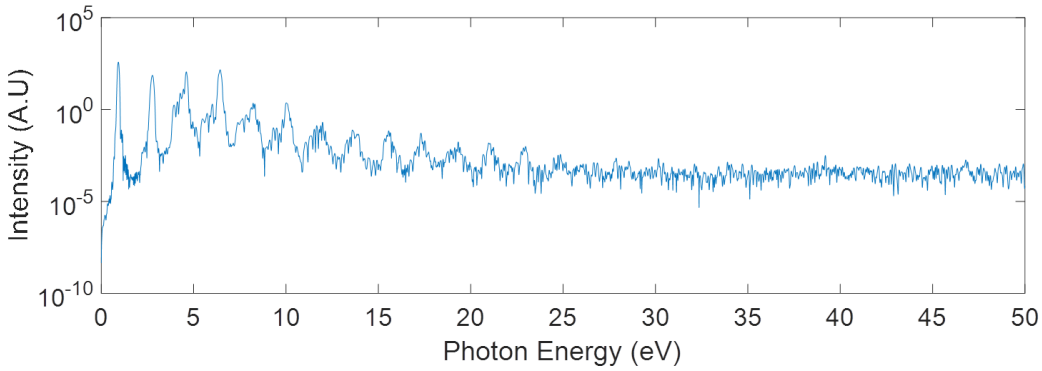

Fig. 6.1 The simulated spectrum of the HHG in NiO from Nicolas Tancogne-Dejean. Note that The cutoff of the HHG has extended into XUV regime.

the correlation effects. Our collaborator Nicolas Tancogne-Dejean also predicts some novel HHG behavior in the charge-transfer insulator NiO using a time-dependent density-functional theory plus self-consistent Hubbard U method [116]. The simulation results from him indicated that the cutoff of HHG in NiO extends to the XUV region. (shown in Fig. 6.1).

Earlier research on HHG from NiO in the air was done by Eliza Casandruc in our group. For these low-order harmonics results from NiO, she measured the intensity dependence of the lower order harmonics HH5 and HH7 in Fig. 6.2. As the driving energies increase, they deviate from the normal harmonic scaling behavior, especially for HH7. For the highest driving energies, they enter the nonperturbative regime (deviation from the I^7 scaling).

To further study the behavior of higher harmonic orders from NiO or other solids, it is vital to set up an XUV beamline in the lab, as XUV photons can not propagate in the air because of the high absorption in the air. The design and implementation of this XUV beamline would be discussed in detail in the following section.

6.2 Experimental setup

The experimental setup scheme of solid HHG vacuum XUV beamline is shown in Fig. 6.3. This vacuum system consists of two custom-designed vacuum chambers, in which the solid samples and the XUV spectrometer are housed. The infrared driver pulses are produced by the home-built optical parametric amplifier (OPA) introduced in Chapter 3. After transmitting through the input window of the first chamber, we focus the signal of OPA with a 45-cm-lens onto the solid sample (a free-standing 50-μm-thick NiO crystal or a free-standing 50-μm-thick MgO crystal), which mounted on a motorized rotation stage, and then measure the generated XUV photons in a transmission geometry via the XUV spectrometer or a microchannel plate(MCP) detector.

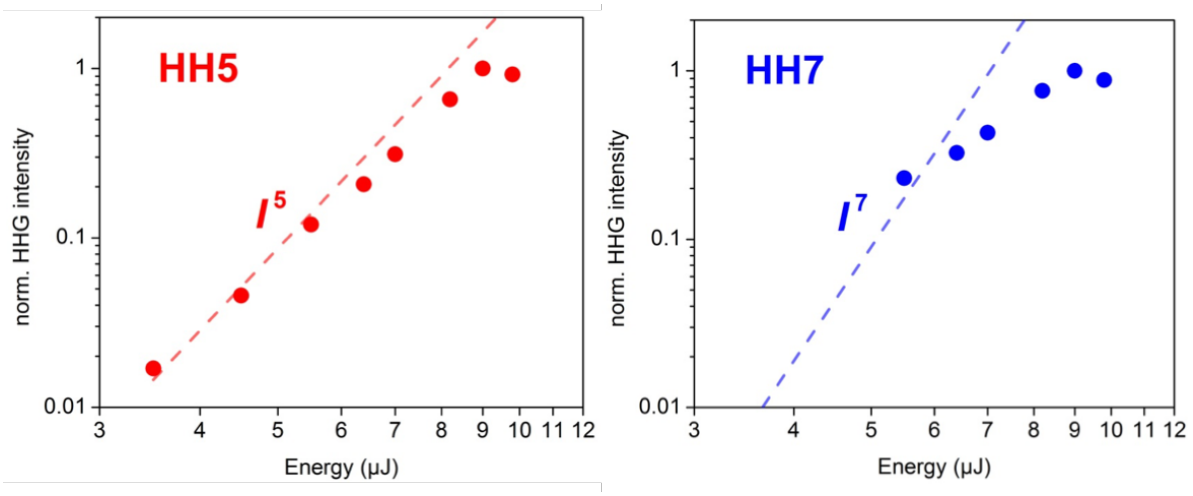

Fig. 6.2 Intensity scaling of harmonic yields HH5 and HH7 from 50-μm NiO in the visible spectral region: for the highest driving intensities, the harmonic signals exhibit clear deviations from a perturbative power law (indicated by the green lines). the harmonics HH5 and HH7 were generated by 120-fs, 2.1-μm pulses and detected by an Ocean Optics HR4000 spectrometer.

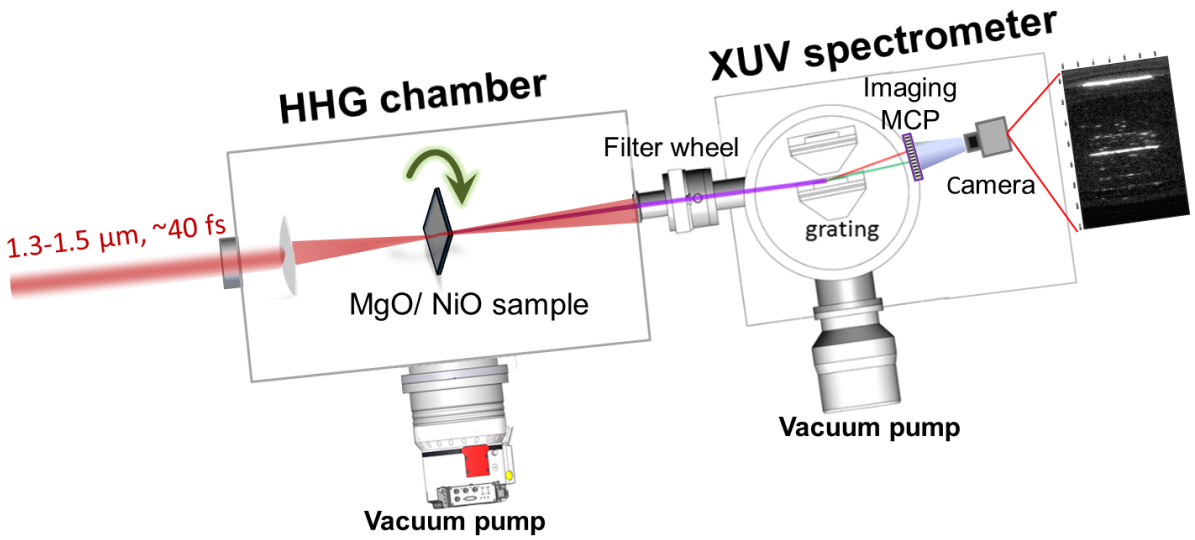

Fig. 6.3 Schematic of a vacuum XUV beamline setup. The input IR pulse from the OPA passes through the fused-silica-entrance of the vacuum chamber and is focused onto the solid samples (MgO or NiO) by a 45-cm-lens. The XUV generated from the sample then propagates through the XUV spectrometer and hit the microchannel plate (MCP) detector.

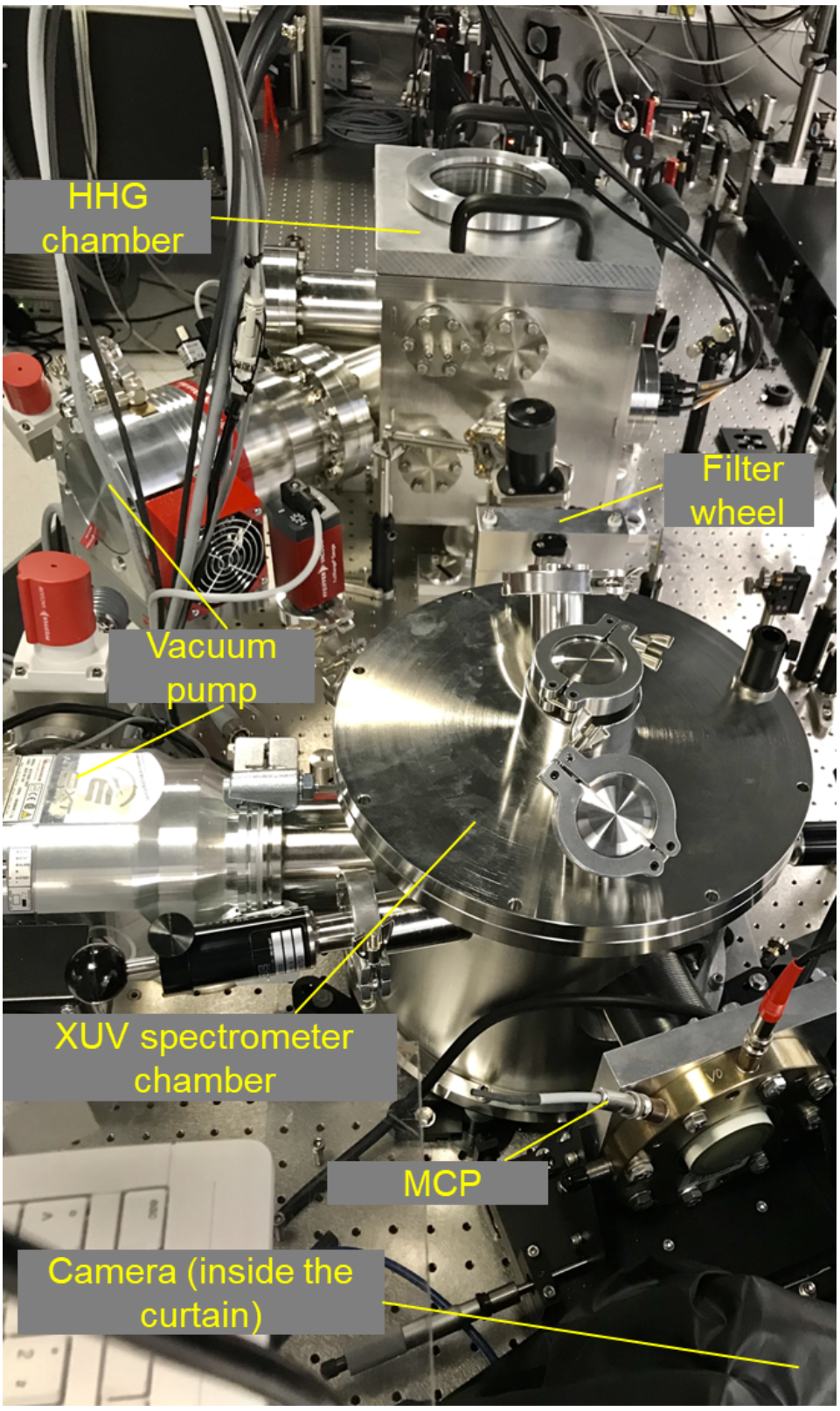

Fig. 6.4 Photo of vacuum XUV beamline setup in the lab.

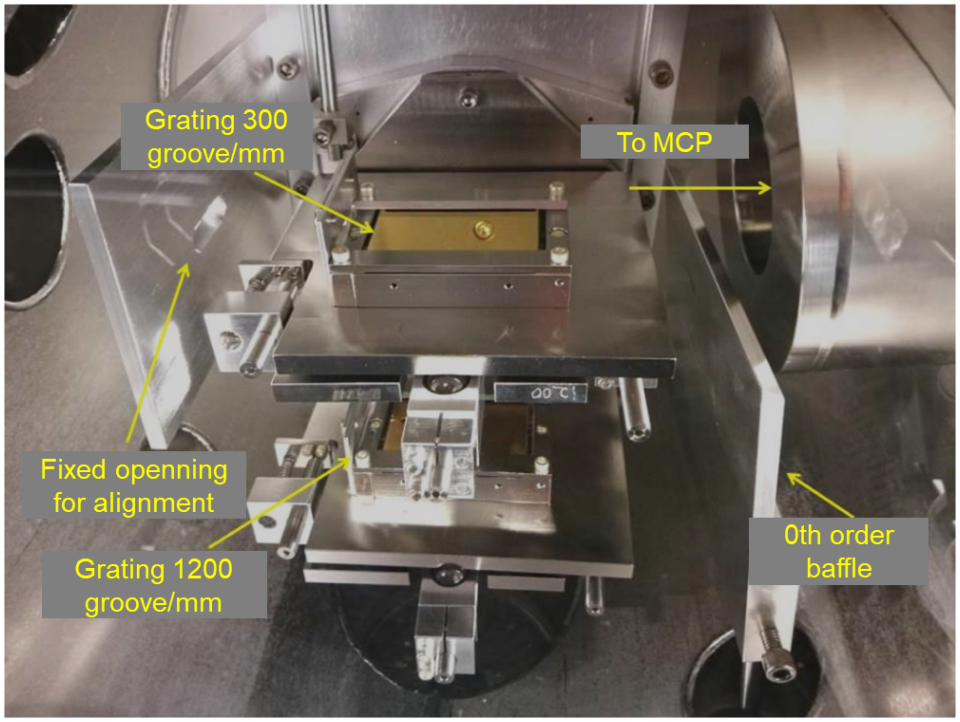

Fig. 6.5 Photo of the McPherson 251MX XUV spectrometer gratings.

There is a filter wheel connecting the two vacuum chambers, which contains several thin metallic filters. For our case, a 50-nm-In-filter and a 50-nm-Al-filter are mounted for the calibration of the XUV energy in 15-17eV, as a narrow high transmission overlap in this energy range for both filters is a good photon energy calibration reference for calibrating the peak energy of the XUV (shown in Fig. 6.9). After transmitting the filter wheel, the suppressed driver pulses and the XUV photons propagate into the XUV spectrometer chamber, where the XUV harmonics can be spectrally resolved by a McPherson soft-X-ray/XUV flat-field spectrograph (Model 251MX) equipped with 300 grooves/mm flat-field XUV grating for 20-80 nm (62-15.5 eV) and a MgF_2-coated multi-channel plate (MCP). Specifically, the XUV go through an adjustable slit and a fixed opening before being dispersed by the grating and then are detected by the imaging MCP. A web-camera (acA5472-17uc, Basler camera) is used to capture the XUV spectra imaged on the phosphor screen of the MCP.

6.2.1 Gated detection of XUV spectra

In the XUV detection, the detected MCP signals inevitably contain the background noise from the driver pulses that would overwhelm the weak XUV signals. To solve this problem, a gated detection method is used in our solid-state XUV beamline. The gating setup (shown in Fig. 6.6) includes a delay generator, a high voltage gating unit and the two-MCP stack. The 3-kHz TTL

signal from the laser-trigger-pulses goes through the delay generator and feeds the high voltage switch to modulate the high voltage output into a gated-high-voltage-pulse (the pulse shape is shown in Fig. 6.6). The maximum voltage that can be applied to the two-MCP stack is set to 2400 V, which is enough for signal detection. Then, the delay should be carefully tuned to synchronize with the coming XUV signal and the high voltage pulse duration is set to 70 ns (the minimal value for MCP to work properly). The XUV signal patterns from NiO with and without gating detection are shown in Fig. 6.7. Here, the bright line in the left edge of both phosphor screens shows the zero order of driving laser for reference. The spotted lines in the same row of the zero order on the phosphor screen are all detected XUV photons and their pattern is stable. The random scattering spots in the upper image are all noises. Obviously, the gating suppresses most of the random scattering spots.

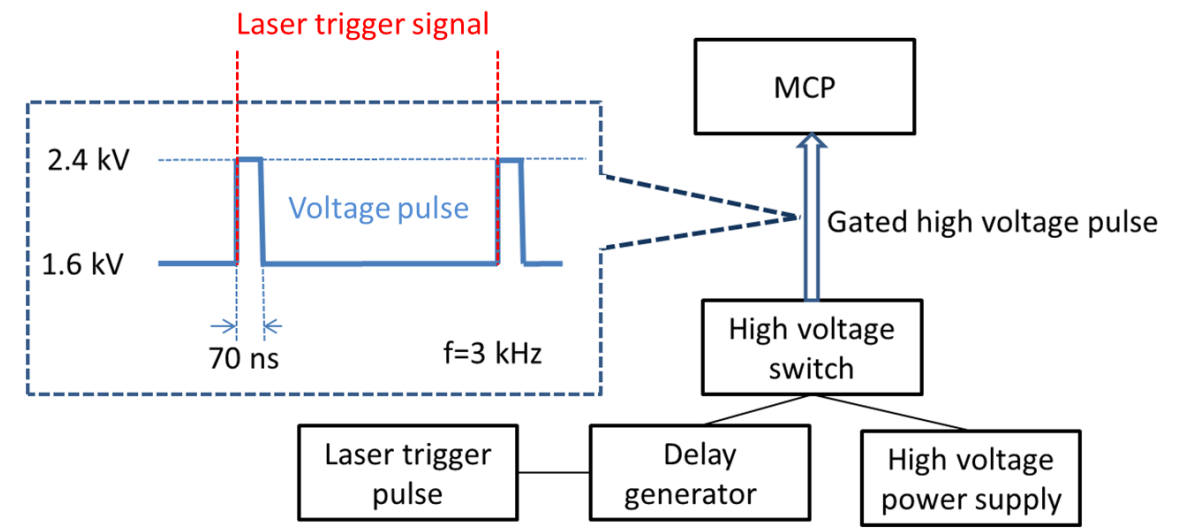

Fig. 6.6 The schematic of the gating setup for MCP

6.3 Experimental results

6.3.1 Calibration of multi-channel plate-based spectrometer

To measure the XUV harmonics with the XUV spectrometer, the wavelength calibration is an essential but not straightforward issue. While a usual compact spectrometer used in the air is easy to find a wavelength standard (e.g. a common fluorescent lamps which has a set of spectral lines from mercury), sources in the XUV range, such as an expensive gas discharge source or a synchrotron, are not viable in our experimental conditions. To solve this problem, we take

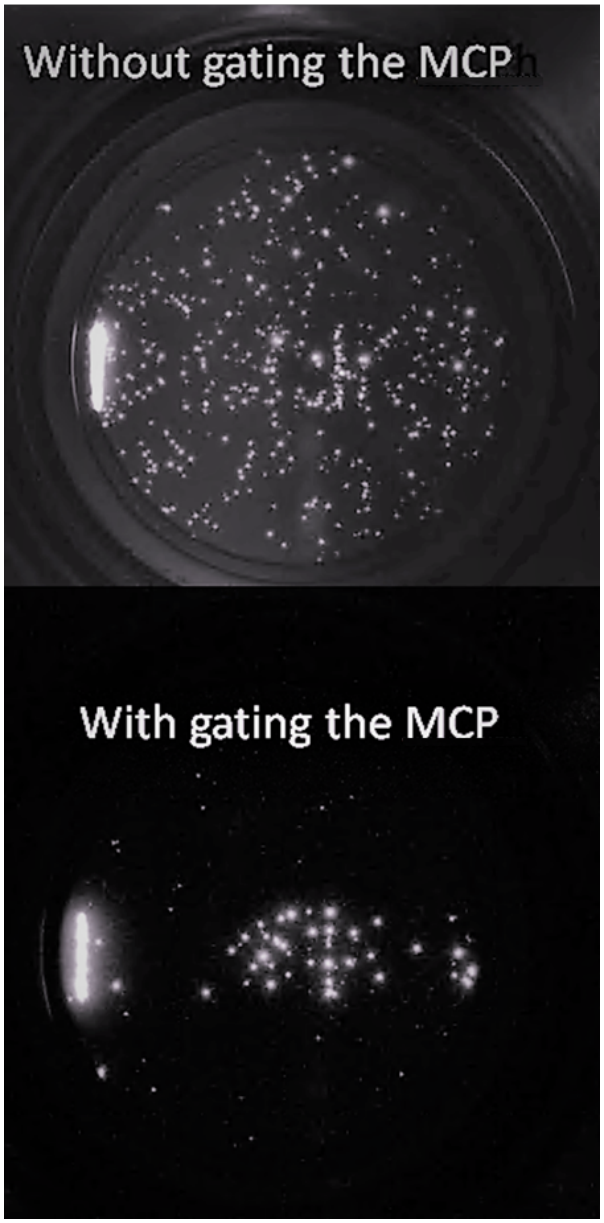

Fig. 6.7 The XUV signal patterns from NiO on MCP phosphor screen with and without gated detection. The bright line in the left edge of both phosphor screens shows the zero order of driven laser for reference. The spotted lines in the same row of the zero order on the phosphor screen are all detected XUV photons and their pattern is stable. The random scattering spots in the upper image are all noises. Obviously, with gating detection, most of the noises can be depressed.

advantage of both the absorption edges of metallic thin filters and the photon energies of HHG spectrum peaks of MgO single crystal.

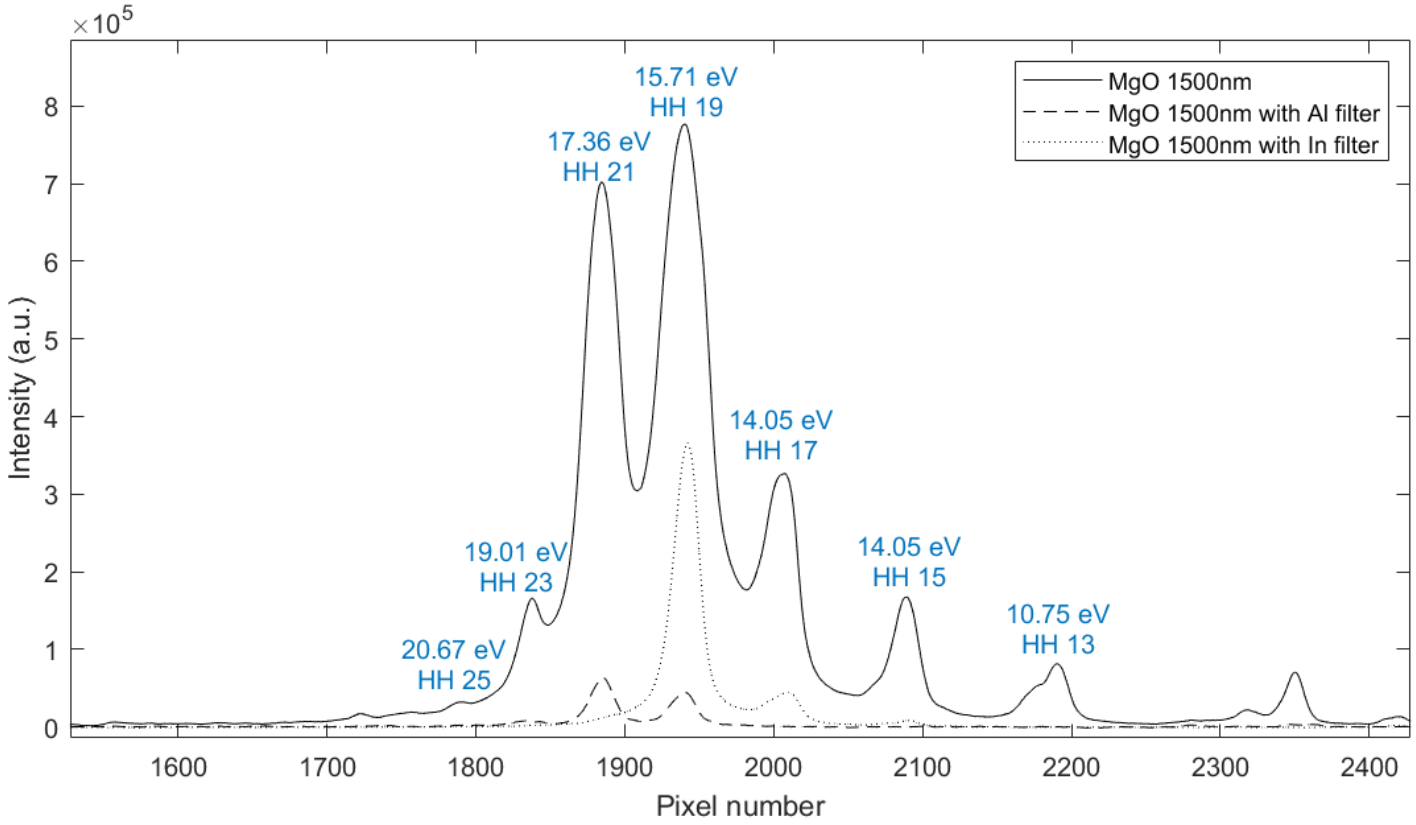

Fig. 6.8 The uncalibrated HHG harmonics spectra from MgO. Here the X axis is the pixel number of raw data. The seven harmonic peaks as well as their photon energies are labeled here for calibration of the photon energy axis.

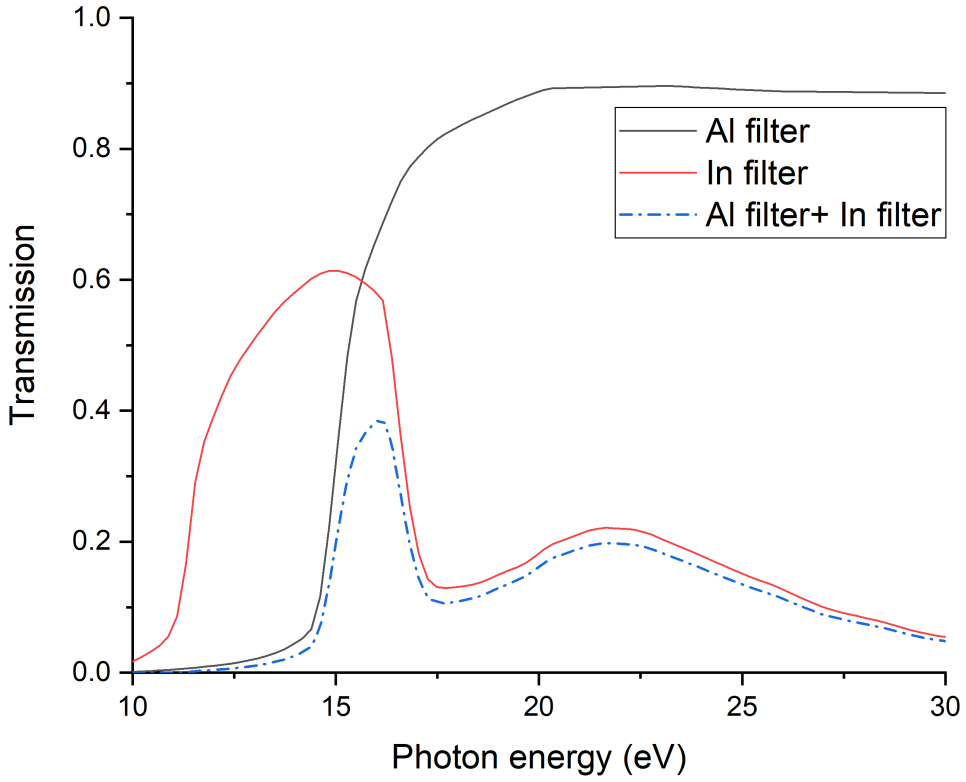

Fig. 6.9 XUV transmission curves of 50 nm Al filter, 50 nm In filter and combined (Al+In) filter transmission.

The uncalibrated raw-data of XUV harmonic spectra from MgO single crystal are shown in Fig. 6.8. The resulting spectra measured without filter, with Al filter and with In filter are plotted as a solid line, dash line, and dotted line, respectively.

To calibrate the XUV spectrometer, photon energy of each pixel in the 15-17eV XUV transmission curves of 50 nm Al filter and In filter are shown in Fig. 6.9.

Since the harmonic peak structure of the HHG spectrum consists of spectral spikes locating at odd harmonic order of the fundamental frequency, the energy gap value between neighbouring peaks would be twice the photon energy of the driven pulse. For our uncalibrated HHG raw-data in Fig. 6.8, this energy gap value is 1.65 eV and harmonic spectra after In or Al thin filter has only one common harmonic peak. Compared to the transmission curves of the Al and In filter in Fig. 6.9, this peak could only be 19th order harmonic and therefore the photon energy of this peak is 15.71 eV. After anchoring the pixel position of the 19th harmonic peak in the raw data, other high harmonic orders can easily be determined. The photon energy values of odd-harmonic peaks are labeled in Fig. 6.8 and all of them are calculated from their harmonic

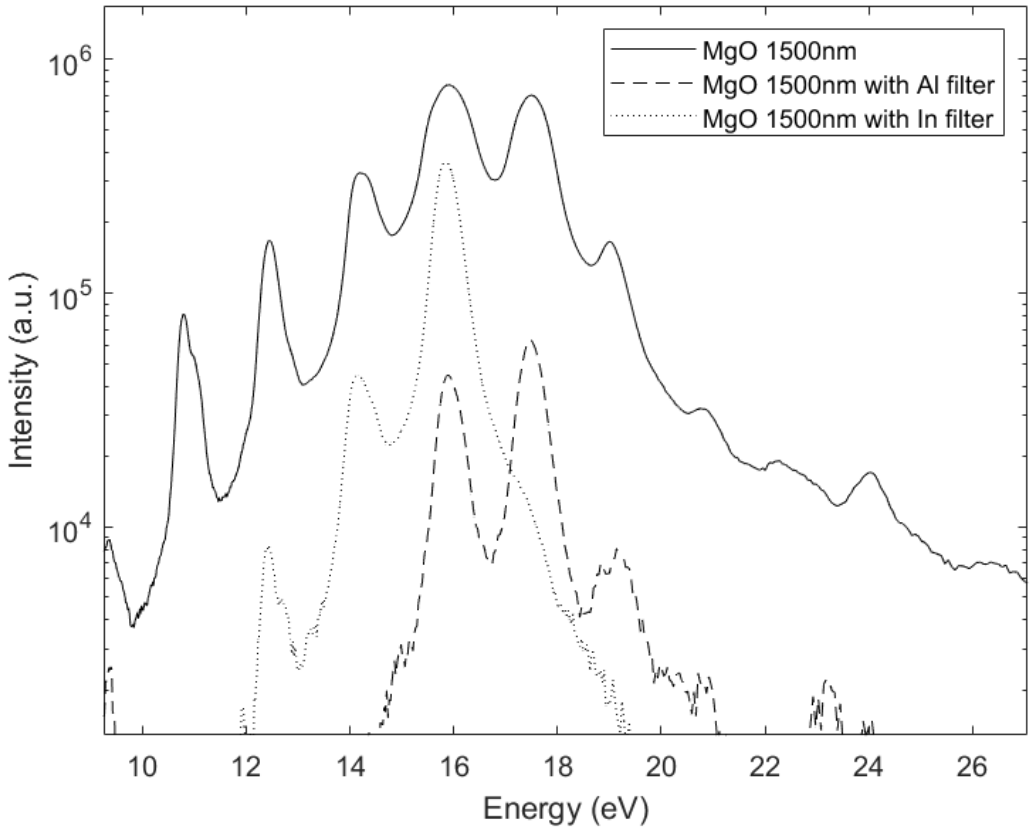

Fig. 6.10 The HHG harmonics spectra from MgO. The HHG of MgO without filter, with Al filter and with In filter are plotted as a black solid line, black dash line, and black dotted line, respectively.

order times the photon energy of the driving OPA pulse. Fitting these 7 data values to the polynomial function to get the wavelength calibration coefficients, the wavelength and photon energy associated with each pixel on pixel coordinate could be deduced. With this, we can convert the pixel number axis into photon energy axis.

6.3.2 HHG from MgO

Fig. 6.10 shows the XUV harmonic spectra from MgO single crystal after the calibration of the energy. The HHG of MgO without filter, with Al filter and with In filter are plotted as a black solid line, black dash line and black dotted line, respectively.

Fig. 6.11 shows XUV spectra from MgO single crystal with a different driven laser photon wavelength of 1500nm, 1450nm and 1300nm, respectively. In each spectrum curve, the peak to peak energy gaps stay the same and grow wider as the driven laser photon energies increase, which is a clear HHG feature. Moreover, when changing the drive wavelength, the XUV

harmonic peaks from MgO single crystal display a shift according to the harmonic order times the fundamental photon energy. This is another signature of the HHG spectra. The laser intensity on the sample is ~ 7 TW/cm^2, which is already near the damage threshold of the samples.

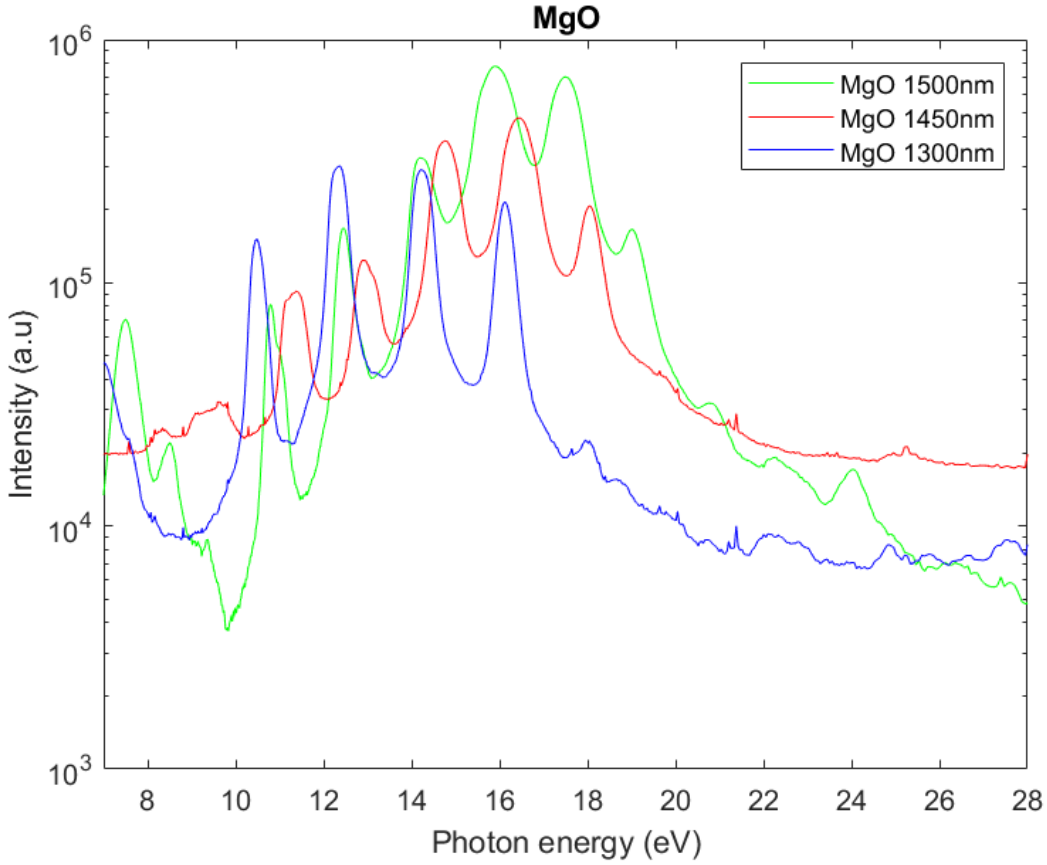

Fig. 6.11 The wavelength dependence of nonperturbative HHG spectra in MgO. In each spectrum curve, the peak to peak energy gaps stay the same and grow wider as the driven laser photon energies increases, which is a clear HHG feature. Moreover, when changing the drive wavelength, the XUV harmonic peaks from MgO single crystal display a shift according to the harmonic order times the fundamental photon energy. This is another signature of HHG spectra.

6.3.3 Crystal rotation dependence of HHG in MgO

To verify the XUV emission of MgO is an HHG signal as well as to demonstrate the ability of our vacuum HHG XUV beamline, we also perform the measurement of crystal angle rotation dependence of nonperturbative high-harmonic emission in MgO (shown in Fig. 6.12). The four-fold angular dependence of the XUV spectra is compatible with the HHG symmetry feature in MgO single crystal.

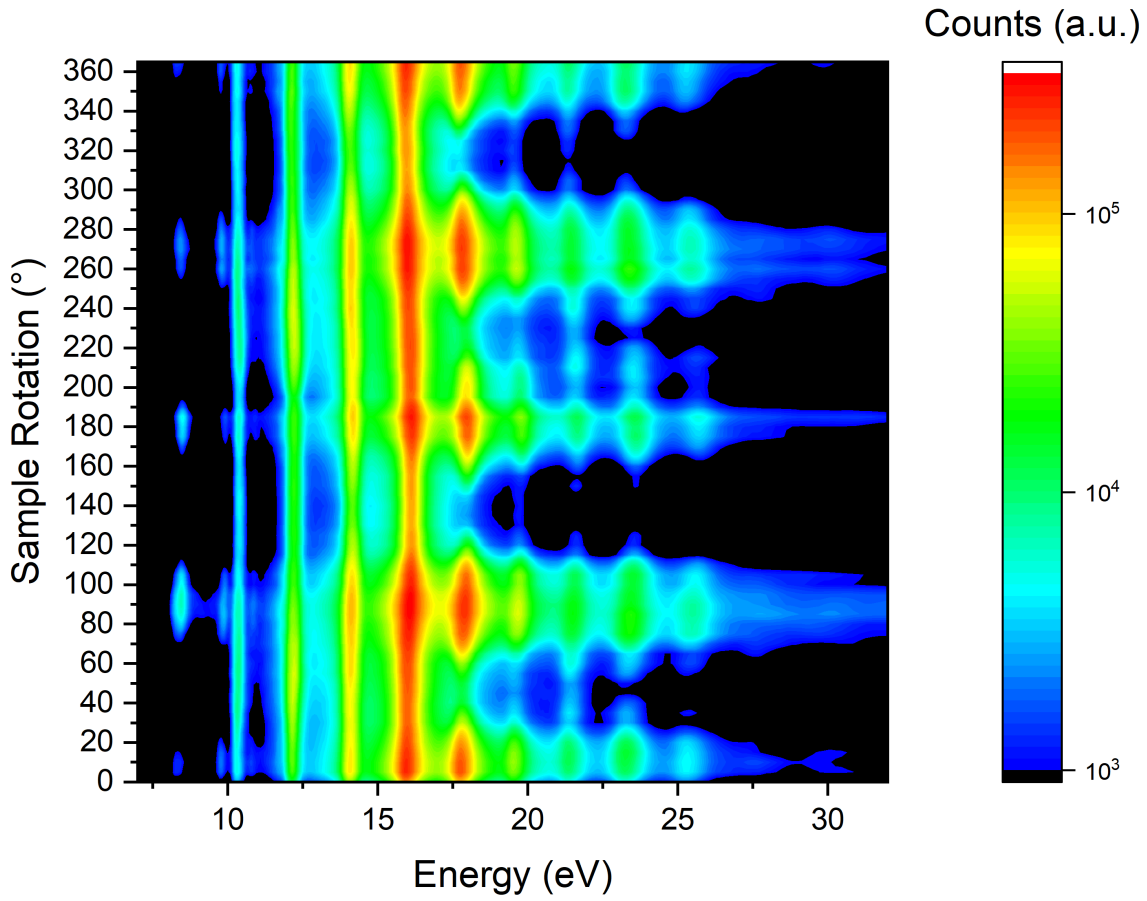

Fig. 6.12 HHG dependence on MgO sample rotation driven by 1300nm OPA pulses. The four-fold angular dependence of the XUV spectra is compatible with the HHG symmetry feature in MgO.

6.3.4 XUV emission from NiO

The XUV emission spectrum from NiO together with the HHG spectra from MgO are shown in Fig. 6.13 for comparison.

The wavelength dependence of XUV spectra in NiO is shown in Fig. 6.14. Compared with MgO, the XUV emission peaks from NiO do not shift when changing the drive wavelength. This is against the feature of HHG signal. Therefore, the observed signal can not be from an HHG process. The enegry scan of XUV spectra in NiO is shown in Fig. 6.15. Currently, the mechanism of this XUV emission photons is not clear.

Unfortunately, in these preliminary experiments - the XUV emission from NiO did not behave as expected, as there is no clear harmonic structure observed. More experiments and

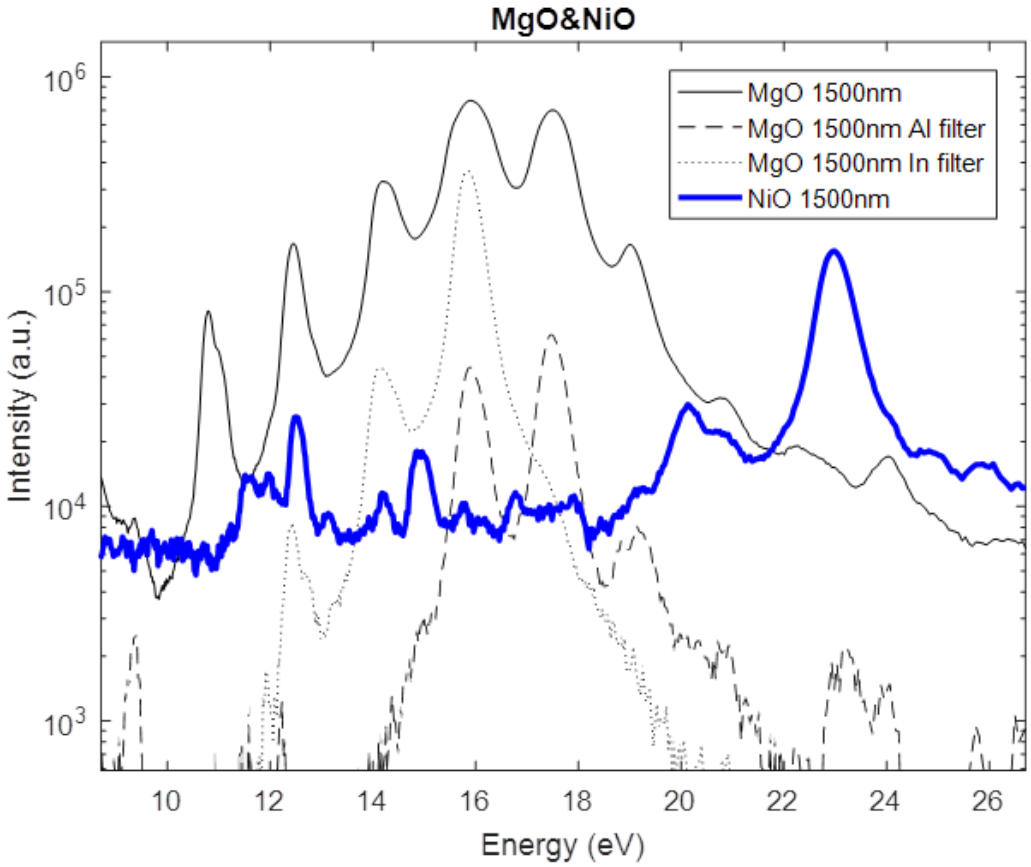

Fig. 6.13 XUV emission spectrum from NiO together with the HHG harmonics spectra from MgO for comparison.

theoretical calculations are needed to understand the XUV emission mechanism and to really create nonperturbative higher-order harmonics from NiO.

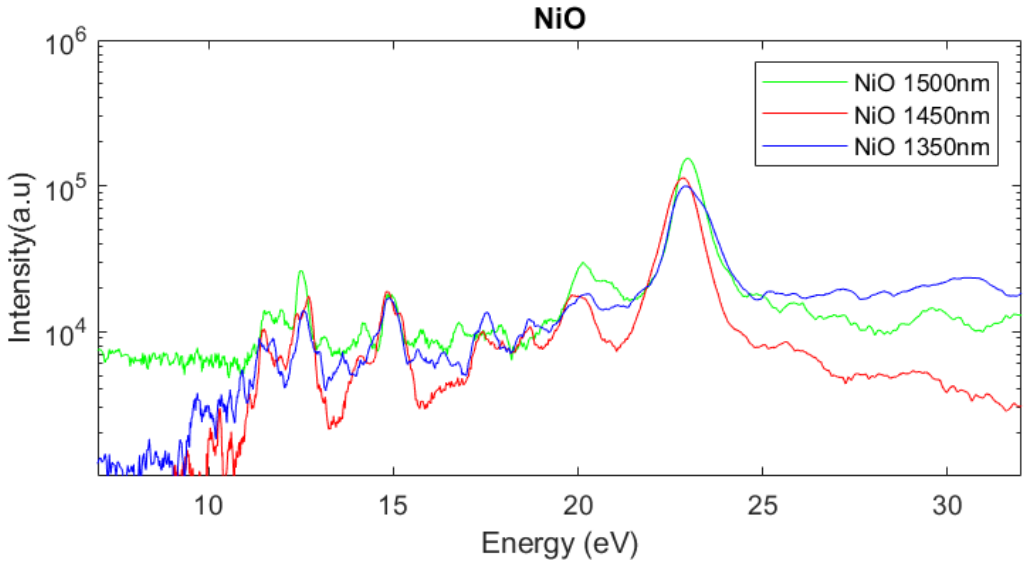

Fig. 6.14 The wavelength dependence of XUV spectra in NiO. Compared with MgO, the XUV emission peaks from NiO do not shift when changing the drive wavelength. This is against the feature of HHG signal. Currently, the mechanism of this XUV emission photons is not clear.

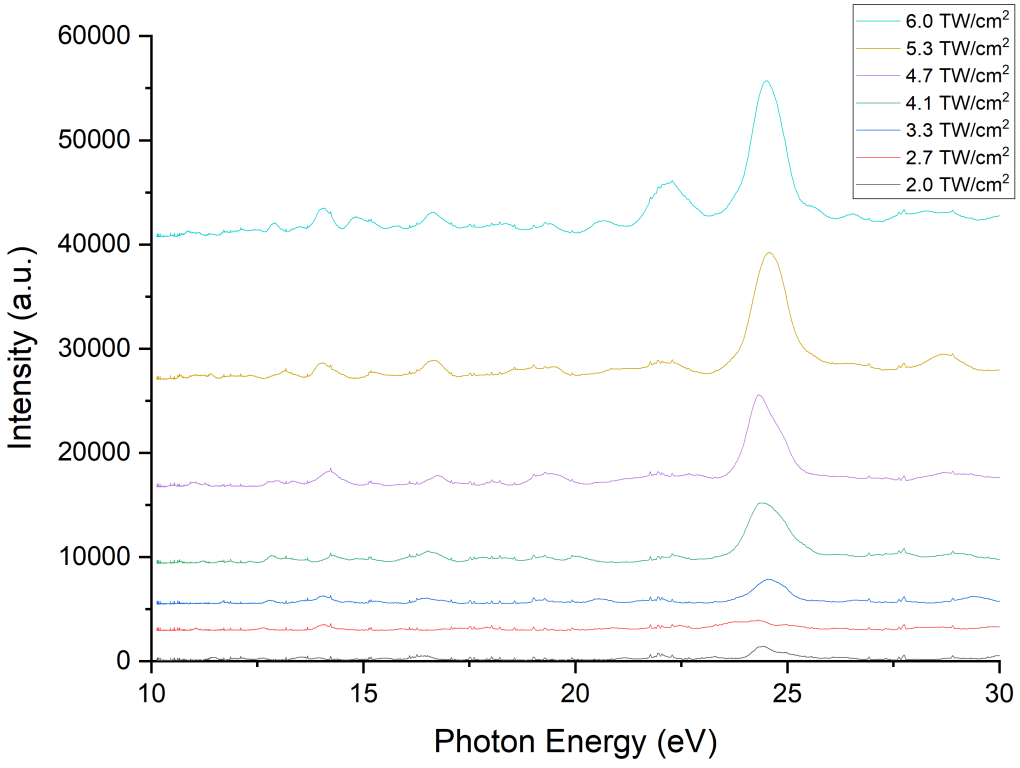

Fig. 6.15 The enegry scan of XUV spectra in NiO.

References

[1] Janos Hebling, Gabor Almasi, Ida Kozma, and Jurgen Kuhl. Velocity matching by pulse front tilting for large area THz-pulse generation. *Optics express*, 10(21):1161–1166, 2002.

[2] Chen Ning Yang. Thematic melodies of twentieth century theoretical physics: Quantization, symmetry and phase factor. In *Selected Papers II: With Commentaries*. 2013.

[3] P. W. Anderson. More Is Different. *Science*, 1972.

[4] Robert W Boyd. Nonlinear optics. page 316, 2010.

[5] Wenqian Ronny Huang. *All-Optical Electron Acceleration with Ultrafast THz Pulses*. PhD thesis, Massachusetts Institute of Technology, 2017.

[6] Phillipe Piot. PHYS 630. *Lecture Notes*, 2016.

[7] Clemens Tobias Friedrich Jakubeit. *High Harmonic Generation using a 2 µm OPCPA*. PhD thesis, Ludwig–Maximilians–Universitaet, 2019.

[8] Chuang Li, Ding Wang, Liwei Song, Jun Liu, Peng Liu, Canhua Xu, Yuxin Leng, Ruxin Li, and Zhizhan Xu. Generation of carrier-envelope phase stabilized intense 15 cycle pulses at 175 μm. *Optics Express*, 19(7):6783, 2011.

[9] Daniel J. Kane and Rick Trebino. Characterization of Arbitrary Femtosecond Pulses Using Frequency-Resolved Optical Gating. *IEEE Journal of Quantum Electronics*, 1993.

[10] Rick Trebino and Daniel J. Kane. Using phase retrieval to measure the intensity and phase of ultrashort pulses: frequency-resolved optical gating. *Journal of the Optical Society of America A*, 1993.

[11] Rick Trebino. *Frequency-Resolved Optical Gating: The Measurement of Ultrashort Laser Pulses*. 2000.

[12] Oliver Graydon. Terahertz: Entering applications. *Nature.com Blogs*, page May 21, 2018.

[13] Wikipedia contributors. Terahertz radiation, 2019.

[14] X. C. Zhang and Jingzhou Xu. *Introduction to THz wave photonics*. 2010.

[15] D. H. Auston, K. P. Cheung, J. A. Valdmanis, and D. A. Kleinman. Cherenkov radiation from femtosecond optical pulses in electro-optic media. *Physical Review Letters*, 1984.

[16] Ch Fattinger and D. Grischkowsky. Point source terahertz optics. *Applied Physics Letters*, 1988.

[17] S. S. Dhillon, M. S. Vitiello, E. H. Linfield, A. G. Davies, Matthias C. Hoffmann, John Booske, Claudio Paoloni, M. Gensch, P. Weightman, G. P. Williams, E. Castro-Camus, D. R.S. Cumming, F. Simoens, I. Escorcia-Carranza, J. Grant, Stepan Lucyszyn, Makoto Kuwata-Gonokami, Kuniaki Konishi, Martin Koch, Charles A. Schmuttenmaer, Tyler L. Cocker, Rupert Huber, A. G. Markelz, Z. D. Taylor, Vincent P. Wallace, J. Axel Zeitler, Juraj Sibik, Timothy M. Korter, B. Ellison, S. Rea, P. Goldsmith, Ken B. Cooper, Roger Appleby, D. Pardo, P. G. Huggard, V. Krozer, Haymen Shams, Martyn Fice, Cyril Renaud, Alwyn Seeds, Andreas Stöhr, Mira Naftaly, Nick Ridler, Roland Clarke, John E. Cunningham, and Michael B. Johnston. The 2017 terahertz science and technology roadmap. *Journal of Physics D: Applied Physics*, 50(4), 2017.

[18] H. A. Hafez, X. Chai, A. Ibrahim, S. Mondal, D. Férachou, X. Ropagnol, and T. Ozaki. Intense terahertz radiation and their applications, 2016.

[19] Mojca Jazbinsek, Uros Puc, Andreja Abina, and Aleksander Zidansek. Organic Crystals for THz Photonics. *Applied Sciences*, 9(5):882, 2019.

[20] W. D. Johnston and I. P. Kaminow. Contributions to optical nonlinearity in GaAs as determined from Raman scattering efficiencies. *Physical Review*, 1969.

[21] C. Vicario, A. V. Ovchinnikov, S. I. Ashitkov, M. B. Agranat, V. E. Fortov, and C. P. Hauri. Generation of 09-mJ THz pulses in DSTMS pumped by a Cr:Mg_2SiO_4 laser. *Optics Letters*, 2014.

[22] J. A. Fülöp, Z. Ollmann, Cs Lombosi, C. Skrobol, S. Klingebiel, L. P??lfalvi, F. Krausz, S. Karsch, and J. Hebling. Efficient generation of THz pulses with 0.4 mJ energy. *Optics express*, 22(17):20155–20163, 2014.

[23] Mostafa Shalaby and Christoph P. Hauri. Demonstration of a low-frequency three-dimensional terahertz bullet with extreme brightness. *Nature Communications*, 6:1–8, 2015.

[24] L. Pálfalvi, J. Hebling, G. Almási, Á Péter, K. Polgár, K. Lengyel, and R. Szipöcs. Nonlinear refraction and absorption of Mg doped stoichiometric and congruent LiNbO3. *Journal of Applied Physics*, 2004.

[25] Masaru Nakamura, Shinji Higuchi, Shunji Takekawa, Kazuya Terabe, Yasunori Furukawa, and Kenji Kitamura. Optical damage resistance and refractive indices in near-stoichiometric MgO-doped LiNbO3. *Japanese Journal of Applied Physics, Part 2: Letters*, 2002.

[26] X. C. Zhang, X. F. Ma, Y. Jin, T. M. Lu, E. P. Boden, P. D. Phelps, K. R. Stewart, and C. P. Yakymyshyn. Terahertz optical rectification from a nonlinear organic crystal. *Applied Physics Letters*, 1992.

[27] Jakub Imriska. *Generation and detection of terahertz pulses in the organic crystals OH1 and COANP*. PhD thesis, 2009.

[28] Q. Wu and X. C. Zhang. Free-space electro-optic sampling of terahertz beams. *Applied Physics Letters*, 1995.

[29] P. Uhd Jepsen, C. Winnewisser, M. Schall, and V. Schyja. Detection of THz pulses by phase retardation in lithium tantalate. *Physical Review E - Statistical Physics, Plasmas, Fluids, and Related Interdisciplinary Topics*, 1996.

[30] C. Winnewisser, P. Uhd Jepsen, M. Schall, V. Schyja, and H. Helm. Electro-optic detection of THz radiation in LiTaO3, LiNbO3 and ZnTe. *Applied Physics Letters*, 1997.

[31] J.Kerr. No Title. *Phil.Mag.*, 4(50):337, 1875.

[32] F. Booth. The dielectric constant of water and the saturation effect. *The Journal of Chemical Physics*, 19(4):391, 1951.

[33] Matthias C. Hoffmann, Nathaniel C. Brandt, Harold Y. Hwang, Ka Lo Yeh, and Keith a. Nelson. Terahertz Kerr effect. *Applied Physics Letters*, 95(23):100–103, 2009.

[34] Eric Freysz and Jérôme Degert. Nonlinear optics: Terahertz Kerr effect. *Nature Photonics*, 4(3):131–132, 2010.

[35] D J Tildesley and P A Madden. Time correlation functions for a model of liquid carbon disulphide. *Molec. Phys.*, 48(1):129, 1983.

[36] Peter Zalden, Liwei Song, Xiaojun Wu, Haoyu Huang, Frederike Ahr, Oliver D. Mücke, Joscha Reichert, Michael Thorwart, Pankaj Kr Mishra, Ralph Welsch, Robin Santra, Franz X. Kärtner, and Christian Bressler. Molecular polarizability anisotropy of liquid water revealed by terahertz-induced transient orientation. *Nature Communications*, 2018.

[37] Fivos Perakis, Luigi De Marco, Andrey Shalit, Fujie Tang, Zachary R. Kann, Thomas D. Kühne, Renate Torre, Mischa Bonn, and Yuki Nagata. Vibrational Spectroscopy and Dynamics of Water. *Chemical Reviews*, 116:7590, 2016.

[38] Pablo G Debenedetti. Supercooled and glassy water. *J. Phys.: Condens. Matter*, 15:R1669, 2003.

[39] J. K. Vij, D. R J Simpson, and O. E. Panarina. Far infrared spectroscopy of water at different temperatures: GHz to THz dielectric spectroscopy of water. *Journal of Molecular Liquids*, 112(3):125–135, 2004.

[40] N Q Vinh, Mark S Sherwin, S James Allen, D K George, A J Rahmani, Kevin W Plaxco, N Q Vinh, Mark S Sherwin, S James Allen, D K George, and A J Rahmani. High-precision gigahertz-to-terahertz spectroscopy of aqueous salt solutions as a probe of the femtosecond-to-picosecond dynamics of liquid water High-precision gigahertz-to-terahertz spectroscopy of aqueous salt solutions as a probe of the femtosecond-to. *The Journal of Chemical Physics*, 142:164502, 2015.

[41] Mohsen Sajadi, Martin Wolf, and Tobias Kampfrath. Transient birefringence of liquids induced by terahertz electric-field torque on permanent molecular dipoles. *Nature Communications*, 8:14963, 2017.

[42] John E. Bertie, R. Norman Jones, and C. Dale Keefe. Infrared intensities of liquids XII: Accurate optical constants and molar absorption coefficients between 6225 and 500 cm-1 of benzene at 25°C, from spectra recorded in several laboratories. *Applied Spectroscopy*, 50(6):147, 1995.

[43] Marie Claire Bellissent-Funel, Ali Hassanali, Martina Havenith, Richard Henchman, Peter Pohl, Fabio Sterpone, David Van Der Spoel, Yao Xu, and Angel E. Garcia. Water Determines the Structure and Dynamics of Proteins. *Chemical Reviews*, 116(13):7673–7697, 2016.

[44] I. Shvab and Richard J. Sadus. Intermolecular potentials and the accurate prediction of the thermodynamic properties of water. *Journal of Chemical Physics*, 2013.

[45] J. K. Gregory, D. C. Clary, K. Liu, M. G. Brown, and R. J. Saykally. The water dipole moment in water clusters. *Science*, 1997.

[46] Y. S. Badyal, M. L. Saboungi, D. L. Price, S. D. Shastri, D. R. Haeffner, and A. K. Soper. Electron distribution in water. *Journal of Chemical Physics*, 2000.

[47] T. R. Dyke, K. M. Mack, and S. J. Muenter. The structure of water dimer from molecular beam electric resonance spectroscopy. *The Journal of Chemical Physics*, 66(2):498, 1977.

[48] C J F Böttcher and P Bordewijk. *Theory of Electric Polarization, Vol II Dielectrics in Time-Dependent Fields*. Elsevier, 1996.

[49] R. K. Khanna, E. Dempsey, and G. Parry Jones. Kerr constant of water from 280 to 350 K at 632.8 nm. *Chemical Physics Letters*, 53(3):542, 1978.

[50] W H Orttung and J A Meyers. The Kerr Constant of Water. *Journal of Physical Chemistry*, 67(9):1905–1910, 1963.

[51] Z. Blaszczak and P. Gauden. Method for the determination of the value of the optical Kerr constant in weakly anisotropic liquids. *Review of Scientific Instruments*, 58(10):1949–1951, 1987.

[52] N. J. Harrison and B. R. Jennings. Laser-Induced Kerr Constants for Pure Liquids, 1992.

[53] A. Taschin, P. Bartolini, R. Eramo, R. Righini, and R. Torre. Optical Kerr effect of liquid and supercooled water: The experimental and data analysis perspective. *Journal of Chemical Physics*, 141(8):4507, 2014.

[54] Xiaojun Wu, Sergio Carbajo, Koustuban Ravi, Frederike Ahr, Giovanni Cirmi, Yue Zhou, Oliver D. Mücke, and Franz X. Kärtner. Terahertz generation in lithium niobate driven by Ti:sapphire laser pulses and its limitations. *Optics Letters*, 2014.

[55] D. Grischkowsky, Søren Keiding, Martin van Exter, and Ch. Fattinger. Far-infrared time-domain spectroscopy with terahertz beams of dielectrics and semiconductors. *Journal of the Optical Society of America B*, 1990.

[56] N. Board. The Complete Technology Book of Essential Oils. *Aromatic Chemicals*.

[57] Peter Zalden, Liwei Song, Xiaojun Wu, Haoyu Huang, Frederike Ahr, Oliver D. Mücke, Joscha Reichert, Michael Thorwart, Pankaj Kr Mishra, Ralph Welsch, Robin Santra, Franz X. Kärtner, and Christian Bressler. Molecular polarizability anisotropy of liquid water revealed by terahertz-induced transient orientation. *Nature Communications*, 9(1), 12 2018.

[58] William T Coffey and Yuri P Kalmykov. *The Langevin Equation*. World Scientific Series in Contemporary Chemical Physics, 2012.

[59] Sergey Bodrov, Yury Sergeev, Aleksey Murzanev, and Andrey Stepanov. Terahertz induced optical birefringence in polar and nonpolar liquids Terahertz induced optical birefringence in polar and nonpolar liquids. *The Journal of Chemical Physics*, 147:084507, 2017.

[60] S Kedenburg, M Vieweg, T Gissibl, and H Giessen. Linear refractive index and absorption measurements of nonlinear optical liquids in the visible and near-infrared spectral region. *Optical Materials Express*, 2(11):1588–1611, 2012.

[61] Konstantinos Moutzouris, Myrtia Papamichael, Sokratis C. Betsis, Ilias Stavrakas, George Hloupis, and Dimos Triantis. Refractive, dispersive and thermo-optic properties of twelve organic solvents in the visible and near-infrared. *Applied Physics B: Lasers and Optics*, 116(3):617–622, 2014.

[62] Kunlun Bai and Joseph Katz. On the refractive index of sodium iodide solutions for index matching in PIV. *Experiments in Fluids*, 55(4), 2014.

[63] M. Heyden, J. Sun, S. Funkner, G. Mathias, H. Forbert, M. Havenith, and D. Marx. Dissecting the THz spectrum of liquid water from first principles via correlations in time and space. *Proceedings of the National Academy of Sciences*, 107(27):12068–12073, 2010.

[64] I. H. Malitson. Interspecimen Comparison of the Refractive Index of Fused Silica. *Journal of the Optical Society of America*, 55(10):1205, 1965.

[65] D Milam. Review and assessment of measured values of the nonlinear refractive-index coefficient of fused silica. *Applied Optics*, 37(3):546–550, 1998.

[66] José E F Rubio, Jesús M. Arsuaga, Mercedes Taravillo, Valentín G. Baonza, and Mercedes Cáceres. Refractive index of benzene and methyl derivatives: Temperature and wavelength dependencies. *Experimental Thermal and Fluid Science*, 28(8):887–891, 2004.

[67] S. K. Garg, J E Bertie, H Klip, and C P Smyth. Dielectric Relaxation, Far-Infrared Absorption, and Intermolecular Forces in Nonpolar Liquids. *The Journal of Chemical Physics*, 49(6):2551, 1968.

[68] S. A. Myers and E. J. Robinson. Kerr effect in CS2, C6H6, and CCl4. *Journal of Chemical Physics*, 58(8):3526–3527, 1973.

[69] Enthalpy of Fusion. In *CRC Handbook of Chemistry and Physics*, pages 4–134.

[70] D. Eisenberg and W. Kauzmann. *The Structure and Properties of Water*. Oxford University Press, Oxford, 2006.

[71] T. H. Maiman. Stimulated optical radiation in Ruby. *Nature*, 1960.

[72] P. A. Franken, A. E. Hill, C. W. Peters, and G. Weinreich. Generation of optical harmonics. *Physical Review Letters*, 1961.

[73] Jeffrey L. Krause, Kenneth J. Schafer, and Kenneth C. Kulander. High-order harmonic generation from atoms and ions in the high intensity regime. *Physical Review Letters*, 1992.

[74] P. B. Corkum. Plasma perspective on strong field multiphoton ionization. *Physical Review Letters*, 1993.

[75] K. J. Schafer, Baorui Yang, L. F. Dimauro, and K. C. Kulander. Above threshold ionization beyond the high harmonic cutoff. *Physical Review Letters*, 1993.

[76] H. R. Reiss. Complete Keldysh theory and its limiting cases. *Physical Review A*, 1990.

[77] Shambhu Ghimire, Anthony D. Dichiara, Emily Sistrunk, Pierre Agostini, Louis F. Dimauro, and David A. Reis. Observation of high-order harmonic generation in a bulk crystal. *Nature Physics*, 7(2):138, 12 2010.

[78] Shambhu Ghimire and David A. Reis. High-harmonic generation from solids. *Nature Physics*, 15(1):10–16, 2018.

[79] O. Schubert, M. Hohenleutner, F. Langer, B. Urbanek, C. Lange, U. Huttner, D. Golde, T. Meier, M. Kira, S. W. Koch, and R. Huber. Sub-cycle control of terahertz high-harmonic generation by dynamical Bloch oscillations. *Nature Photonics*, 8(2), 2014.

[80] T. T. Luu, M. Garg, S. Yu. Kruchinin, A. Moulet, M. Th Hassan, and E. Goulielmakis. Extreme ultraviolet high-harmonic spectroscopy of solids. *Nature*, 521(7553):498–502, 2015.

[81] Georges Ndabashimiye, Shambhu Ghimire, Mengxi Wu, Dana A. Browne, Kenneth J. Schafer, Mette B. Gaarde, and David A. Reis. Solid-state harmonics beyond the atomic limit. *Nature*, 534(7608):520–523, 2016.

[82] Naotaka Yoshikawa, Tomohiro Tamaya, and Koichiro Tanaka. High-harmonic generation in graphene enhanced by elliptically polarized light excitation. *Science*, 356(6339):736–738, 2017.

[83] Hanzhe Liu, Yilei Li, Yong Sing You, Shambhu Ghimire, Tony F. Heinz, and David A. Reis. High-harmonic generation from an atomically thin semiconductor. *Nature Physics*, 13(3):262–265, 2017.

[84] G. Vampa, T. J. Hammond, N. Thiré, B. E. Schmidt, F. Légaré, C. R. McDonald, T. Brabec, and P. B. Corkum. Linking high harmonics from gases and solids. *Nature*, 522(7557):462–464, 2015.

[85] Nicolas Tancogne-Dejean, Oliver D. Mücke, Franz X. Kärtner, and Angel Rubio. Ellipticity dependence of high-harmonic generation in solids originating from coupled intraband and interband dynamics. *Nature Communications*, 8(1):1–9, 2017.

[86] Oliver D. Mücke. Isolated high-order harmonics pulse from two-color-driven Bloch oscillations in bulk semiconductors. *Physical Review B*, 84(8):081202, 8 2011.

[87] M. Hohenleutner, F. Langer, O. Schubert, M. Knorr, U. Huttner, S. W. Koch, M. Kira, and R. Huber. Real-time observation of interfering crystal electrons in high-harmonic generation. *Nature*, 2015.

[88] Shambhu Ghimire, Anthony D. Dichiara, Emily Sistrunk, Georges Ndabashimiye, Urszula B. Szafruga, Anis Mohammad, Pierre Agostini, Louis F. Dimauro, and David A. Reis. Generation and propagation of high-order harmonics in crystals. *Physical Review A - Atomic, Molecular, and Optical Physics*, 85(4):1–6, 2012.

[89] D. Golde, T. Meier, and S. W. Koch. High harmonics generated in semiconductor nanostructures by the coupled dynamics of optical inter- and intraband excitations. *Physical Review B - Condensed Matter and Materials Physics*, 2008.

[90] Peter G. Hawkins, Misha Yu Ivanov, and Vladislav S. Yakovlev. Effect of multiple conduction bands on high-harmonic emission from dielectrics. *Physical Review A - Atomic, Molecular, and Optical Physics*, 2015.

[91] Takuya Higuchi, Christian Heide, Konrad Ullmann, Heiko B. Weber, and Peter Hommelhoff. Light-field-driven currents in graphene. *Nature*, 550(7675):224–228, 2017.

[92] G. Vampa, C. R. McDonald, G. Orlando, P. B. Corkum, and T. Brabec. Semiclassical analysis of high harmonic generation in bulk crystals. *Physical Review B - Condensed Matter and Materials Physics*, 2015.

[93] G. Vampa, C. R. McDonald, G. Orlando, D. D. Klug, P. B. Corkum, and T. Brabec. Theoretical analysis of high-harmonic generation in solids. *Physical Review Letters*, 2014.

[94] Mengxi Wu, Shambhu Ghimire, David A. Reis, Kenneth J. Schafer, and Mette B. Gaarde. High-harmonic generation from Bloch electrons in solids. *Physical Review A - Atomic, Molecular, and Optical Physics*, 2015.

[95] A. F. Kemper, B. Moritz, J. K. Freericks, and T. P. Devereaux. Theoretical description of high-order harmonic generation in solids. *New Journal of Physics*, 2013.

[96] Wei Liu. Advanced ultrafast fiber laser sources enabled by fiber nonlinearities. (September), 2016.

[97] G. Vampa, T. J. Hammond, M. Taucer, Xiaoyan Ding, X. Ropagnol, T. Ozaki, S. Delprat, M. Chaker, N. Thiré, B. E. Schmidt, F. Légaré, D. D. Klug, A. Yu Naumov, D. M. Villeneuve, A. Staudte, P. B. Corkum, M. Taucer, A. Yu Naumov, B. E. Schmidt, T. J. Hammond, Xiaoyan Ding, T. Ozaki, F. Légaré, D. D. Klug, D. M. Villeneuve, M. Chaker, N. Thiré, G. Vampa, X. Ropagnol, A. Staudte, and P. B. Corkum. Strong-field optoelectronics in solids. *Nature Photonics*, 12(8):465–468, 2018.

[98] Yong Sing You, Mengxi Wu, Yanchun Yin, Andrew Chew, Xiaoming Ren, Shima Gholam-Mirzaei, Dana A. Browne, Michael Chini, Zenghu Chang, Kenneth J. Schafer, Mette B. Gaarde, and Shambhu Ghimire. Laser waveform control of extreme ultraviolet high harmonics from solids. *Optics Letters*, 2017.

[99] Yong Sing You, David A. Reis, and Shambhu Ghimire. Anisotropic high-harmonic generation in bulk crystals. *Nature Physics*, 13(4):345–349, 2017.

[100] Hyunwoong Kim, Seunghwoi Han, Yong Woo Kim, Seungchul Kim, and Seung Woo Kim. Generation of Coherent Extreme-Ultraviolet Radiation from Bulk Sapphire Crystal. *ACS Photonics*, 2017.

[101] Martin Wegener. *Extreme nonlinear optics : an introduction*. 2005.

[102] N. W. Ashcroft and N. D. Mermin. Solid State Physics, 1976.

[103] Nicolas Tancogne-Dejean, Oliver D. Mücke, Franz X. Kärtner, and Angel Rubio. Impact of the Electronic Band Structure in High-Harmonic Generation Spectra of Solids. *Physical Review Letters*, 118(8):1–6, 2017.

[104] N Klemke, N. Tancogne-Dejean, G. M. Rossi, Y. Yang, F. Scheiba, R. E. Mainz, G. Di Sciacca, A. Rubio, F. X. Kärtner, and O. D. Mücke. Polarization-state-resolved high-harmonic spectroscopy of solids. *Nature Communications*, 10(1):2–3, 2019.

[105] D. N. Basov, R. D. Averitt, and D. Hsieh. Towards properties on demand in quantum materials, 2017.

[106] Rune S. Jacobsen, Karin N. Andersen, Peter I. Borel, Jacob Fage-Pedersen, Lars H. Frandsen, Ole Hansen, Martin Kristensen, Andrei V. Lavrinenko, Gaid Moulin, Haiyan Ou, Christophe Peucheret, Beáta Zsigri, and Anders Bjarklev. Strained silicon as a new electro-optic material. *Nature*, 441(7090):199–202, 2006.

[107] E. Timurdogan, C. V. Poulton, M. J. Byrd, and M. R. Watts. Electric field-induced second-order nonlinear optical effects in silicon waveguides. *Nature Photonics*, 11(3):200–206, 2017.

[108] Kirill A. Grishunin, Nikita A. Ilyin, Natalia E. Sherstyuk, Elena D. Mishina, Alexey Kimel, Vladimir M. Mukhortov, Andrey V. Ovchinnikov, Oleg V. Chefonov, and Mikhail B. Agranat. THz Electric Field-Induced Second Harmonic Generation in Inorganic Ferroelectric. *Scientific Reports*, 7(1):1–8, 2017.

[109] M. Cazzanelli, F. Bianco, E. Borga, G. Pucker, M. Ghulinyan, E. Degoli, E. Luppi, V. Véniard, S. Ossicini, D. Modotto, S. Wabnitz, R. Pierobon, and L. Pavesi. Second-harmonic generation in silicon waveguides strained by silicon nitride. *Nature Materials*, 11(2):148–154, 2012.

[110] H Huang, L Song, N Klemke, A Rubio, and F X Kärtner. High-Order Harmonic Generation from Solids Dressed by an Intense Terahertz Field. 2:6–7, 2018.

[111] Lucie Prussel. Ab-initio description of optical nonlinear properties of semiconductors in the presence of an electrostatic field. 2017.

[112] C. Attaccalite and M. Grüning. Nonlinear optics from an ab initio approach by means of the dynamical Berry phase: Application to second- and third-harmonic generation in semiconductors. *Physical Review B - Condensed Matter and Materials Physics*, 2013.

[113] Erich Runge and E. K.U. Gross. Density-functional theory for time-dependent systems. *Physical Review Letters*, 1984.

[114] Robert Van Leeuwen. Causality and symmetry in time-dependent density-functional theory. *Physical Review Letters*, 1998.

[115] Xavier Andrade, David Strubbe, Umberto De Giovannini, Ask Hjorth Larsen, Micael J.T. Oliveira, Joseba Alberdi-Rodriguez, Alejandro Varas, Iris Theophilou, Nicole Helbig, Matthieu J. Verstraete, Lorenzo Stella, Fernando Nogueira, Alán Aspuru-Guzik, Alberto Castro, Miguel A.L. Marques, and Angel Rubio. Real-space grids and the Octopus code as tools for the development of new simulation approaches for electronic systems. *Physical Chemistry Chemical Physics*, 2015.

[116] Nicolas Tancogne-Dejean, Michael A. Sentef, and Angel Rubio. Ultrafast Modification of Hubbard U in a Strongly Correlated Material: Ab initio High-Harmonic Generation in NiO. *Physical Review Letters*, 2018.

[117] Nicolas Tancogne-Dejean, Oliver D. Mücke, Franz X. Kärtner, and Angel Rubio. Ellipticity dependence of high-harmonic generation in solids: unraveling the interplay between intraband and interband dynamics. *Nature Communications*, 2017.

[118] D. A. Varshalovich, A. N. Moskalev, and V. K. Khersonskii. *Quantum Theory of Angular Momentum*. World Scientific, 1988.

[119] William A. Wegener. Transient electric birefringence of dilute rigid-body suspensions at low field strengths. *The Journal of Chemical Physics*, 84(11):5989, 1986.

Appendix A

Theory of Coffey and Kalmykov

A.1 Theory of Coffey and Kalmykov

A theoretical description for dynamic Kerr signals of polar, asymmetric-top molecules in a solvent has been given by Coffey and Kalmykov [58] In their approach, the emergence of birefringence in response to strong electric fields is treated on the basis of rotational Brownian motion of single molecules. Specifically, a perturbing electric field seeks to rotate molecules on basis of their permanent dipole moments and (hyper-) polarizabilities, while thermal fluctuations aim to lead the system back towards an equilibrium distribution. This interplay is captured by an Euler-Langevin equation in the overdamped (Debye) and dilute (non-interacting) limit which is used to derive a hierarchy of differential recurrence relations for the appropriate statistical moments of the problem. In this case, these are given by averages of Wigner's D functions $D^{j}_{m,n}(t)$ [118] which form an orthonormal basis set for the construction of the relevant quantities. For comparably low electric field strengths the hierarchy can be truncated early, leading to a simple description via two coupled vector-differential equations

$$\frac{d}{dt}\mathbf{c_1}(t) = \hat{A}_1\mathbf{c_1}(t) + E(t)\mathbf{B_1} \tag{A.1}$$

$$\frac{d}{dt}\mathbf{c_2}(t) = E(t)\hat{Q}\mathbf{c_1}(t) + \hat{A}_2\mathbf{c_2}(t) + E^2(t)\mathbf{B_2} \tag{A.2}$$

Here, the vectors $c_1(t)$ and $c_2(t)$ carry averages of the first and second Wigner functions

$$\mathbf{c_1}(t) = \begin{pmatrix} \left\langle D^1_{0,-1} \right\rangle (t) \\ \left\langle D^1_{0,0} \right\rangle (t) \\ \left\langle D^1_{0,1} \right\rangle (t) \end{pmatrix}, \mathbf{c_2}(t) = \begin{pmatrix} \left\langle D^2_{0,-2} \right\rangle (t) \\ \left\langle D^2_{0,-1} \right\rangle (t) \\ \left\langle D^2_{0,0} \right\rangle (t) \\ \left\langle D^2_{0,1} \right\rangle (t) \\ \left\langle D^2_{0,2} \right\rangle (t) \end{pmatrix} \tag{A.3}$$

Their time-evolution is determined by the coefficients of the rotational diffusion tensor D_{ij} and the response to the perturbing electric field $E(t)$. The latter is given by the permanent dipole moment μ and the elements of the electric polarizability tensor ε_{ij} of a molecule. Hyperpolarizabilities are neglected here. In our case, the molecular reference frame xyz is chosen in such a way that the rotational diffusion tensor is diagonal and encoded within

$$\Delta = \frac{D_{zz}}{D_{xx} + D_{yy}} - \frac{1}{2} \tag{A.4}$$

$$\tau_D = \frac{1}{D_{xx} + D_{yy}} \tag{A.5}$$

$$\Xi = \frac{D_{xx} - D_{yy}}{D_{xx} + D_{yy}} \tag{A.6}$$

The matrices $\hat{A}_1$ and $\hat{A}_2$ are then related to relaxation back towards the equilibrium distribution and read

$$\hat{A}_1 = -\tau_D^{-1} \begin{pmatrix} 1+\Delta & 0 & \Xi/2 \\ 0 & 1 & 0 \\ \Xi/2 & 0 & 1+\Delta \end{pmatrix} \tag{A.7}$$

$$\hat{A}_2 = -\tau_D^{-1} \begin{pmatrix} 3+4\Delta & 0 & \Xi\sqrt{3/2} & 0 & 0 \\ 0 & 3+\Delta & 0 & 3\Xi/2 & 0 \\ \Xi\sqrt{3/2} & 0 & 3 & 0 & \Xi\sqrt{3/2} \\ 0 & 3\Xi/2 & 0 & 3+\Delta & 0 \\ 0 & 0 & \Xi\sqrt{3/2} & 0 & 3+4\Delta \end{pmatrix} \tag{A.8}$$

where the diagonal entries give rise to relaxation times of the order of τ_D and $\tau_D/3$ respectively if Ξ and Δ can be neglected. The vector $B_1(t)$ and the matrix $\hat{Q}$ relate to the impact of the

permanent dipole moment

$$\hat{Q} = \frac{\sqrt{3}}{10\tau_D k_B T} \begin{pmatrix} \mu^-(3+4\Delta) - \mu^+\Xi & \sqrt{2}\mu_z\Xi & 0 \\ 3\mu_z & [\mu^-(3+2\Delta) - 2\mu^+\Xi]/\sqrt{2} & \mu_z\Xi \\ \sqrt{3/2}(\mu^-\Xi - \mu^+) & 2\sqrt{3}\mu_z & \sqrt{3/2}(\mu^- - \mu^+\Xi) \\ \mu_z\Xi & [2\mu^-\Xi - \mu^+(3+2\Delta)]/\sqrt{2} & 3\mu_z \\ 0 & \sqrt{2}\mu_z\Xi & \mu^-\Xi - \mu^+(3+4\Delta) \end{pmatrix} \tag{A.9}$$

$$\mathbf{B_1} = \frac{1}{3\sqrt{2}\tau_D k_B T} \begin{pmatrix} \mu^-(1+\Delta) - \mu^+\Xi/2 \\ \sqrt{2}\mu_z \\ -\mu^+(1+\Delta) + \mu^-\Xi/2 \end{pmatrix} \tag{A.10}$$

where $\mu^{\pm} = \mu_x \pm i\mu_y$. Finally, the vector $B_2(t)$ gives the coupling to the electric polarizability

$$\mathbf{B_2} = \frac{1}{10\sqrt{6}\tau_D k_B T} \begin{pmatrix} (\varepsilon_{xx} - 2i\varepsilon_{xy} - \varepsilon_{yy})(3+4\Delta) - (\varepsilon_{xx} + \varepsilon_{yy} - 2\varepsilon_{zz})\Xi \\ 2(\varepsilon_{xz} - i\varepsilon_{yz})(3+\Delta) - 3(\varepsilon_{xz} + i\varepsilon_{yz})\Xi \\ \sqrt{6}[2\varepsilon_{zz} - \varepsilon_{xx} - \varepsilon_{yy} + \Xi(\varepsilon_{xx} - \varepsilon_{yy})] \\ -2(\varepsilon_{xz} + i\varepsilon_{yz})(3+\Delta) + 3(\varepsilon_{xz} - i\varepsilon_{yz})\Xi \\ (\varepsilon_{xx} + 2i\varepsilon_{xy} - \varepsilon_{yy})(3+4\Delta) - (\varepsilon_{xx} + \varepsilon_{yy} - 2\varepsilon_{zz})\Xi \end{pmatrix} \tag{A.11}$$

In a Kerr measurement, the perturbing electric field is assumed to occur along the axis Z in the laboratory coordinate system spanned by the three axes XYZ. The birefringence is then measured between the axes X and Z with an optical probing pulse. It can be derived from the measured optical anisotropy $\Delta\alpha(t) = \langle \alpha_{ZZ} - \alpha_{XX} \rangle(t)$ by way of the Lorenz-Lorentz equation as

$$\Delta n(t) \approx \frac{2\pi\rho_0}{n_s} \Delta\alpha(t) \tag{A.12}$$

with the number density ρ_0, the refractive index of the solvent n_s and formulated here for a polarizability volume $\alpha = \alpha'/4\pi\varepsilon_0$ [119, 48]. The connection between $\Delta\alpha(t)$ and equation (A.1) and equation (A.2) is given by a dot product

$$\Delta\alpha(t) = a_2 \cdot \mathbf{c_2}(\mathbf{t}) \tag{A.13}$$

where a_2 contains the spherical components of the body-fixed optical polarizability tensor $\widehat{\alpha}_0$ and reads

$$a_{\mathbf{2}} = \sqrt{3/8}\begin{pmatrix} \alpha_{xx} - \alpha_{yy} + 2i\alpha_{xy} \\ 2\left(\alpha_{xz} + i\alpha_{yz}\right) \\ \sqrt{6}\left[\alpha_{zz} - \mathrm{Tr}[\hat{\alpha}]/3\right] \\ 2\left(-\alpha_{xz} + i\alpha_{yz}\right) \\ \alpha_{xx} - \alpha_{yy} - 2i\alpha_{xy} \end{pmatrix} \tag{A.14}$$

The vector $a_{\mathbf{2}}$ contains anisotropies of the optical polarizability and defines the dimension and overall size of the resulting signal. In fact, its central component can be rewritten as $\Delta\alpha_0 = \alpha_{0,\|} - \alpha_{0,\perp} = \alpha_{zz} - (1/2)(\alpha_{xx} + \alpha_{yy})$ and multiplies to the central components of both c_1 and c_2. If we choose the molecular z-axis to coincide with the permanent dipole moment, these elements give direct measures for orientation and alignment of the molecules as

$$\left\langle D^1_{0,0}\right\rangle(t) = \langle\cos(\theta)\rangle(t) \tag{A.15}$$

$$\left\langle D^2_{0,0}\right\rangle(t) = \frac{1}{2}\left(\left\langle 3\cos^2(\theta) - 1\right\rangle(t)\right) \tag{A.16}$$

Both relations follow from a general property of the D functions, specifically $D^j_{0,0} = P_j(\cos(\theta))$, where P_j is the Legendre polynomial of rank j and θ the Euler angle between the molecular z-axis and the laboratory Z-axis [58, 118]. For the case of isotropic rotational diffusion, where $D_{xx} = D_{yy} = D_{zz} = D$ such that $\Xi = \Delta = 0$, we can formally solve the theory of equation (A.1) and equation (A.2). Assuming isotropic initial conditions where $\mathbf{c}_1(0) = 0$ and $\mathbf{c}_2(0) = 0$ as well as choosing the molecular z-axis to coincide with the permanent dipole moment, we obtain

$$\begin{aligned}\Delta\alpha(t) = \frac{1}{5\tau_D}\Big[\frac{3}{4}\frac{\Delta\alpha_0^+\Delta\varepsilon_0^+}{k_BT} + \frac{\Delta\alpha_0\Delta\varepsilon_0}{k_BT}\Big]\iint_0^t duE^2(u)e^{-3\frac{(t-u)}{\tau_D}} \\ + \frac{1}{5\tau_D^2}\frac{\Delta\alpha_0\mu_z^2}{(k_BT)^2}\int_0^t du\int_0^u ds\left[E(u)e^{-3\frac{(t-u)}{\tau_D}}\right]\left[E(s)e^{-\frac{(u-s)}{\tau_D}}\right]\end{aligned} \tag{A.17}$$

where we defined $\Delta\alpha_0^+ = \alpha_{xx} - \alpha_{yy}$ and $\Delta\varepsilon_0^+ = \varepsilon_{xx} - \varepsilon_{yy}$ as well as $\Delta\varepsilon_0 = \varepsilon_{zz} - (1/2)(\varepsilon_{xx} + \varepsilon_{yy})$ in accordance with $\Delta\alpha_0$. Equation (A.17) renders two distinct behaviors: the first term induces a symmetric signal which depends on the anisotropies of the electric polarizability and the second creates a non-symmetric term that depends on the permanent dipole moment. For molecules with zero permanent dipole moment, we expect a symmetric contribution consistent with the results for Benzene and CS_2 in the main text. For molecules with non-zero permanent dipole moment, the second term contributes as well and we expect an interplay between both

contributions. The latter may be a particularly important component for the measurement on water and the alcohols.

This section was contributed by our collaborators Joscha Reichert and Michael Thorwart and published in Ref. [57].